Winter Is Coming

The Global Cooling and the Next Little Ice Age

Frank Dosk

Contents

Winter Is Coming 5

1 Introduction: The Case for an Incoming Little Ice Age 7
1.1 A Climate That Has Always Changed 7
1.2 Why Now Weakening Cycles 24 and 25 8
1.3 Ocean Modes Turning Cold AMO and PDO 9
1.4 Echoes of the Pre Maunder Configuration 10
1.5 Why This Book and How It Argues 11

2 History of Past Cold and Warm Periods 13
2.1 Cosmogenic Isotopes as a Solar Proxy 13
2.2 Pre Maunder Grand Minima 14
2.3 The Maunder and Dalton Minima Up Close 15
2.4 Grand Maxima and Societal Abundance 16
2.5 The Long Cycles Hallstatt Eddy Bray 17

3 Solar Science Foundations 21
3.1 From Galileo to the Photoheliograph 21
3.2 Cycle Metrics Schwabe Hale Butterfly 22
3.3 Sunspot Numbers and Their Recalibration 24
3.4 The Satellite Era TSI Record 25
3.5 F10.7 and the Modern Activity Index 27

4 The Grand Solar Cycles: Zharkova's Two-Wave Dynamo 29
4.1 The Solar Background Magnetic Field 29
4.2 PCA and the Two Wave Decomposition 32
4.3 Isotope Validation 35
4.4 The 2020 2053 Modern Grand Solar Minimum Prediction 36
4.5 Flare Physics the Same Magnetic Field 39

5 The Sun's Inertial Motion 43
5.1 How Exoplanets Reveal Stellar Wobble 43
5.2 Solar Inertial Motion SIM 45
5.3 The Jose Cycle and Longer Beats 49
5.4 Harmonic Analysis Yndestad and Abdussamatov 52
5.5 How Planetary Forcing Reaches Earth S Climate 53

6 The Cloud Hypothesis: Cosmic Rays and Climate 55
6.1 How Cosmic Rays Reach the Lower Atmosphere 55

6.2 Forbush Decreases the Natural Experiment . . . 56
6.3 Chamber Evidence Sky and Cloud . . . 58
6.4 Heliospheric Modulation and Global Temperature . . . 59
6.5 Shaviv and the Spiral Arm Record . . . 60

7 The Underground Connection: Volcanism and the Sun . . . 63
7.1 When the Sun Goes Quiet the Earth Gets Loud . . . 63
7.2 The Maunder Era Eruptions . . . 66
7.3 Tambora and the Year Without a Summer . . . 68
7.4 Hunga Tonga the Eruption That Warmed the World . . . 72
7.5 Mechanisms Why Might the Sun Affect the Earth S Crust . . . 73
7.6 What If the Next Minimum Brings the Next Big Eruption . . . 75

8 There Is No Such Thing as Settled Science . . . 79
8.1 Warming Happened but Who Did It . . . 79
8.2 The Natural CO_2 Budget . . . 80
8.3 The Surface Temperature Record Under a Magnifying Glass . . . 82
8.4 TSI vs CO_2 the Connolly Soon Attribution . . . 84
8.5 Natural Cycles as Confounders Scafetta AMO PDO . . . 86

9 What Can We Do? Preparation for the Next Minimum . . . 89
9.1 The Historical Baseline What Cold Periods Look Like . . . 89
9.2 Grid and Energy Resilience . . . 90
9.3 Food Security and Agriculture . . . 91
9.4 Water Sanitation and the Built Environment . . . 93
9.5 Household and Regional Preparedness . . . 93
9.6 The Precautionary Closing Argument . . . 94

References . . . 97

Appendices . . . 107

A Downloads . . . 109

B About . . . 111
B.1 The author . . . 111
B.2 Corrections . . . 111
B.3 License . . . 111
B.4 Cite this book . . . 111

C Changelog . . . 113
C.1 Version 293 — 2026-07-08 15:39 UTC . . . 113

Winter Is Coming

The book describes why the planet is cooling, why we are entering the next Little Ice Age, and how the Sun is actually responsible for Earth's climate.

> **Draft — work in progress.** You are reading version 293 of a living document, generated 2026-07-08 15:39 UTC. Chapters, figures, and citations may change between releases. The latest edition — readable online or as a fresh download — always lives at https://winter-is-coming.pages.dev.

This book is organised into 9 chapters. Every claim is followed by a bracketed marker such as [1] that links to the full source in the References.

1. Introduction: The Case for an Incoming Little Ice Age

The climate is cooling, weakening solar cycles 24–25 echo the pre-Maunder pattern, and a public-facing precautionary case is overdue.

1.1 A Climate That Has Always Changed

To understand the current trajectory, we must first recognize that change is the norm, not the exception, across the Holocene epoch. [1] The Greenland Ice Sheet Project 2 (GISP2) provides a critical window into this past, having taken five years and over 3 km of drilling to reach bedrock in 1993. [1] Analysis of Dansgaard–Oeschger (D–O) events in the GISP2 ice core led to the discovery that they displayed a prominent frequency at 1470 years, a periodicity that Stefan Rahmstorf argued had less than 1% probability of being due to chance. [1] While the result was not so clear in similar ice cores like the European GRIP (Greenland Ice Core Project) completed in 1992, GISP2 was considered to have better resolution. [1] The GISP2 record of $\delta^{18}O$ serves as a proxy for Greenland temperature and has been placed on the new GICC05 timescale. [1] Dividing the 48–10 kyr BP period in boxes of approximately 1500 years helps display the periodicity of the D–O cycle, with the abrupt start of the Holocene in the North Atlantic considered the most recent D–O warming. [1] A new reconstruction of temperature variability in the extratropical Northern Hemisphere during the last two millennia, utilizing many palaeotemperature proxy records never previously included in any large-scale temperature reconstruction, shows a distinct Roman Warm Period c. [2] AD 800–1300. This reconstruction demonstrates that decadal mean temperatures seem to have reached or exceeded the 1961–1990 mean temperature level during substantial parts of these earlier warm periods. [2] During the Medieval Climate Anomaly, spanning the 10th to 13th centuries CE, temperature and hydrological shifts were not uniform. [3] Peatland water-table reconstructions from the North Atlantic Region show that the onset of drier conditions varied temporally and spatially, with some sites recording contradictory hydrological conditions despite their proximity. [4] This high degree of spatial variability suggests that the Medieval Climate Anomaly was characterized by strong regional differences rather than uniform global warmth. Furthermore, global temperature composites indicate that peak Northern Hemisphere warmth during the Middle Ages was less than or at most comparable to the mid-20th-century warm period, as Medieval temperature peaks were not synchronous in all records. [5][6][4][1] The inherent ambiguities in defining this feature underscore the complexity of paleoclimate data. [1] Specifically, the Neoglacial cooling trend averaged approximately −0.2 °C per millennium, a rate that demonstrates the profound impact of even modest temperature changes on global systems. This gradual cooling, which culminated in the Little Ice Age, caused considerable glacier expansion and biome changes, such as the reduction of tropical forests and the expansion of tundra. [1] While short-term fluctuations of 0.4 °C can occur over just a few years, they are transient compared to these millennial-scale trends. [1] Understanding this deep historical context is crucial, as it challenges the assumption that recent warming is entirely anomalous. [1]

The prevailing narrative often frames climate change as a singular, unprecedented crisis driven solely by modern industrial activity, yet this view overlooks the deep historical context of Earth's natural variability. [1] As Freeman Dyson noted, climate change is part of the normal order of things, a process that was already occurring before humans came. This intrinsic variability demonstrates that the climate system has always changed, establishing a baseline of natural fluctuation that predates the current era of concern. [1] Recognizing that climate change has always happened allows us to properly understand the totality of climate change, moving beyond a narrow focus on emissions to consider the profound effect of natural climate cycles and events that have shaped the planet's past. [1] This broader perspective is essential for addressing the unanswered questions in natural climate change that are usually restricted to highly specialized scientific works. [1] While the Intergovernmental Panel on Climate Change (IPCC) presents a specific view of the past 10,000 years, some researchers argue that this depiction of temperature history is selective and incorrect. This contention arises from discrepancies between official records and independent data analyses. [7][1] For instance, critiques suggest that the IPCC's temperature history is contradicted by the actual data record, pointing to figures that reveal a more nuanced picture than

the "approved" storybook narrative implies. [7] The reliance on smoothed global proxy reconstructions, which depend heavily on researcher choices and limited low-precision proxies, introduces significant uncertainty. [1] Consequently, alternative reconstructions, such as those correcting for proxy re-dating and smoothing issues, present a different trajectory. This evidence supports the view that the standard IPCC depiction may be flawed, suggesting that our understanding of past climate stability requires revision. [8] While the Mauna Loa series is frequently cited as the gold standard for pristine measurements, significant disputes exist concerning the accuracy of broader atmospheric CO2 records and the true significance of human emissions over the past 150 years. Critics argue that the objections raised against ice-core data are mysteriously not applied to surface temperature measurements, creating an asymmetry in scientific scrutiny. [9][7][10][1]

1.2 Why Now Weakening Cycles 24 and 25

Solar cycle 24 exhibited lower intensity than cycle 23, and forecasters across the solar-minimum literature projected that cycle 25 would be weaker still. This decline is not merely a fluctuation in sunspot counts but reflects a substantial weakening of the Sun's magnetic field, as evidenced by a 51% reduction in integrated solar magnetic energy density from cycle 23 to cycle 24. [11][12][13] Furthermore, the solar wind Alfven speeds dropped below 57 km/s, a marked decrease from the range observed in cycles 22 and 23, while the solar wind magnetosonic Mach number showed a larger lower bound for cycle 24 compared to its predecessors. These changes have weakened the energy coupling parameter, leading to a substantial 15%–38% decrease in the average strength of high-latitude ionospheric, low-latitude magnetospheric, and equatorial ionospheric current systems. [12] Consequently, high-latitude Joule heating manifested a reduction of approximately 30% during cycle 24. This alignment supports the prediction of a modern grand solar minimum spanning from 2020 to 2053. [14] As we move deeper into this predicted quiet period, the data suggests that the Sun is entering a phase of diminished output that could have important implications for our Earth's atmosphere-ionosphere-magnetosphere system. [15]

The Sun's energy output is not static; it fluctuates with the solar cycle, and recent data reveals a troubling trend. [16] Total Solar Irradiance (TSI), the measure of solar energy reaching Earth, has shown an increasing rate of decline from cycle 22 through cycle 24, continuing into cycle 25. This acceleration is stark: the average annual decrease rate in the 22nd cycle was approximately 0.007 Wm^{-2}/yr, rising to ~0.02 Wm^{-2}/yr in the 23rd cycle. [16][12] In the current cycle, this rate has jumped to almost 0.1 Wm^{-2}/yr, a trajectory that is consistent with a deepening solar dimming. [16] The 11-year component of TSI in the current cycle has decreased by almost 0.7 Wm^{-2} with respect to cycle 23, while the average cyclical values were lower by ~0.15 Wm^{-2} in the 23rd cycle than in the 22nd. [16] Furthermore, the TSI value at the minimum between cycles 23 and 24 was lower by ~0.23 Wm^{-2} compared to the 22/23 minimum. This observed trend of increasing TSI decline suggests that the current solar behavior mirrors the analogous TSI decline of the Maunder Minimum period, setting the stage for a new era of reduced solar heating. [16] This level was $0.32\,W/m^2$ lower than the minimum of the 21st cycle in October 1986 and $0.25\,W/m^2$ lower than the 22nd cycle minimum in June 1996. [17] The value of TSI at the minimum between 23/24 cycles ($1365.27 \pm 0.02\,Wm^{-2}$) was lower by ~0.23 and ~0.30 Wm^{-2} than at the minima between 22/23 and 21/22 cycles, respectively. [16] This confirms that the TSI minimum between cycles 23 and 24 was lower than the minima between cycles 21/22 and 22/23. This finding suggests that the solar irradiance during this specific minimum was indeed anomalously low compared to recent historical precedents. [18][16][17][19][20] This decline is consistent with analyses of the solar background magnetic field derived from WSO magnetic synoptic maps, which indicated that cycle 25 would exhibit smaller activity compared to cycle 24. [11] Such findings align with the prediction of a modern grand solar minimum spanning 2020 to 2053. [14] Furthermore, predictions based on the Layman's Sunspot Count, which utilizes SIDC values while ignoring specks rated lower than 23 pixels, indicated that cycles 24 and 25 would remain below 50 SSN. This approach quantifies AMP events to provide a platform for future sunspot prediction out to 3000 AD. [21] The current AMP group, which began with solar cycle 20, failed to generate a full grand minimum due to a weak AMP event caused by the late timing of the Uranus/Neptune conjunction and a failed Wilson's Test. [21] The results indicate that a solar minimum is in progress during cycle 24, with Cycle 24 being smaller than Cycle 23 and — in that projection — Cycle 25 smaller than Cycle 24. [22] This pattern suggests continued weakness through cycle 27, around 2050, consistent with a Dalton-type solar minimum. The expected intensity of this prolonged low-activity period is similar to that of the Dalton Minimum, reinforcing the view that the current solar behavior marks a significant departure from the stronger cycles of the mid-twentieth century. [22][23] By classifying solar Cycle 24 as moderate or low based on the negative power anomaly and the negative phase of the 120-year solar magnetic pattern, these models supported the conclusion that Cycle 25 could not be high. [23] Analysis of the Clouds and the

Earth's Radiant Energy System, Energy Balanced And Filled data (CERES EBAF 2.8) reveals a small but negative trend in the net Top Of Atmosphere (TOA) energy imbalance over the past decade, a finding that contradicts earlier assertions that external radiative forcing was not essential to the climate hiatus. [24] This negative trend in the net radiation is consistent with the decreasing Total Solar Irradiance (TSI), as the incoming solar radiation has decreased due to the approach toward the Centennial Gleissberg Cycle (CGC) minimum, while the Outgoing Longwave Radiation (OLR) has remained largely unchanged owing to the lack of a global temperature trend during the hiatus, and the Reflected Shortwave (RSW) radiation, determined by albedo, did not significantly change. [24] Consequently, over a span of approximately 53 to 75 years, the Earth is projected to maintain a negative average annual energy balance, a state that suggests a sustained cooling phase rather than a temporary fluctuation.

1.3 Ocean Modes Turning Cold AMO and PDO

To understand the current trajectory toward a colder climate, we must first examine the internal dynamics of the Atlantic and Pacific basins, where recent shifts suggest a departure from the warm phases that dominated the late twentieth century. [8] Recent simulations using the MPI-ESM-P Earth system model indicate that this system is capable of abrupt, self-sustaining shifts that can lock the region into prolonged cold states. Specifically, an ensemble of millennium-long simulations reveals that an abrupt weakening of the subpolar gyre can trigger multicentennial cold climate regimes resembling the Little Ice Age. This mechanism does not rely on a permanent collapse of the broader overturning circulation but rather on localized feedbacks involving sea ice and freshwater export. [25][26] This weakening was driven by anomalous freshening in the upper Labrador Sea and cold conditions in the Nordic Seas, which enhanced sea ice growth and export through the Denmark Strait. [25] The resulting reduction in poleward heat transport cooled the Nordic Seas further, creating a positive feedback loop that stabilized the weaker gyre regime. [25] The simulated post-shift climate featured expanded sea ice, reduced subpolar meridional heat transport, and persistent blocking-like sea level pressure anomalies, conditions that broadly agree in magnitude and duration with paleoclimate reconstructions of the Little Ice Age. While the timing of the simulated shift around 1600 CE differs from reconstructed anomalies in the thirteenth and fourteenth centuries, this discrepancy is attributed to the dominance of internal climate variability rather than a failure of the mechanism. [25] Simulations from the MPI-ESM-P model, specifically the Past1000-R3 ensemble, provide a mechanistic understanding of how such cold regimes stabilize. In this simulation, an abrupt weakening of the subpolar gyre around 1600 separates two stationary regimes, with the post-shift cold regime persisting for at least 250 years. [25] First, reduced poleward heat transport cools the Nordic Seas, which enhances sea ice growth and export through the Denmark Strait, further freshening the Labrador Sea. [25] Second, reduced salt transport sustains this upper-ocean freshening. [25] These feedbacks demonstrate that the post-shift cold regime is stabilized by interactions between freshened upper Labrador Sea waters and expanded sea ice. Although the Atlantic Meridional Overturning Circulation (AMOC) does not exhibit a long-lasting shift, it temporarily weakens during the transition, contributing to the broader cooling signal. [26] In one specific millennium-long simulation (Past1000-R3), the SPG weakened by 0.72 Sv over two decades around 1600, separating two stationary regimes with the post-shift state persisting for at least 250 years. [25] Two positive feedbacks stabilized this weaker regime: reduced poleward heat transport cooled the Nordic Seas, enhancing sea ice growth and export through the Denmark Strait, which further freshened the Labrador Sea; simultaneously, reduced salt transport sustained upper-ocean freshening. [25] Crucially, while the AMOC temporarily weakened during the transition, the simulations establish that these abrupt subpolar gyre shifts are not associated with persistent changes in Atlantic Meridional Overturning Circulation strength. The simulated post-shift climate featured expanded sea ice, reduced subpolar meridional heat transport, and persistent blocking-like sea level pressure anomalies, broadly agreeing in magnitude and duration with paleoclimate reconstructions of the Little Ice Age. [27][25] Historical analogs provide a stark warning about the potential magnitude of such shifts. [1] The model simulations show that a rapid weakening of the subpolar gyre, driven by freshwater export from the Arctic and associated freshening in the upper Labrador Sea, can initiate a cascade of anomalous oceanic and atmospheric circulation, sea ice extent, and upper-ocean salinity changes. [25] The discrepancies in timing are not a flaw in the model but rather a reflection of the chaotic nature of internal climate variability. [25] As the research indicates, preconditioning by internal variability explains the timing discrepancies between simulated subpolar gyre shifts and reconstructed Little Ice Age onset. This finding is pivotal because it demonstrates that the ocean can spontaneously enter a cold state due to its own internal dynamics, without requiring a persistent external forcing like a grand solar minimum. [25] The ocean is not just a passive recipient of solar energy; it is an active participant in the

climate system, capable of storing and releasing heat in ways that can override short-term atmospheric trends. [28]

1.4 Echoes of the Pre Maunder Configuration

To understand the current solar trajectory, we must first look to the historical baseline established by the Maunder Minimum, a period spanning from 1645 to 1715 that serves as a primary analogue for contemporary solar behavior. [29] The Maunder Minimum (1645–1715) was a period of low sunspot numbers and reduced total solar irradiance. During this time, the sun entered a state of prolonged quietude, with observations from the mid-seventeenth century noting a significant decline in the frequency and intensity of these solar features. [30][31][32][33][34][35] These isotopic records show a distinct maximum during the Maunder Minimum, indicating that the sun's magnetic field was too weak to deflect cosmic rays effectively, a signature of low solar activity. [36] The Maunder Minimum demonstrates that the sun can enter extended periods of low activity, with significant consequences for global climate. [37]

The Maunder Minimum (approximately 1645–1715) serves as a critical historical baseline for understanding the climatic consequences of prolonged solar hibernation. [37] During this epoch, European temperatures plummeted, shortening the growing season by more than a month. This cooling was not merely a statistical anomaly but a tangible crisis that reshaped daily life and agricultural viability across the continent. [38] In the Paris region, the average monthly temperature fell below freezing eight times between 1691 and 1697, a phenomenon never again seen. [38] Further north, in Finland, long winters and early night frosts destroyed the harvest in both 1695 and 1696, causing a demographic catastrophe with population losses in some areas exceeding 40 per cent. [38] The natural archive on climate indicates that average temperatures in 1687–1700 were 1.5°C lower than in the preceding decade, leading climatologists to christen this period the climax of the Little Ice Age. [38] These oscillations, though seemingly small, had outsized impacts: since each change of 0.1°C in global temperature advances or retards the ripening of crops by one day, the cooling of the 1690s delayed harvests by an average of two weeks in temperate zones. [38] During this era, severe cold caused the Thames River and Dutch canals to freeze over, demonstrating the tangible impact of solar quiescence on regional hydrology. [8] The northern hemisphere experienced a landmark winter in 1657–58, where the canal between Haarlem and Leiden remained frozen for two months, and the Baltic froze so hard that the Swedish army marched over ice to launch a surprise attack on Copenhagen. [38] John Evelyn judged that he and his compatriots had just lived through 'the severest winter that man alive had known in England,' with crow's feet frozen to their prey. [38] Later, during the Great Frost of 1683–84, the River Thames was completely frozen for two months, with ice reaching 11 inches thick at London. [39] Solid ice extended for miles off the coasts of the southern North Sea, preventing the use of many harbors and causing severe problems for shipping. [39]

The historical record confirms that cereal grain harvest failures during the Maunder Minimum led to mass famines in Europe. This catastrophic outcome was driven by a global fall in temperature of 1° C to 2° C, caused by abnormally low solar activity in the early and mid-seventeenth century combined with major volcanic eruptions. [40][41][38] A single degree centigrade was enough to have a serious effect on growing seasons, leading to catastrophic falls in crop yields across the world. [38] In seventeenth-century Europe, a 30 percent reduction in the grain harvest often doubled the price of bread, whereas a 50 percent reduction quintupled it. [41] The most densely populated areas of the early modern world relied on a single crop: wheat or rye in Europe, rice in Asia, and maize in the Americas. [41] These staple crops constituted up to 75 percent of the population's diet, making these dynamics devastating. [38] The widespread food crises of the seventeenth century, and especially the crisis of the 1690s, have been connected to a period of low solar activity, to the Maunder Minimum (c. [42] 1645–1715). Thus, although low solar activity is likely to have contributed to the cooling conditions of the seventeenth century over the long time scale, the sudden drop in summer temperatures and resultant crop failure years across northern Eurasia resemble the signature of volcanic eruptions more than the signal of solar activity. The case of seventeenth-century Southern Ostrobothnia demonstrates that this forcing can fundamentally challenge human lives more than ten thousand kilometres away from the physical source of the eruption. [40]

The late seventeenth century serves as a critical baseline analogue for understanding current solar behavior, particularly the period known as the Maunder Minimum (approximately 1645-1715). [37] Such dramatic reductions, extending beyond a single eleven-year cycle, are classified as grand solar minima. [43] During these periods, the Sun exhibits specific physical traits that distinguish it from active phases. [44]

The historical record provides a critical baseline for understanding the potential climatic consequences of prolonged solar quiescence, particularly when examining the Maunder Minimum period that spanned approximately 1645 to 1715. [37] This era is widely regarded as the most prominent recent instance

of reduced solar activity, characterized by a distinct lack of visible sunspots as documented by Eddy 1976, alongside increased concentrations of cosmogenic isotopes such as carbon-14 and beryllium-10 that indicate a more quiescent heliospheric magnetic field. [45] Paleoclimate reconstructions, including tree-ring data from northern North America analyzed by Jacoby and D'Arrigo 1989, reflect the general coldness associated with the Little Ice Age during this seventeenth-century window, suggesting that global or Northern Hemisphere temperatures were approximately 0.5 degrees Celsius colder than today, with extratropical regions experiencing cooling closer to 1 degree Celsius. [45] 1999 and Mann et al. 2003, supports a significant thermal anomaly.

1.5 Why This Book and How It Argues

This book provides the evidence and the argument for this approach, challenging the current narrative of anthropogenic global warming. [46]

The book asserts that IPCC temperature and CO2 records are selective, inaccurate, or based on discarded data. This critique establishes that the Intergovernmental Panel on Climate Change's depiction of the temperature history over the past 10,000 years is selective and plain wrong, contradicting the actual data record. [7] Furthermore, serious questions regarding the accuracy of the IPCC's claimed record of atmospheric CO2 over the past 150 years demonstrate that many measurements have been discarded because they do not agree with the approved story. Additionally, the study identifies significant errors in the IPCC reports, showing that the 39 computer models used by the panel fail validation against measured surface temperature changes. [47]

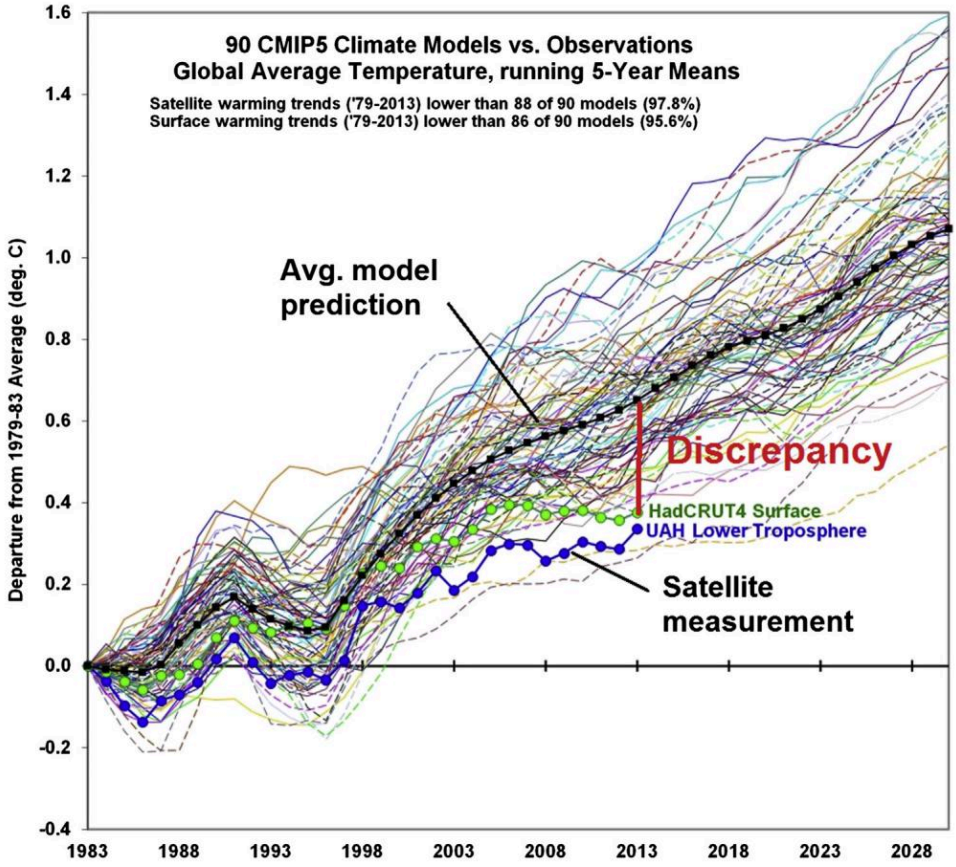

Figure 1.1: This line graph compares 90 CMIP5 climate model predictions against satellite and surface temperature observations from 1979 to 2013, plotting the departure from the 1979–83 average in degrees Celsius. The graph shows numerous model projections (colored lines) and an average model prediction (black line) that generally trend above the observed data from HadCRUT4 surface measurements (green dots) and UAH lower troposphere satellite measurements (blue dots), with a highlighted discrepancy indicating that most models overestimate warming trends. (source: ref 8)

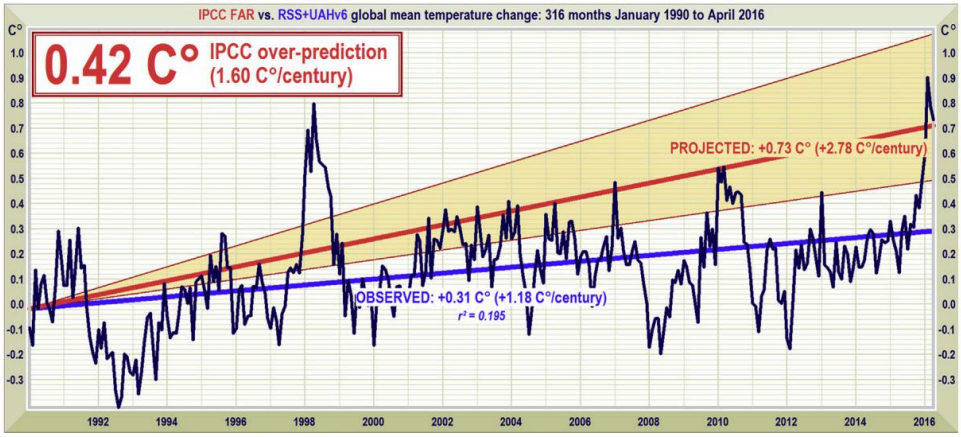

Figure 1.2: This line graph compares observed global mean temperature change (1990–2016) from RSS+UAHv6 satellite data against IPCC FAR projections, showing a 0.42 °C over-prediction (1.60 °C/century) relative to the observed trend of +0.31 °C/century (r^2 = 0.195). The observed data (black line) fluctuates around the projected trend (red line), with the projected warming (0.73 °C/century) falling outside the observed range, indicating a significant divergence between historical observations and the IPCC FAR projection. (source: ref 8)

The author posits that solar variability, specifically a 'hibernation' or cold spell, is the primary driver of current climate change. This perspective establishes that a historic reduction in the energy output of the Sun has begun, signaling the end of global warming and the start of a new, potentially dangerous cold climate. [46] The evidence demonstrates that this significant climate change event is coming, with the most likely outcome being widespread global loss of life and social, economic, and political disruption. [46] Understanding this shift is essential for preparing for the inevitable cold and difficult years to come. [46] Adaptation involves practical adjustments to clothing, transportation, and the design of homes and businesses, alongside a deeper understanding of cold-weather health hazards. [50] Given that Little Ice Age conditions could strangle food production and trigger famines, the plan emphasizes techniques for long-term food storage. [51] Furthermore, because massive ice storms and blizzards can cause widespread electrical outages that render modern electric heating systems useless, the strategy highlights the critical need for backup heat sources that do not rely on electricity. Consequently, the text demonstrates that individuals and communities must prepare for a scenario where they cannot rely on external aid, whether from their own national governments or from foreign powers. The book's mission, therefore, is to alert readers to this reality before it becomes an immediate crisis. [46] The narrative emphasizes that staying silent about these discoveries would be a disservice to the public, especially given the potential for a "long depression" or severe economic recession tied to the cooling trend. [46] Thus, the text proves that a shift toward self-reliance is not just advisable but essential for navigating the upcoming decades.

The chapters that follow build the case in sequence. Chapter 2 traces the rhythm of past cold and warm periods, showing that abrupt climate swings are the historical norm rather than the exception. Chapter 3 lays out the tools of solar science — how sunspots are counted and the Sun's output is measured. Chapter 4 turns to Zharkova's two-wave dynamo and its forecast of a grand minimum. Chapter 5 follows the Sun's own motion about the solar system's centre of mass, the planetary clock behind those cycles. Chapter 6 examines the cloud hypothesis — how cosmic rays, modulated by solar activity, may seed the clouds that cool the Earth. Chapter 7 explores the underground connection between a quiet Sun and a restless crust. Chapter 8 confronts the attribution question head-on, weighing the Sun against carbon dioxide. And Chapter 9 asks what a prudent society should do now to prepare for a colder few decades.

2. History of Past Cold and Warm Periods

Reconstructed solar activity shows ~5 deep minima and ~4 sustained maxima since antiquity, each tracking documented climate and societal impact.

2.1 Cosmogenic Isotopes as a Solar Proxy

To reconstruct solar activity beyond the brief era of direct observation, scientists rely on cosmogenic isotopes that serve as natural archives of cosmic-ray flux. [43] Among these proxies, Beryllium-10 (^{10}Be) concentrations are measured in Greenland ice cores such as Dye-3. These ice cores provide a continuous record of atmospheric deposition, allowing researchers to trace variations in solar modulation over millennia. [52][53][54][55][56][57] The precision of these records is crucial for understanding the long-term behavior of the Sun and its impact on Earth's climate system. [58]

The production of beryllium-10 (^{10}Be) in the atmosphere serves as a sensitive recorder of solar modulation, particularly because the solar wind's magnetic field shields Earth from galactic cosmic rays. [55] When solar activity is high, this shielding effect is enhanced, reducing the flux of cosmic-ray protons that generate ^{10}Be. [55] For instance, high-resolution records from Law Dome ice in East Antarctica show a highly significant correlation ($r_{xy} = 0.64$) between ^{10}Be concentrations and neutron monitor data, which directly measures cosmic-ray intensity. [59] Furthermore, comparisons with the Greenland Ice Core Project data reveal that ^{10}Be time series can differentiate between the strengths of solar minima even when sunspot numbers drop to near zero, such as during the Maunder Minimum. This sensitivity confirms that ^{10}Be provides a continuous record of the open solar magnetic field, independent of the threshold effects that obscure sunspot observations during grand minima. [55] Thus, the cosmogenic isotope record faithfully registers solar centennial variability, offering a critical tool for understanding long-term solar-climate interactions beyond the limited span of direct sunspot observations.

Ice-core archives from Antarctica and Greenland preserve beryllium-10 (^{10}Be), a cosmogenic isotope whose atmospheric production is modulated by solar activity. [33] These temperature anomalies, derived from various paleoclimate records, show a remarkable correlation with cosmic-ray variations inferred from isotopic data. [60] The resulting ^{14}C production rate (p ^{14}C) reflects the flux of incoming cosmic ray particles, which are modulated by the solar magnetic field. [61] This inverse relationship establishes ^{14}C production rates as a robust indicator of solar variability. [62] For instance, the maximum ^{14}C production rate in the last millennium occurred between AD 1645 and 1715, coinciding with the Maunder Minimum when sunspots were almost lacking. [32] In contrast, ^{14}C concentration in tree rings can be influenced by changes in the global carbon cycle, complicating the isolation of solar signals. The first principal component explains 69% of the total variance, implying that ^{14}C production changes throughout the Holocene are very similar to the ^{10}Be changes found in polar ice cores from two different hemispheres. [52] Simulations starting at 500 BC using ^{10}Be-derived production from Antarctic ice show a good match with IntCal04 atmospheric ^{14}C variations in both amplitude and phase, with correlation coefficients (r^2) close to 0.9. [63] Consequently, long-term reconstructions rely on proxy evidence from natural archives, specifically cosmogenic isotope concentrations preserved in dendrochronologically dated tree rings and ice cores. Among these proxies, Carbon-14 (^{14}C) isotopes are extracted from ancient tree rings for solar proxy analysis, providing a reliable archive of past solar activity on time scales of years to centuries and millennia. This radiocarbon record establishes that radiocarbon production in the atmosphere, and consequently in tree rings, is owing to a cosmic ray flux which has significantly varied, being in inverse relationship with solar activity. [64][65][66][67] The longest and most precise annual ^{14}C dataset, created by Brehm et al. using 13 oak timbers from buildings in the UK and Switzerland covering the period 969–1933 CE, demonstrates the persistence of the 11-year Schwabe cycle throughout the last millennium. [65] These annually resolved paleoclimatic and solar proxies from the same calendar-dated tree-ring sequence confirm a direct influence of the Schwabe cycle on climate, reaffirming that ^{14}C in tree-ring chronologies can provide robust information on solar variability. [65] Furthermore, the regularity of longer cycles, such as the 178.7-year cycle, is sometimes disturbed, with patterns of solar minima like the Spörer and Maunder types recurring in steps of approximately 2402 years. By correcting for obfuscating variables such as the strength of the geomagnetic field, a function called the solar modulation potential is derived,

which reveals the activity of the Sun over time via changes in cosmogenic isotope production. [64] This method confirms that the radiocarbon record in tree rings provides a reliable archive of past solar activity, allowing researchers to reconstruct solar behavior far beyond the reach of instrumental records. [43]

2.2 Pre Maunder Grand Minima

This period of reduced solar activity is further corroborated by auroral records; continuous Chinese observations from 900 A.D. to 1200 A.D. indicate that auroral activity was relatively weak during 1010–1050 A.D., consistent with the grand minimum conditions of the Oort Minimum. [68] The lack of auroral evidence in "The Poetic Edda," assembled in southern Norway between 1000 and 1100 A.D., also aligns with the reconstructed auroral zone and the weak solar activity characteristic of the Oort Minimum. [68]

Solar activity reconstructions reveal distinct periods of prolonged low output, or grand minima, scattered across the historical record. [43] 1050, a signal inferred to indicate a period of minimum solar activity known as the Oort Minimum. This specific interval, spanning roughly from 1010 to 1070 or 1080, is identified in adjustment-free solar activity reconstructions as one of four grand minima since the year 1000 A.D., alongside the Wolf, Spörer, and Maunder events. The elevated $\Delta^{14}C$ levels during this time confirm reduced solar modulation, as higher radiocarbon production corresponds to lower sunspot numbers in the inverted scale of the record. While some extratropical Northern Hemisphere temperature reconstructions do not explicitly highlight the Oort Minimum as a distinct cold anomaly, the cosmogenic isotope data establishes the solar quiescence. The timing of this minimum aligns closely with grand perihelion coincidences of Saturn, Uranus, and Neptune near the year 1050, suggesting a planetary association with Oort-type solar activity. These independent lines of evidence from radiocarbon dating and orbital mechanics suggest that the Oort Minimum was characterized by significantly reduced solar activity. Although the direct temperature signal in some proxy records is less pronounced than in later minima like the Maunder, the solar reconstruction confirms the event's occurrence and duration. The consistency between the $\Delta^{14}C$ peak and the solar activity reconstruction is consistent with the existence of this early grand minimum in the Holocene record. [31][19][2][63][69] The resulting ^{10}Be record spans approximately from year 840 AD to year 1980 AD, offering a near-decadal resolution with an average of 8 years per sample. [63] This resolution corresponds to a mean accumulation rate of about 7 cm water equivalent per year. [63] The reconstruction of Φ based on stacked records and a constant mixing scheme compares quite well with the one of McCracken et al. based on the South Pole record and their mixing model "M3" (Fig. [63] 5), with three marked differences. First, the Spörer Minimum corresponds to the weakest activity in our reconstruction, even after removing the lowest values around year 1456 AD. [63] Another important difference is a secondary maximum centered around year 1220 AD in the South Pole reconstruction, which does not exist at all in our stack. [63] A third important difference concerns the rank of the minima: in our stack the Spörer is the lowest minimum, followed by the Maunder, Wolf, Oort, and Dalton Minima, that is, the Oort and Maunder Minima are higher than in the McCracken et al. reconstruction. [63] The maximum of Φ is found during the 20th century based on the raw Φ values, but during the 8th century based on smoothed Φ values. [63] As discussed in Sect. 3.3, trends in snow accumulation have probably biased the relative values of Φ , and this would affect the rank of the reconstructed solar Minima and maxima. [63] In particular, the expected decrease in snow accumulation during the 16th and 17th centuries would have increased ^{10}Be concentration and biased Φ towards lower values. [63] However, this bias would not (or less) apply to our reconstructed Spörer Minimum and would even lower the Maunder Minimum. Specifically, large volcanic eruptions caused short-term climatic effects, including cooler temperatures over several months due to reduced solar irradiation. This distinction is vital because stratospheric aerosols affect the global radiation budget by absorbing and, more importantly, backscattering incoming solar radiation, which causes a cooling of the lower atmosphere and the surface. [70][1][71] Statistical studies using superposed epoch analysis have identified a statistically significant average temperature decrease of about 0.2 to 0.5°C for 1 to 3 years following the times of known nineteenth and twentieth century eruptions. [70] However, this volcanic signal is transient; surface temperatures recover in a few years as the aerosols decay, meaning that volcanic forcing cannot account for the multi-decadal or centennial cooling trends observed during the Sumerian, Egyptian, or Roman minima. The volcanic signal expected in hemispheric or zonal surface temperature records in historical times is about the same as the background interannual variations in temperature, requiring careful compositing to isolate the signal from noise. [70] Therefore, when we observe sustained cooling periods that align with low solar activity in ^{10}Be and ^{14}C records, we are not looking at the aftermath of volcanic winters, which are brief and intense, but rather at the prolonged dimming of the Sun itself. Thus, the pre-Maunder record stands as a testament to solar dominance on decadal to centennial scales, independent of the short-term volcanic noise that punctuates the instrumental era.

2.3 The Maunder and Dalton Minima Up Close

Furthermore, the cosmogenic record detects the Hallstatt 2,400-year cycle across the Holocene, suggesting a deep, rhythmic structure to solar output that predates the instrumented era.

Chapter 7 tells the Tambora story in full — the 1815 eruption, the 'year without a summer,' the failed harvests from New England to Finland. Here it is enough to note that the Dalton Minimum's most infamous years were a volcanic exclamation point set inside an already sun-starved climate.

The Dalton Minimum was an active period for volcanic activity, a fact that highlights the complex interplay between solar and geological forcing during this era. [79] In addition to the massive Mount Tambora eruption, La Soufriere on Saint Vincent erupted in 1812, as did Mayon in the Philippines in 1814. These concurrent events highlight how multiple geological disasters can compound cooling effects. [46] [77] This overlap challenges simple attributions of climate change to a single driver, showing instead a period where solar hibernation and volcanic particulates likely worked in tandem to depress global temperatures. [80] The historical record thus suggests that the Dalton Minimum was not merely a solar phenomenon but a time of compounded climatic stress from both celestial and terrestrial sources. [81] Post described as the "last great subsistence crisis in the Western world." As the sun went quiet during this interval, the Earth began to slowly cool, delaying the start of the planting season and limiting the harvest with early frost in the fall. [82] While modeling studies show a large range of simulated climate responses to solar forcings, with some attributing most cooling to volcanic effects, other analyses suggest solar cooling was a significant force for lower temperatures during the Dalton Minimum. For instance, Shindell et al. concluded that volcanic eruptions have rather strong but only short-lived effects on temperatures, while the reduction of the solar irradiance during the grand minimum affects temperatures on longer timescales. [82][79][45][1][46] Archibald (Australia), Duhau (Argentina), and Theodor Landscheidt (Germany) forecasted that the sun would enter a period similar to the Dalton Minimum or a more severe "Grand Minimum" in Solar Cycle 25 — within the 2020–2053 window this book adopts. [83] These forecasts underscore the potential for future solar minima to impact global temperatures and societal stability, echoing the severe conditions of the Dalton era. [46] The combined effects of volcanic eruptions and solar irradiance decrease could significantly modify global mean temperatures, with Wagner and Zorita showing modifications by up to several tenths of a degree. [79] However, the exact solar forcing used in some modeling studies remains unknown, highlighting the complexity of isolating solar impacts from other climatic factors.

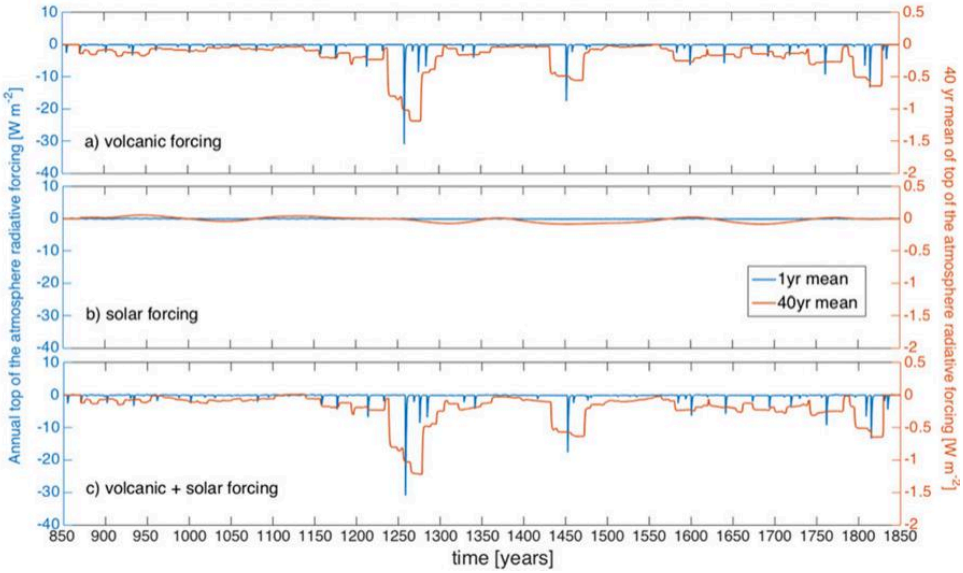

Figure 2.1: This figure displays three time series plots of top-of-atmosphere radiative forcing in W m^{-2} from 850 to 1850 CE, showing annual average volcanic forcing (a), solar forcing (b), and their sum (c). The blue lines represent 1-year running means, while the orange lines show 40-year running means, with the right y-axis corresponding to the 40-year mean values. Volcanic forcing exhibits large, short-term negative spikes, particularly around 1250 and 1800 CE, while solar forcing remains relatively stable with minor fluctuations. The combined forcing (c) reflects the sum of both components, with the 40-year mean (orange) smoothing out short-term variability. (source: ref 84)

2.4 Grand Maxima and Societal Abundance

Rather than a monolithic warming trend, the region experienced a distinct seesaw of precipitation conditions between the western and eastern basins, where the west often faced arid conditions during positive North Atlantic Oscillation periods, while the east sometimes experienced more humid conditions despite the broader NAO impact. [85] This regional divergence was driven by the interplay of multiple climate patterns, including the North Sea-Caspian Pattern, defined by the pressure difference between the North Sea and the Caspian Sea, which brought cool and dry winter conditions to the central and eastern Mediterranean when positive, and warm and wet conditions when negative. [85] Furthermore, the influence of a strong Siberian High could channel unusually cold airflow from Inner Eurasia into the eastern Mediterranean and the Middle East, contributing to rare phenomena such as snowfall and frost in Baghdad, events that were described several times during the Oort Minimum of the 11th century. These specific meteorological dynamics demonstrate that the Medieval Climate Anomaly in the Eastern Mediterranean was spatially and temporally incoherent, punctuated by recurring anomalies. Such variability underscores the necessity of examining regional climate drivers rather than relying on hemispheric averages, as local socio-political dynamics in the Byzantine Empire were likely shaped by these fluctuating environmental conditions rather than a steady thermal trend. [85][86] Elena Xoplaki and co-authors combined evidence of economic and demographic growth in Byzantium between 850 and 1300 CE with new findings from palynology, alongside documentary textual evidence and natural proxies for the Balkans and Asia Minor. [85] Their analysis identified potential links between climatic and societal changes, specifically noting correlations between a long-term trend towards wetter conditions in western Anatolia around AD 850–1000 and stable, relatively warm-wet conditions in northern Greece during AD 1000–1100. [85] Based on a marine record from the Athos basin in Northern Greece, they reconstructed changes in sea surface temperatures and other palaeoenvironmental factors. [85] Their data suggests a cooling trend from ca. [87] 500 to 850 CE, followed by a warming trend from ca. [85] 850 to 950 CE in the Northern Aegean. [85]

Palynological data, specifically pollen records from Asia Minor and the Southern Balkans, confirm a significant increase in agricultural cultivation across the Byzantine Empire beginning in the late 9th and 10th centuries, following a notable decline between the 6th and 8th centuries. [85] This expansion included intensified production of cerealia, olives, and wine, alongside shifts toward pasturage and animal husbandry, reflecting regional variations in land use. [85] Alexander Olson's study on oak and olive cultivation in the middle Byzantine period demonstrates that this economic upsurge and agricultural intensification were consequences of greater pressure for surplus from elite figures, rather than demographic growth alone. [85] The data shows that modest landscape modifications and slow agricultural growth characterized the 10th and 11th century Aegean provinces, with more significant economic dynamics emerging only in the late 11th century. [85] This later period was driven by a Komnenian-led Byzantine state demanding higher tax revenue, an emerging class of big landowners seeking rent, and Italian merchants trading across the Aegean's waters, which pressured peasants to produce a surplus that garnered coins on the market. [85] In 1069, for instance, the winter in Germany was harsh and long, causing rivers to freeze and leading to a significant shortage of wine and fruit due to the extreme cold. [39] These concurrent extremes demonstrate the global reach of climatic anomalies during this period. [3] In England, the year 1069 saw a great dearth, exacerbated by Norman conquests, where peasants resorted to cannibalism and sold themselves into slavery to survive. [39]

The Oort Solar Minimum (ca. 1010–1080) was characterized by reduced solar activity and cooler global average temperatures. An adjustment-free reconstruction of the solar activity over the last three millennia confirms four Grand minima since the year 1000A.D, including the Oort (1010–1070) period. The smoothed MDVM reconstruction exhibited a general agreement with the variation of the reconstructed total solar irradiance, with a significant correlation ($r = 0.498$, $edf = 34$, $p<0.01$) during the common period 849–2000 AD. The relatively cold conditions between the two warm peaks around AD 1000 and 1100 seemed to be related to the Oort Minimum. Several of the periods with especially low solar activity are also visible in the reconstruction, such as the Wolf Minimum (c. [19][88][2][89] This complex climatic backdrop did not necessarily cause societal collapse in Byzantium or neighbouring polities; instead, it appears to be consistent with long-term economic expansion for certain times, suggesting that the empire possessed significant resilience against exogenous shocks. [85] A detailed examination of the winter of 927–28 illustrates this dynamic clearly. [85] Rather, the long winter was later connected with what the state and the peasants perceived as a socioeconomic crisis, serving as a lens through which contemporaries understood the reasons for social transformation. [90] The environmental stressor, even if it was not the harshest winter of the tenth century in physical terms, impinged upon the complex web of crop ecologies, social relations, and the state's interests. [90] It added new momentum to extant social dynamics, specifically

the trend of office-holding elites accumulating wealth to become an increasingly powerful social group. [85] While Byzantine society as a whole proved resilient, surviving the crisis, the price for this resilience was a significant shift in the balance of socioeconomic relations. [90] The winter offered an opportunity for the more affluent to exploit peasants whose livelihoods depended on ecological niches incapable of withstanding prolonged cold spells. [90] Thanks to buffers such as existing estates, accumulated gold, and local connections, elite groups could exploit local subsistence crises across the provinces to improve their situation relative to both the producing population and the state. [90] This suggests that environmental stressors stimulated social evolution rather than causing direct collapse. [90] Recent regional studies, including pollen data from Lake Belevi and Bafa Gölü, alongside written records like the 1073 charter for Andronikos Dukas regarding flood-damaged estates in the Maeander delta, support this nuanced view. [85] These archives inform us about short-term localised events and long-term trends, allowing for a more detailed description of the resilience of rural and urban communities. [85]

2.5 The Long Cycles Hallstatt Eddy Bray

This perspective raises serious concerns about a coming ice age in several thousand years, rather than catastrophic warming from greenhouse gas emissions on the timescale of the 21st century. [8] If Vinós' analysis is correct, the belief that we can control Earth's climate by reducing CO_2 emissions may turn out to be the greatest folly of the 21st century, underscoring the need for a broader debate on the true drivers of climate change. [1]

Climate models employing reductions in total solar irradiance of 0.4%, 0.25%, 0.12%, and 0.08% indicate that even a 'grand' minimum state would only partly reduce global mean temperature by 0.1 K, or delay the projected rise. [91] More moderate scenarios result in an even weaker signal, while recent experiments with a 0.12% reduction apportioned across the spectrum, or a larger 0.85% reduction in UV irradiance alone, show regional responses in the Northern Hemisphere that do not appear to scale linearly with the forcing magnitude. [91] These simulations suggest that a hypothetical grand solar minimum would offset only approximately 0.2 K of anthropogenic warming. Consequently, such a solar downturn is unlikely to significantly alter the long-term warming trend driven by greenhouse gas emissions. [92] These higher estimates imply that solar forcing could be important for climate variability, particularly if the irradiance from the quiet Sun varies significantly over time. [93] Some studies utilizing these high solar variability TSI estimates argue that solar forcing dominated long-term warming since the 19th century, suggesting that the solar contribution to observed temperature increases may be larger than previously thought. [94] Consequently, the relative importance of solar forcing in recent warming trends continues to be a subject of significant scientific debate.

Solar forcing of Earth's climate operates through both direct and indirect processes, with the simplest direct mechanism involving variations in solar radiative output. [95] While currently believed too small to have had a dominant influence on surface climate, variations in solar irradiance may have been larger back in time. [96] Indirect effects include solar-induced changes in atmospheric transparency influencing the radiative budget of the planet. [95] One possibility is that changes in the solar output of ultraviolet (UV) radiation affects temperatures in the stratosphere through absorption by ozone, which has the potential to influence the large-scale dynamics of the troposphere. [95] During solar maxima, the energy in the UV spectrum can be several percent higher than during solar minima. [60] Consequently, while solar variability contributes to natural climate fluctuations, it is generally considered a minor factor compared to anthropogenic greenhouse gas emissions.

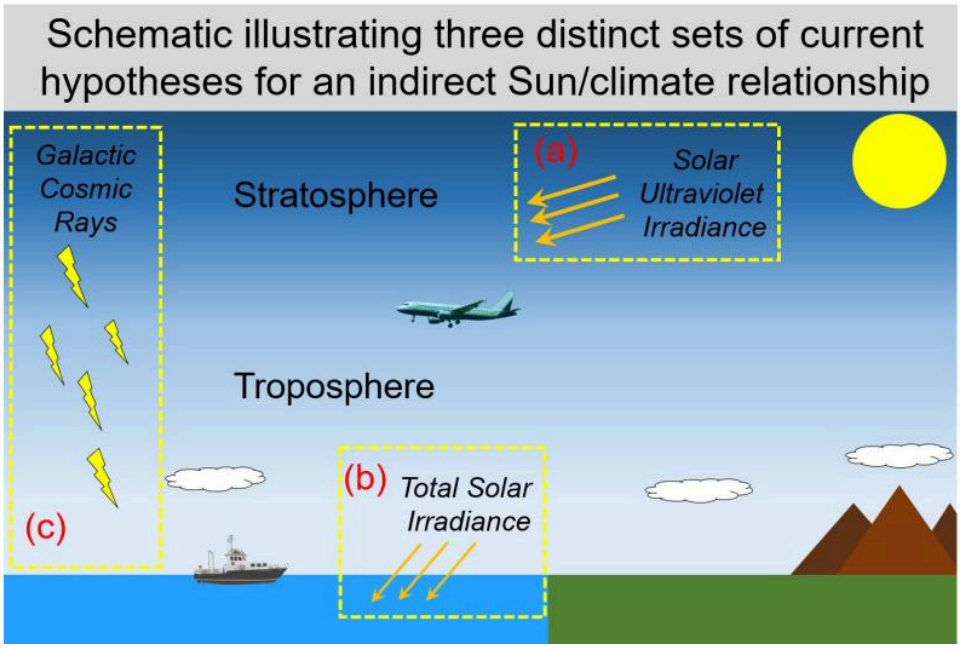

Figure 2.2: This schematic illustrates three proposed mechanisms for indirect solar influence on Earth's climate. Panel (a) shows solar ultraviolet irradiance affecting the stratosphere, with a top-down pathway to the troposphere and surface. Panel (b) depicts total solar irradiance impacting the troposphere and oceans, representing a bottom-up mechanism. Panel (c) illustrates galactic cosmic rays modulated by solar activity, with a proposed influence on the troposphere and stratosphere. The diagram contrasts the vertical pathways of solar forcing across atmospheric layers. (source: ref 94)

Porter demonstrates that sulfur-rich aerosols generated by volcanic eruptions are a primary forcing mechanism of glacier fluctuations and climate on a decadal scale, suggesting volcanic impacts as a dominant driver of interannual-to-decadal Northern Hemisphere temperature variability. The study shows that episodes of glacier advance consistently associate with intervals of high average volcanic aerosol production, inferred from acidity variations in a Greenland ice core. [97][73][52] Specifically, advances occur whenever acidity levels rise sharply from background values to reach concentrations $\geq 1.2\ \mu equiv\ H^{+}/kg$ above background. [97] A phase lag of about 10–15 yr, equivalent to reported response lags of Alpine glacier termini, separates the beginning of acidity increases from the beginning of subsequent ice advances. [97] The amount of surface cooling attributable to individual large eruptions or episodes of eruptions is similar to the probable average temperature reduction during these advances, ca. $0.5^{\circ} - 1.2^{\circ}C$, as inferred from depression of equilibrium-line altitudes. [97] This climatic shock coincided with the political transition from the Roman Republic and Ptolemaic Kingdom to the Roman Empire, a period marked by unusual climate, crop failures, famine, disease, and unrest in the Mediterranean, suggesting significant vulnerability to hydroclimatic shocks in ancient states. These findings imply that such environmental stressors may have exacerbated existing political tensions, potentially accelerating the collapse of established regimes. [98][99][100][101]

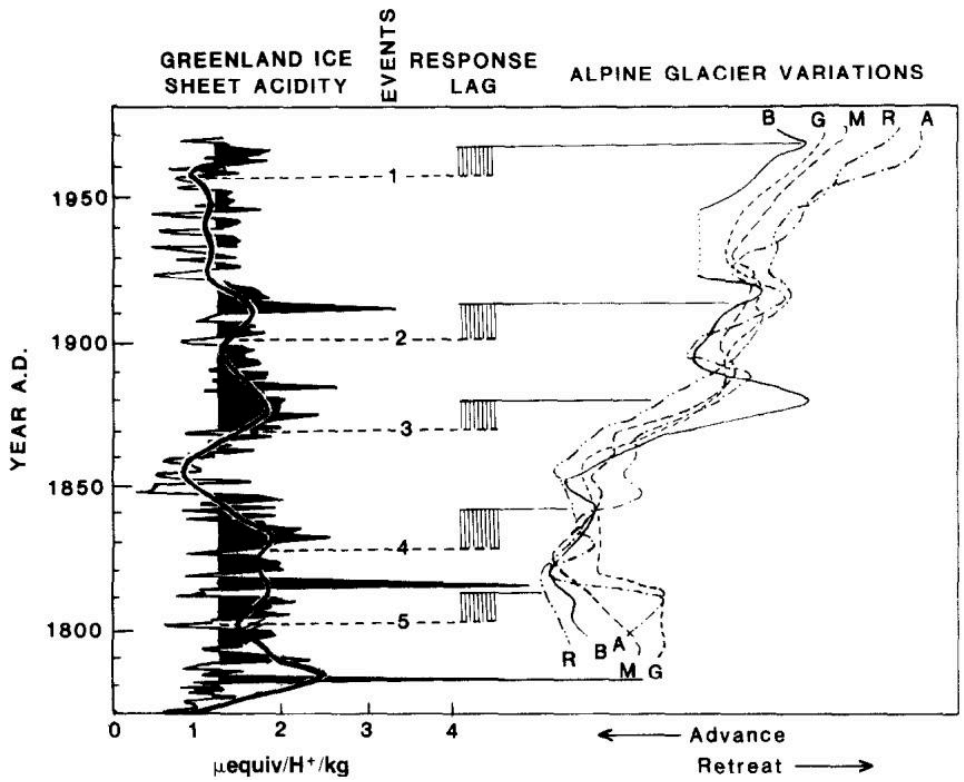

Figure 2.3: The figure displays a time series comparing the 2-year average acidity profile of the upper Greenland Ice Sheet, with a 11-point Gaussian filtered curve and shaded regions indicating values above background levels, against five Alpine glacier variations (Argentière, Brenva, Unter Grindelwald, Mer de Glace, Rhone) from 1800 to 1950 A.D. Dashed horizontal lines mark the onset of acidity events exceeding 2.4 μequiv H^+/kg, and shaded zones to the right of the Greenland acidity curve illustrate the response lag, showing that glacier advances lag behind acidity peaks by 1–2 decades. (source: ref 97)

Model simulations using the MPI-ESM-P ensemble suggest an abrupt weakening of the subpolar gyre around 1600, driven by anomalous Arctic freshwater export into the Labrador Sea. This shift, observed in the Past1000-R3 simulation, indicates a reduction in gyre strength of 0.72 Sv over two decades, separating two stationary regimes. [25][26] The mechanism appears to be stabilized by positive feedbacks: reduced poleward heat transport cools the Nordic Seas, enhancing sea ice growth and export through the Denmark Strait, which further freshens the upper ocean. [25] These simulated changes, including expanded sea ice and reduced subpolar meridional heat transport, are consistent with paleoclimate reconstructions of Little Ice Age-type episodes, despite timing discrepancies attributed to internal climate variability. [25] Iversen to refine postglacial period zonation and establish a summer vegetation-based temperature scale for the Scandinavian Holocene by the 1940s. [1] These efforts produced Holocene climate reconstructions that closely mirror current understanding, revealing that the Holocene climate can be subdivided into periods of distinct climatic conditions, as illustrated in a diagram by Rutger Sernander from 1912. [1] The resulting vegetation stages allow for the distinction of a 2500-year vegetation and faunal cycle, with some botanists like Sernander proposing that transitions between periods were abrupt rather than gradual. [1] Specifically, Sernander linked the last transition between the Sub-Boreal and the Sub-Atlantic, occurring around 650 BC, to the "Fimbulvintern," or Great Winter of the Sagas, which marks the end of the Nordic Bronze Age and rendered the Nordic countries a colder place. [1]

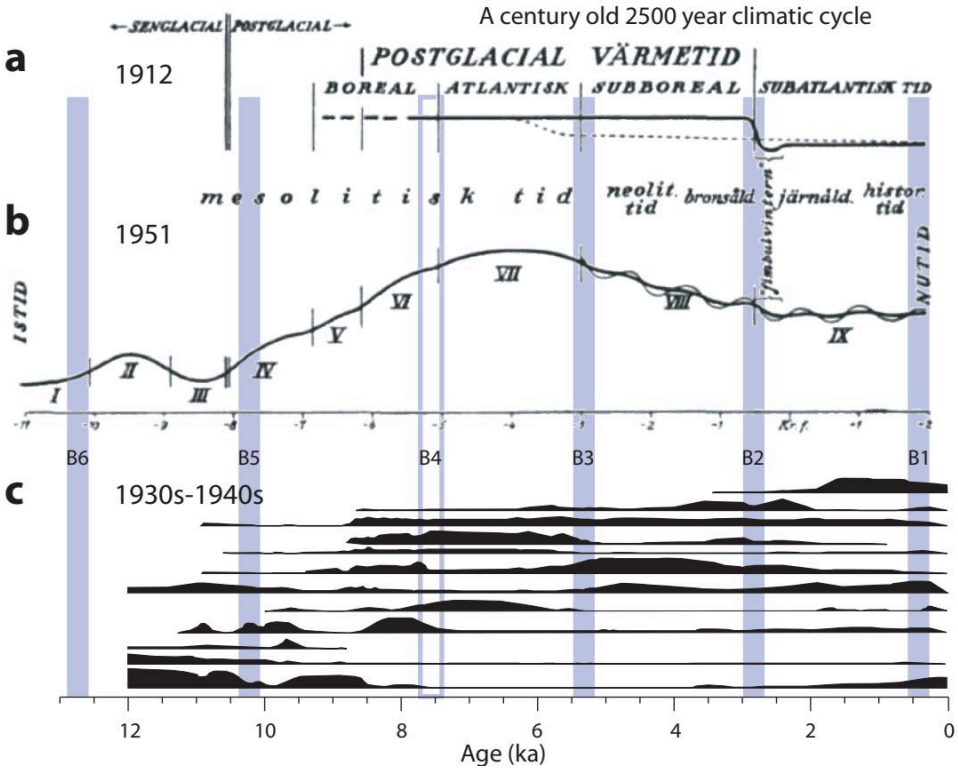

Figure 2.4: This figure presents three historical reconstructions of postglacial climate and vegetation in southern and central Sweden from the early 20th century. Panel (a) shows Rutger Sernander's 1912 model of abrupt climate degradation at the Sub-Boreal/Sub-Atlantic transition, labeled "fimbulvintern," contrasted with G. Andersson's gradual temperature evolution. Panel (b) displays Magnus Fries' 1951 diagram of temperature evolution based on pollen zones (I–IX), with a thin line indicating a near-millennial humidity oscillation. Panel (c) illustrates analytical pollen zones from the 1930s–1940s, confirming Sernander's climatic framework, with blue vertical bars marking the 2500-year Bray cycle. All panels use a common age scale in thousands of years before present (ka), with dates in CE calendar years. (source: ref 1)

3. Solar Science Foundations

The instrumented solar record — sunspot counts, magnetic indices, F10.7, TSI — is the toolbox every later chapter draws on.

3.1 From Galileo to the Photoheliograph

The history of solar observation begins not with the naked eye, but with the lens. [43] By the late seventeenth century, astronomers like Cassini and Flamsteed were tracking the frequency of these spots with increasing regularity. [102] Cassini noted that spots were more frequent in 1676 than in the twenty years preceding, while Flamsteed lamented their rarity in the years following. [102] The sunspot number, a key metric in solar physics, traces its lineage back to these early observations. [58] The legacy of 1610 is thus not just a historical footnote, but the starting point of the solar record that underpins our current understanding of solar variability. [43] This method allowed for relatively good solar images and remained in use until the late 18th century. [43] The first known observation of a sunspot using a camera obscura was done by Kepler in May 1607, who erroneously ascribed the spot on the sun to a transit of Mercury. [43] Although such observations were sparse and related to other phenomena, such as solar eclipses or transits of planets, there were also regular solar observations by camera obscura. [43] For example, about 300 pages of logs of solar observations made in the cathedral of San Petronio in Bologna from 1655–1736 were published by Eustachio Manfredi in 1736. [43] These records demonstrate that observations and drawings made using camera obscura can be regarded as instrumental observations, despite predating widespread telescope use. This classification is crucial because it establishes a continuous record of solar activity that bridges the gap between naked-eye sightings and the systematic telescopic surveys that followed. [103] [104][102][105]

The sunspot number stands as the most common and longest available index of solar activity, serving as a synthetic index useful for the quantitative representation of overall solar activity outside the grand minimum. [43] However, this series has big uncertainties before 1900, and fragmentary non-instrumental observations of the sun before 1610, while giving a possible hint of relative changes in solar activity, cannot be interpreted in a quantitative manner. Daily records of sunspot observations have formed an essential basis for evaluating long-term solar activity since 1610, a data series often considered one of the longest ongoing scientific experiments in modern science. [103] After the initial modern compilation of the comprehensive data set of sunspot group number in Hoyt & Schatten (1998a, 1998b), recent studies have continuously recalibrated and improved these data series to revise the overall long-term trends. [103] Investigations of the original observational records have formed the basis for these analyses, offering a ground truth for further recalibrations using sophisticated methods. [103] The standard sunspot number index is available from 1610 AD onward, though data quality degrades significantly in earlier periods. Consequently, interpretations of solar activity prior to the twentieth century should be treated with caution due to these inherent observational limitations. [106][103][104][107][108][109] This adjustment, attributed to Max Waldmeier, significantly altered the Relative Sunspot Number, creating a discontinuity in the ratio between the Group Sunspot Number and the Standard Sunspot Number around 1945. [110] However, systematic searches of historical drawings from the Greenwich Photoheliographic Programme suggest that the earlier observer, Wolfer, did not apply this weighting scheme, as no such spots were found in the records for which weighting was allegedly applied at Zürich. This finding is consistent with the absence of any mention of a weighting scheme in Wolf's and Wolfer's meticulous yearly reports in the *Mittheilungen über Sonnenflecken* series. [58] Consequently, the apparent continuity of the record masks a fundamental shift in observation protocols, where the Locarno Station, serving as the modern reference site, continues to apply Waldmeier's weighting, thereby carrying the effect fully into the current sunspot number maintained by SIDC in Brussels. Thus, the recovery of lost notebooks is not an antiquarian exercise but a necessary step to establish a reliable baseline for comparing modern satellite-era measurements with pre-telescopic reconstructions.

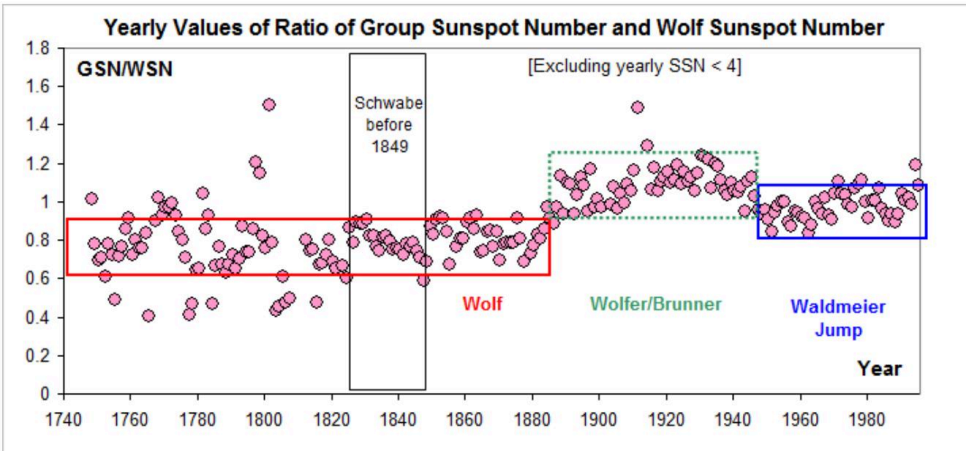

Figure 3.1: This scatter plot displays the yearly ratio of Group Sunspot Number (GSN) to Wolf Sunspot Number (WSN) from 1740 to 1990, excluding years where the Wolf Sunspot Number is less than 4. The vertical axis represents the GSN/WSN ratio, while the horizontal axis shows the year. The data points reveal a distinct shift in the ratio over time: values are clustered around 0.8–1.0 prior to 1849, with a notable increase beginning around 1849, followed by a more stable period from approximately 1900 onward. The plot highlights the "Waldmeier Jump" and labels historical periods including the Schwabe cycle before 1849, the Wolf era, and the Wolfer/Brunner era. (source: ref 58)

3.2 Cycle Metrics Schwabe Hale Butterfly

This variability is anchored by the Schwabe cycle, an approximately 11-year period of solar activity that serves as the primary heartbeat of the solar dynamo. [111] Space-borne measurements of total solar irradiance (TSI) and spectral solar irradiance (SSI) clearly establish this 11-year cycle, showing that while the overall energy output varies by only about 0.1%, the ultraviolet spectrum fluctuates by several percent, particularly in the 200–250 nm range. This modulation is not merely a surface phenomenon but is deeply tied to the Sun's magnetic structure. [112][113][114][115] This longer magnetic cycle is evident in the modulation of galactic cosmic rays, which exhibit a 22-year pattern influenced by the tilt of the heliospheric neutral current sheet and the drift of charged particles through the interplanetary magnetic field. [114] The connection between magnetic activity and irradiance is further confirmed by observations of the Ca II H and K emission lines, whose cores are heated by magnetic processes in the chromosphere. [112] These lines serve as a quantitative proxy for stellar magnetic activity, revealing that more active stars possess more vigorous cycles, implying that the younger Sun likely experienced stronger irradiance variability than it does today. [112] Together, these cycles create a complex, asymmetric environment that modulates the flow of cosmic rays and shapes the space weather experienced by Earth. The ~11 yr cycle itself was discovered by Heinrich Schwabe in 1844 through tracking the variation in the sunspot number. [43] This ~11 yr cycle is considered a fundamental feature of solar activity originating from the solar dynamo process. It is currently believed that these quasi-periodic changes in solar irradiance and sunspot number, known as the Schwabe cycle, are the result of solar differential rotation as modeled in hydromagnetic solar dynamo models. [116][117][118][119][120] Half a century later, E. W. Maunder identified the butterfly diagram, a pattern progressing from ~30° latitude to the equator over the ~11 yr period. [121] Later, G. E. Hale demonstrated that sunspots were sites of intense magnetism protruding through the Sun's photosphere and that the polarities of the butterfly's wings alternated in sign with a period of about 22 yr. [118] The variability of solar cycle amplitudes between decadal and millennial timescales can be understood in terms of a weakly nonlinear and noisy limit cycle, representing the generic model for the fundamental mode of a weakly excited $\alpha\Omega$ -dynamo. [116] No intrinsic periodicities apart from the 11-year cycle are required to understand this variability, although the possible existence of such periodicities cannot be strictly excluded. [116]

Sunspot number remains the main parameter used to track this periodicity, but the count is only the surface signature of a deeper magnetic rhythm. [122] The real physical period of the solar activity cycle is therefore not 11, but 22 years, as the sign of the toroidal magnetic field in any given cycle is opposite to that in the preceding cycle. [123] This alternation is reflected in Hale's polarity law, which notes that the leading polarity in each hemisphere changes from one sunspot cycle to the next. [122] Consequently, the 22-year Hale cycle represents the full magnetic polarity cycle, where sunspot polarities alternate in

sign each 11-year cycle. This magnetic reversal implies that the large-scale organization of the magnetic field in the interior is mostly toroidal in orientation and oppositely directed on either side of the equator, a pattern that active regions adhere to approximately 92–95% of the time. [124][118][125][126][127][128]

The solar cycle is not merely a fluctuation in spot counts but a complex magnetic phenomenon with distinct spatial and temporal signatures. [122] The butterfly diagram shows sunspot emergence progressing from approximately 30 degrees latitude to the equator over the 11-year cycle. This latitudinal migration was first mapped by E. W. Maunder. [129][118][127][125][125] Hale further established in 1908 that the polarities of these magnetic regions alternate in sign with a period of about 22 years, defining the Hale cycle. [43] This 22-year magnetic polarity cycle means that the Sun's magnetic field does not return to its original state until two 11-year sunspot cycles have passed. [43] The wings of the butterfly diagram thus represent not just the location of sunspots, but the visible manifestation of this deeper magnetic rhythm. [121] The trailing sunspot polarity flux is carried poleward by surface meridional flow, creating unipolar magnetic regions at high latitudes that rush to the poles. [127] It is now recognized that the 11 yr cycle is part of the more general Extended Solar Cycle or Hale cycle, which averages 22 yr and encompasses a variety of observational elements beyond sunspots, ranging from the latitudinal distribution of prominences to coronal X-ray bright point positions and coronal extreme-ultraviolet intensity. [130][118][131] While the dominant periodicity is about 11 yr, the Sun also undergoes longer-term variations spanning multiple cycles and lasting decades. [43]

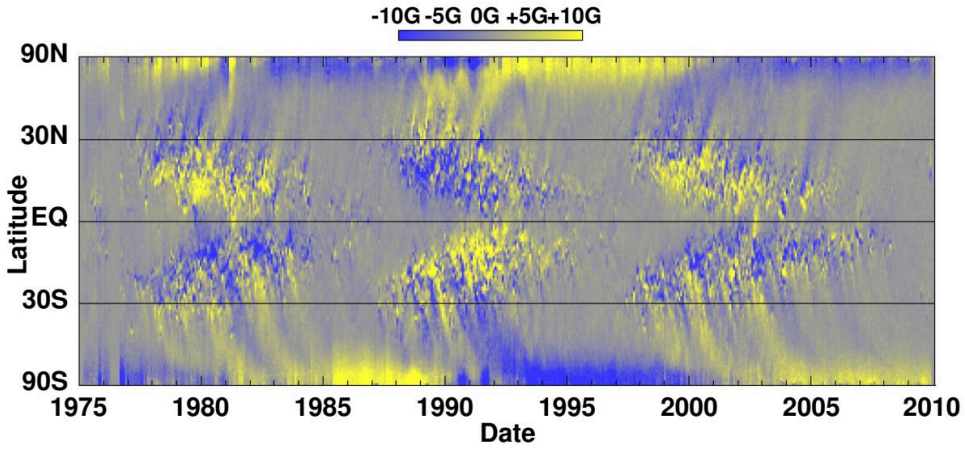

Figure 3.2: This magnetic butterfly diagram displays the longitudinally averaged radial solar magnetic field from 1975 to 2010, derived from Kitt Peak and SOHO observations. The plot shows magnetic polarity (blue for negative, yellow for positive) as a function of latitude and time, illustrating the 11-year solar cycle with alternating bands of opposite polarity emerging at mid-latitudes and migrating toward the equator, while trailing-polarity flux streams poleward to reverse the polar fields. The pattern confirms Hale's Polarity Laws, Joy's Law (tilted active regions), and the gradual reversal of polar magnetic fields, with higher-latitude magnetic features transported toward the poles over time. (source: ref 122)

The Schwabe cycle varies in both amplitude and duration, rather than being a regularly ticking clock. This variability is evident when examining the time-variant number of sunspots, which can be represented by a simple model where the solar activity period time and phase state fluctuate significantly from one cycle to the next. [19][132][133][53][134] Furthermore, the duration of the total cycle is not merely a sum of hemispheric activities but is influenced by phase asynchrony between the northern and southern hemispheres. During solar cycle 14, the total cycle length was defined by the southern hemispheric cycle, whereas in cycle 20, it was determined by the northern hemisphere, despite large phase asynchrony at the beginning of the 20th cycle. [132] In some cases, such as cycles 15 and 19, the length of the total sunspot cycle can be less than the lengths for the individual hemispheres due to fluctuations in solar activity and phase relationships around the sunspot minimum. [132] When analyzing the Wolf Sunspot Number and Group Sunspot Number datasets using Empirical Mode Decomposition, the highest amplitude intrinsic mode function corresponds to a period of approximately 9 years, followed by a mode of about 14 years, which together compose the Schwabe cycle. [133] Thus, the solar cycle is not a simple periodic oscillator but a complex system with varying amplitude and duration, shaped by hemispheric asymmetries and internal dynamical processes.

3.3 Sunspot Numbers and Their Recalibration

Sunspots are dark areas on the solar disc, characterized by strong magnetic fields that lower their temperature to about 4000 K compared to the surrounding 5800 K photosphere, making them appear as distinct darkening. [43] To repair this deficiency, Hoyt and Schatten introduced the Group Sunspot Number (G_N), which relies solely on the count of sunspot groups rather than individual spots, making the index compatible with earlier, less precise records and providing a more reliable reconstruction of solar activity back to the early seventeenth century. [58] However, methodological debates persist regarding the weighting schemes introduced by Wolf and modified by Waldmeier, which may have introduced systematic biases. Analysis of monthly values suggests that the group count and spot count are constrained to a narrow diagonal band, indicating that a one-dimensional relationship with the relative sunspot number might be sufficient for correction to an un-weighted value. [135][106][136] By calculating a weight factor using the formula $w = 1.0044 + 0.0398 \ln(R_i)$ for $R_i \geq 0.2$, researchers can divide the International Sunspot Number since 2003 by this computed factor. [135] This supports the assertion that the weight factor function is also valid for the Waldmeier era at Zürich, allowing for the correction of the Zürich sunspot number for the inflation introduced by the weighting scheme. [110] It is important to take into account that the weight factor varies with the sunspot number itself, so one cannot use a constant weight factor throughout except as a first, crude approximation. [135] This update confirms that the previous series contained artificial trends that distorted the true amplitude of solar cycles, particularly in the modern era. [58] To resolve this, the solar community undertook a decade-long effort involving four Sunspot Number Workshops from 2011–2014, producing major recalibrations: $S_N(1)$ became $S_N(2)$ by Clette and Lefèvre, and HoSc98 became SvSc16 by Svalgaard and Schatten. [137] To address these issues, researchers have replaced the sunspot number between the years 1639 and 1715 with a reconstruction by Vaquero et al., which accounts for the large amount of missing sunspot number data and the difficulty in calibrating between different observatories. [138] While the International and Group sunspot numbers share similarities, such as indicating low activity during the Dalton minimum and a peak around 1957/58, they diverge sharply for earlier periods, with Group numbers running 25-50% lower than International numbers before 1882. [139] This divergence establishes that different sunspot series agree closely over the twentieth century but diverge significantly for earlier centuries. The consensus among diverse reconstructions since 1900, where underlying data are plentiful and of good quality, confirms that all methods are equally satisfactory provided the reference observer records are stable. [109][109][139][60] However, going back in time to Solar Cycle 11, peaking in 1870, the disagreement persists for all earlier cycles, highlighting the critical need for careful calibration when interpreting long-term solar variability from the limited observational records of the past.

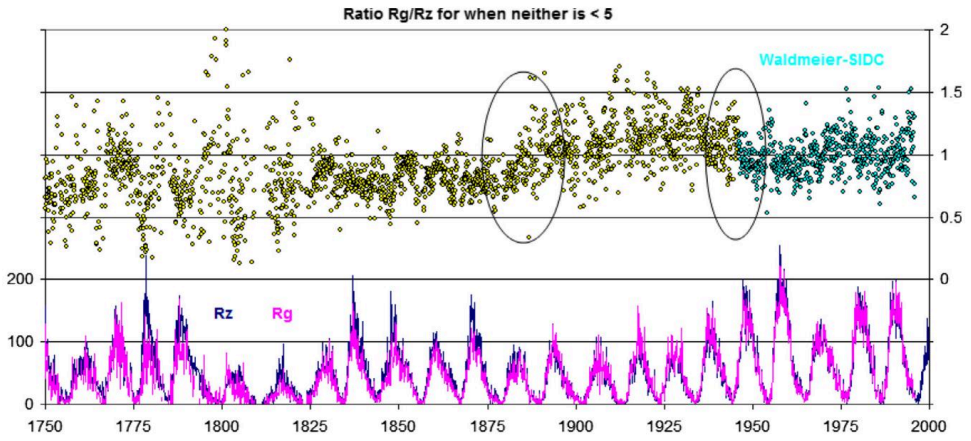

Figure 3.3: The figure displays a scatter plot of the ratio between monthly Group Sunspot Numbers (Rg) and Wolf (Zürich, International) Sunspot Numbers (Rz) from 1750 to 2000, with the ratio plotted against time. The top panel shows the Rg/Rz ratio, where data points are color-coded by time: yellow-green for earlier periods and teal for later periods, with the ratio generally clustering around 1.0 after ~1900. Two oval regions highlight periods of notable deviation. The bottom panel shows the individual Rg (magenta) and Rz (blue) time series, both exhibiting the characteristic 11-year solar cycle, with Rg values generally higher than Rz. The caption indicates the data excludes months where either Rg or Rz is less than 5. (source: ref 110)

The historical record of solar activity reveals a critical divergence in data quality as we look further back in time, particularly concerning the Maunder minimum period from 1645 to 1715. [58] Consequently, the Wolf series cannot reliably capture the true magnitude of solar cycles from 1650 to 1700, where the low fraction of active days indicates very low cycle amplitudes. In contrast, the Group Sunspot Number reconstruction, which relies on counting only the number of sunspot groups rather than individual spots, provides a more robust framework for this period. For instance, observations by Anton Maria Schyrlaeus Rheita in 1642 were initially misinterpreted as showing eight sunspot groups, but were later corrected to report one group in June, highlighting the pitfalls of early data interpretation. [29] Thus, the Maunder minimum is not merely a gap in the Wolf record but a period where the Group Sunspot Number provides the only reliable window into solar behavior, establishing a clearer picture of solar minima that extends back to the early 17th century.

For the purposes of this book we adopt the SILSO Sunspot Number version 2.0 as the reference series. The 2015 recalibration corrected the long-standing Waldmeier discontinuity and remains the community standard maintained by the World Data Center in Brussels; where later analyses dispute particular segments of the record, we flag the disagreement rather than silently switching series. [137]

3.4 The Satellite Era TSI Record

The satellite-era record of Total Solar Irradiance (TSI), the spatially and spectrally integrated radiant energy from the Sun at one astronomical unit, represents the primary energy input to the Earth's climate system, dwarfing all other sources by a factor of three thousand. [140] These measurements rely on electrical-substitution radiometers, instruments that achieve high accuracy by modulating heater power to maintain thermal stability, thereby ensuring precise quantification of the incoming solar flux. Early instruments, such as ERB and ACRIM-1, initially measured higher TSI values than subsequent sensors like ERBE, ACRIM-2, and VIRGO, creating a divergence in the long-term record that has fueled ongoing debate regarding decadal trends. [140] The launch of the Total Irradiance Monitor (TIM) onboard the Solar Radiation and Climate Experiment (SORCE) mission introduced significant improvements in measurement accuracy and stability, ultimately establishing a lower, now internationally accepted TSI value of approximately 1361 W m^{-2}. [140] Despite these advancements, the composite TSI record remains subject to scrutiny, particularly concerning the gap-bridging methods used to reconcile data from different instruments. [141] This uncertainty is critical for climate studies, as it directly impacts assessments of solar forcing on global temperatures. [141] The launch of the SOlar Radiation and Climate Experiment/ Total Irradiance Monitor (SORCE/TIM) helped resolve this offset issue. [140] It confirmed lower TSI values and indicated that predecessor instruments were approximately 0.35% erroneously high. [140] Subsequent corrections were retroactively applied to flight data for ACRIM3 and VIRGO. [140] The lower TSI value established by SORCE/TIM was validated by later missions, including the Total Spectral and Solar Irradiance Sensor (TSIS-1)/TIM, and is now the accepted value by the International Astronomical Union. [140] This recalibration improved uncertainties regarding Earth's energy balance by resolving discrepancies between incoming and outgoing radiation. [140]

The satellite-era record of total solar irradiance (TSI) reveals significant discrepancies in long-term trends depending on the composite method employed. [80] The ACRIM composite suggests TSI increased during the 1980s and 1990s but has slightly declined since then. This upward pattern from 1980 to 2000 stands in stark contrast to the PMOD composite, which indicates a slight downward trend over the same period. [93][94][93] The multi-decadal trending difference between these composites is crucial for discriminating among solar models used to interpret climate changes. [80] If TSI increased from 1980 to 2000, total solar and heliospheric activity could have increased as well, potentially contributing significantly to the global warming observed from 1980 to 2000. [80] Consequently, the choice of composite directly impacts assessments of solar forcing, with the ACRIM data supporting the possibility that TSI acted as a primary driver of global temperatures during this interval, whereas the PMOD data suggests a different mechanism for the observed warming.

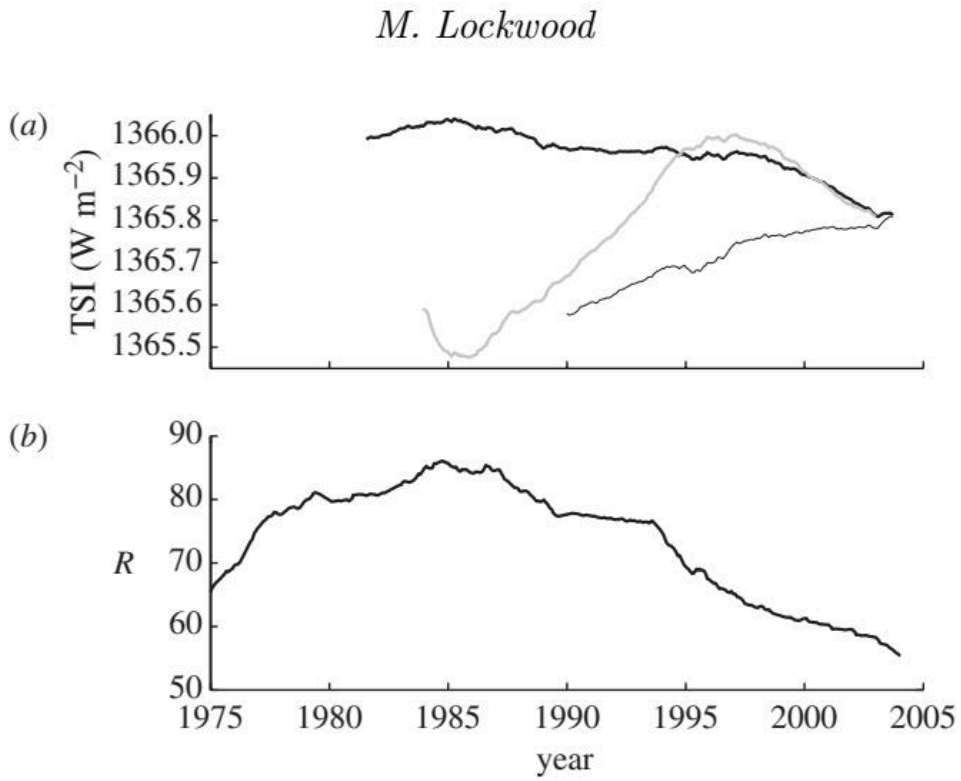

Figure 3.4: Figure 3 presents two panels showing solar-cycle-averaged variations in total solar irradiance (TSI) and sunspot number. Panel (a) plots TSI (W m^{-2}) from 1975 to 2005, comparing three composites: PMOD (thick black line), ACRIM (thick grey line, offset by −0.4 W m^{-2}), and IRMB (thin black line, offset by −1 W m^{-2}), revealing a general decline in TSI over the period with notable divergence during the late 1980s. Panel (b) shows the corresponding solar-cycle-averaged sunspot number (R), which increases from ~60 in 1975 to a peak near 85 around 1985, followed by a steady decline to ~50 by 2005. (source: ref 143)

The satellite-era record of Total Solar Irradiance (TSI) reveals significant discrepancies in how long-term trends are reconstructed, particularly concerning the period known as the ACRIM Gap. [80] During the 1990–1992.5 interval, comparisons between the WSKF06 proxy models and the PMOD composite highlight a fundamental divergence in data processing. [80] While the WSKF06 models show stationarity, the PMOD composite exhibits a significant downward trending difference, largely due to Fröhlich's downward adjustment of the ERB data. [80] This adjustment involved a shift of approximately 0.86 W/m^2, which is more than twice the shift derived from WSKF06 comparisons. [80] Consequently, the resulting PMOD composite suggests that TSI has been steadily decreasing since at least the late-1970s, a conclusion that stands in contrast to the ACRIM composite, which would require an upward adjustment of ~0.46 W/m^2 to reconcile the minima trends. This ongoing debate over gap-bridging methods underscores the uncertainty in decadal TSI trends, as the choice of composite directly influences the perceived direction of solar output over recent decades. This methodological sensitivity implies that the magnitude of solar forcing in climate models remains somewhat ambiguous. [49][94][93][93] Consequently, attributing specific temperature variations to TSI fluctuations requires careful consideration of these reconstruction uncertainties.

The divergence between the ACRIM and PMOD total solar irradiance composites stems from how the ACRIM Gap is bridged using conflicting ERB and ERBE trends. This discrepancy suggests that the resulting long-term solar trends may be somewhat ambiguous. [80]

Since 1978, direct observations of Total Solar Irradiance (TSI) have been obtained from Earth-orbiting satellites, providing a continuous time series of the integrated radiant energy arriving at the top of Earth's atmosphere. [141] However, because these instruments wear out and must be replaced, the records from each mission require inter-calibration to bridge data gaps and account for instrument degradation. Consequently, the magnitude of secular TSI change over the satellite period remains uncertain due to inconsistencies in cross-calibration. While satellite data demonstrate that TSI varies by as much as 0.05–0.07% over an 11-year solar cycle, determining any multi-decadal trend beyond this cycle is difficult.

[60][142][60][140][93][94] These variations illustrate the difficulties faced when combining experiments, suggesting that it is currently not possible to be confident of any multi-decadal trend in TSI. [141]

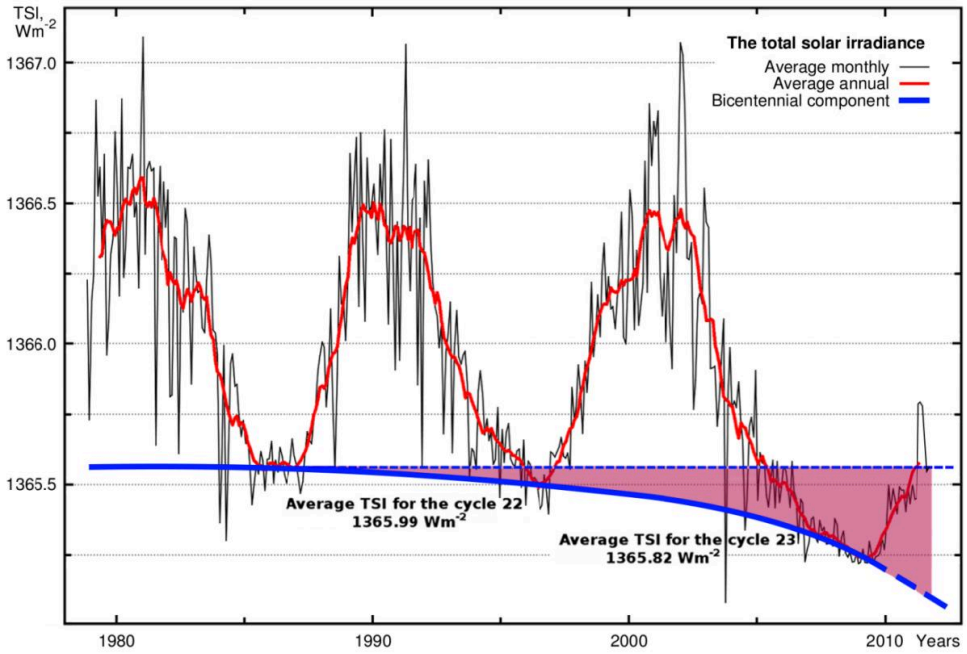

Figure 3.5: The graph displays the total solar irradiance (TSI) from 1978 to 2011, showing daily (black line) and average monthly (red line) variations, with a long-term trend (blue line) representing the bicentennial component. The data reveals a clear 11-year solar cycle, with TSI peaking around 1366.5 W/m² and declining to a minimum near 1365.5 W/m². The average TSI for solar cycle 22 is 1365.99 W/m², while for cycle 23 it is 1365.82 W/m², indicating a gradual decrease in solar output over the period. (source: ref 144)

The satellite era, which began in late 1978, provides the only direct observations of Total Solar Irradiance (TSI), the integrated radiant energy arriving from the Sun at the top of Earth's atmosphere. [80] However, due to data gaps and instrument degradation, the precise calibration needed to bridge these records is not universally agreed upon, leading to divergent composites. For instance, early instruments like ERB and ACRIM-1 measured higher TSI values than subsequent instruments, a discrepancy that was partially resolved following the SORCE/TIM launch and international calibration workshops, which established a lower accepted TSI value of approximately 1361 W m^{-2}. [140] Satellite data demonstrate that TSI varies by as much as 0.05–0.07% over an 11-year solar cycle, amounting to around 1 W/m² at the top of the atmosphere and only 0.2 W/m² at the surface after accounting for geometry and albedo. [141] The critical question for climate science is whether there is a trend in the TSI data beyond this 11-year cycle, as this could have implications for estimates of TSI changes on long timescales. [141] Consequently, the debate over whether TSI has increased or decreased over the multi-decadal scale remains unresolved, with reconstructions from different groups disagreeing on the magnitude and direction of any potential trend.

3.5 F10.7 and the Modern Activity Index

The F10.7 index has been recorded continuously since February 1947, creating a consistent dataset that allows researchers to track solar cycles with high precision. [43]

The Sun's radio flux density at the 10.7 cm wavelength serves as a critical metric for solar activity, distinct from visible sunspot counts. [122]

The 10.7 cm Solar Flux, measured daily by the Canadian Solar Radio Monitoring Programme since 1946, offers a completely objective record of solar activity that can be taken under virtually all weather conditions. [122] While this radio flux is highly correlated with the International Sunspot Number, the relationship between the two indices is slightly nonlinear, with the slope changing as the sunspot number increases up to about 30. This complexity is captured by the Holland and Vaughn formula, which accounts for the base level of about 67 solar flux units and the varying sensitivity at different activity levels. [137]

[122][122][145][139] Although the two measures are tightly linked, the 10.7 cm radio flux lags behind the sunspot number by about one month, adding a temporal nuance to the correlation. [122]

The 10.7 cm Solar Flux, measured daily by the Canadian Solar Radio Monitoring Programme since 1946, offers a completely objective measure of solar activity that can be recorded under virtually all weather conditions. [122] Unlike sunspot counts, which rely on visual observation, this radio flux captures disc-integrated emission at 2800 MHz, providing a stable baseline of about 67 solar flux units for a quiet Sun. [122] The relationship between this radio index and the International Sunspot Number is remarkably tight; statistical analysis confirms that the two measures are highly correlated, with a correlation coefficient of r = 0.995. This near-perfect linear alignment demonstrates that F10.7 serves as a robust proxy for overall solar variability, tracking the rise and fall of solar cycles with precision. [146][137][122][147][148][149]

4. The Grand Solar Cycles: Zharkova's Two-Wave Dynamo

Zharkova's PCA of synoptic magnetograms reveals two magnetic waves whose beating predicts a Modern Grand Solar Minimum running ~2020–2053.

4.1 The Solar Background Magnetic Field

In contrast, the background field is measured across the full disk using synoptic magnetograms from observatories like the Wilcox Solar Observatory. Recent analyses have applied Principal Component Analysis (PCA) to these low-resolution full-disk solar background magnetic field measurements to derive the dominant eigenvalues that cover the maximum variance of the data. [150] This method identifies eigenvectors, or Principal Components (PCs), which come in pairs and reflect the main dipole dynamo waves produced by the solar dynamo mechanism. [151] By classifying these PCs using symbolic regression based on the Hamiltonian principle, researchers have derived mathematical formulae describing their amplitude and phase variations. [150] The summary curve of these two PCs, derived for cycles 21–23 and predicted for cycles 24–26, shows a noticeable decrease in predicted average sunspot numbers, linked to a reduction in the amplitudes and an increase in the phases of the principal components of the solar background magnetic field. [152] Furthermore, extending this prediction thousands of years backward and forward reveals the occurrence of a grand solar cycle of 350–400 years, successfully reproducing well-known historical events such as the Maunder, Wolf, Oort, and Homeric Grand Solar Minima.

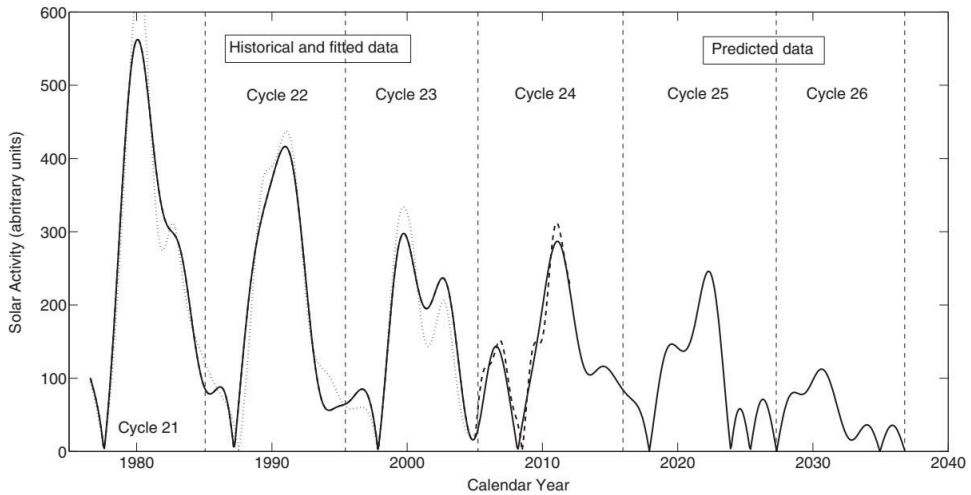

Figure 4.1: This line graph plots solar activity (in arbitrary units) against calendar year from 1970 to 2040, showing the modulus summary principal component for solar cycles 21–26. The solid curve represents the calculated modulus summary PC for cycles 21–23 and its prediction for cycles 24–26, while the dotted curve shows the derived PC from SBMF for cycles 21–23, and the dashed curve shows the SBMF-derived PC for cycle 24. The graph is divided into historical and fitted data (cycles 21–23) and predicted data (cycles 24–26), with vertical dashed lines marking the start of each solar cycle. (source: ref 152)

To isolate the large-scale solar background field from the chaotic noise of active regions, researchers rely on low-resolution magnetograms from the WSO Babcock solar magnetograph. [153] The Stanford University telescope, equipped with a 22.9m vertical Littrow spectrograph, has provided daily sun-as-a-star integrated light measurements of the mean solar magnetic field since May 1975. [154] The polarity pattern observed in these mean field measurements is essentially identical to the interplanetary magnetic field sector structure seen near Earth, albeit with a four-day lag. [154] These principal components,

which come in pairs, are considered a reflection of the main dipole dynamo waves in the solar poloidal magnetic field produced by the dynamo mechanism. [150] By applying symbolic regression based on the Hamiltonian principle, scientists derived mathematical formulae describing the amplitude and phase variations of these eigenvectors. [150]

To isolate the solar background magnetic field from the noise of active regions, researchers applied principal component analysis to low-resolution full-disk synoptic magnetic maps measured by the Wilcox Solar Observatory. [155] This statistical technique decomposes the temporal variations of latitudinal magnetic waves into eigenvectors, each assigned to a separate process supported by its derived variance. [11] The analysis reveals that the eigenvalues and corresponding eigenvectors come in distinct pairs, with the first two eigenvalues covering 39% of the observed magnetic data variance and the next two covering 18%. [11] Collectively, these four pairs account for about 95% of the total magnetic data variance, suggesting that the solar background field is dominated by a small number of coherent modes rather than random fluctuations. These principal components, identified as the largest eigenvectors, represent the primary symmetric structures in the latitudinal distribution of the field. [11][120][156][157][158] This mathematical approach treats the magnetic field as potential between the photosphere and a source surface, where the field is presumed to be exactly radial. [158] The harmonic coefficients are generated based on summary year-long synoptic maps for every rotation, with a cadence equal to half a Carrington rotation. [159] The decomposition relies on the assumption that the magnetic field is potential between the photosphere and the source surface, while the field is presumed to be exactly radial at the source surface. [124] This technique allows for the precise extraction of the large-scale magnetic structure from the complex synoptic data. [121] The use of associated Legendre polynomials demonstrates that the solar surface magnetic field can be effectively broken down into its constituent harmonic parts. [124] The harmonic coefficients are derived from the synoptic maps, ensuring that the analysis is grounded in observational data. [159] These models rely on line-of-sight measurements of the photospheric magnetic field, which are mapped up to a hypothetical coronal source surface where the field is assumed to be purely radial. [158] This approach assumes that there are no currents in the corona between the photosphere and the source surface, meaning the curl of the magnetic field is zero. [158] By solving Laplace's equation, the coronal field lines are determined, allowing for the classification of open flux that extends from the photosphere to the source surface. [158] However, the accuracy of these models is affected by several factors, including the assumption of time-invariance of the photospheric boundary and the challenge of resolving polar magnetic fields due to line-of-sight projection.

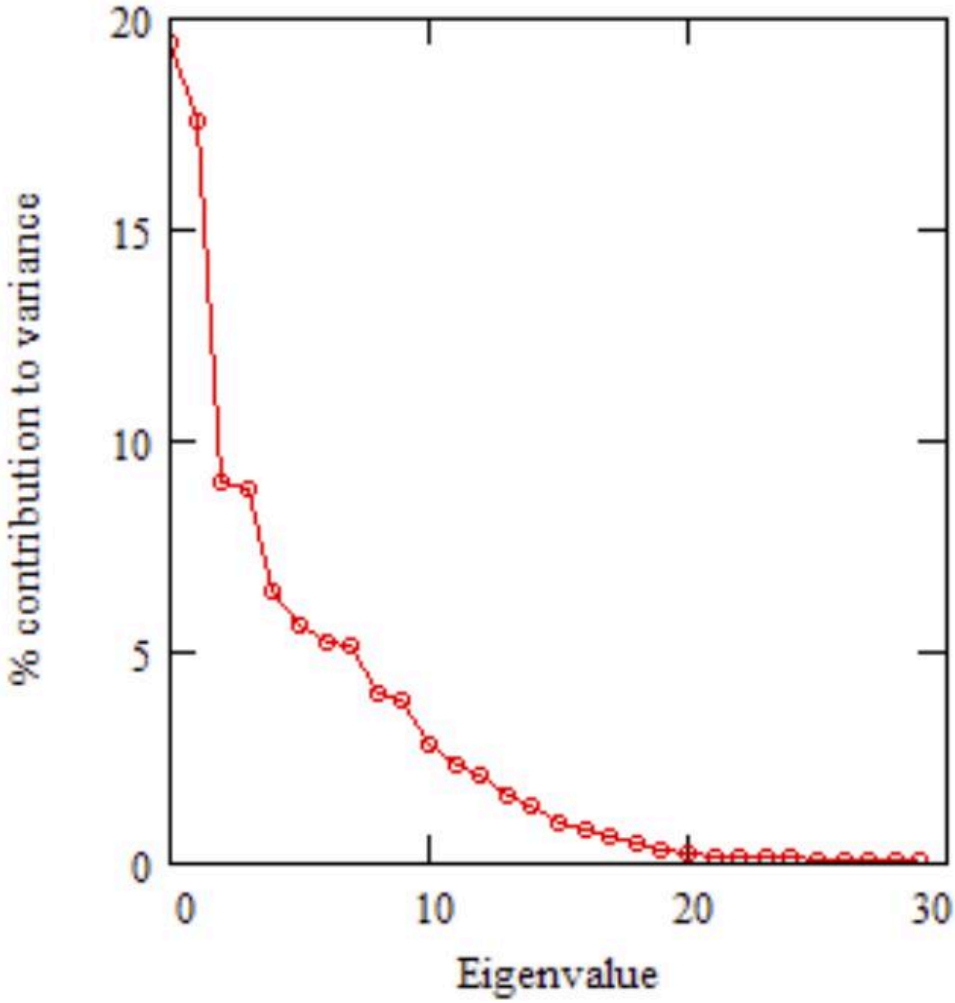

Figure 4.2: This scree plot displays the percentage contribution to variance (y-axis) against eigenvalue number (x-axis) from a principal component analysis of the solar background magnetic field (SBMF) across solar cycles 21–24, using data from the Wilcox Solar Observatory. The curve shows a steep decline in variance contribution for the first few eigenvalues, followed by a long tail of diminishing contributions, indicating that a small number of principal components capture most of the variability in the SBMF data. The pattern is consistent with that previously reported for cycles 21–23. (source: ref 155)

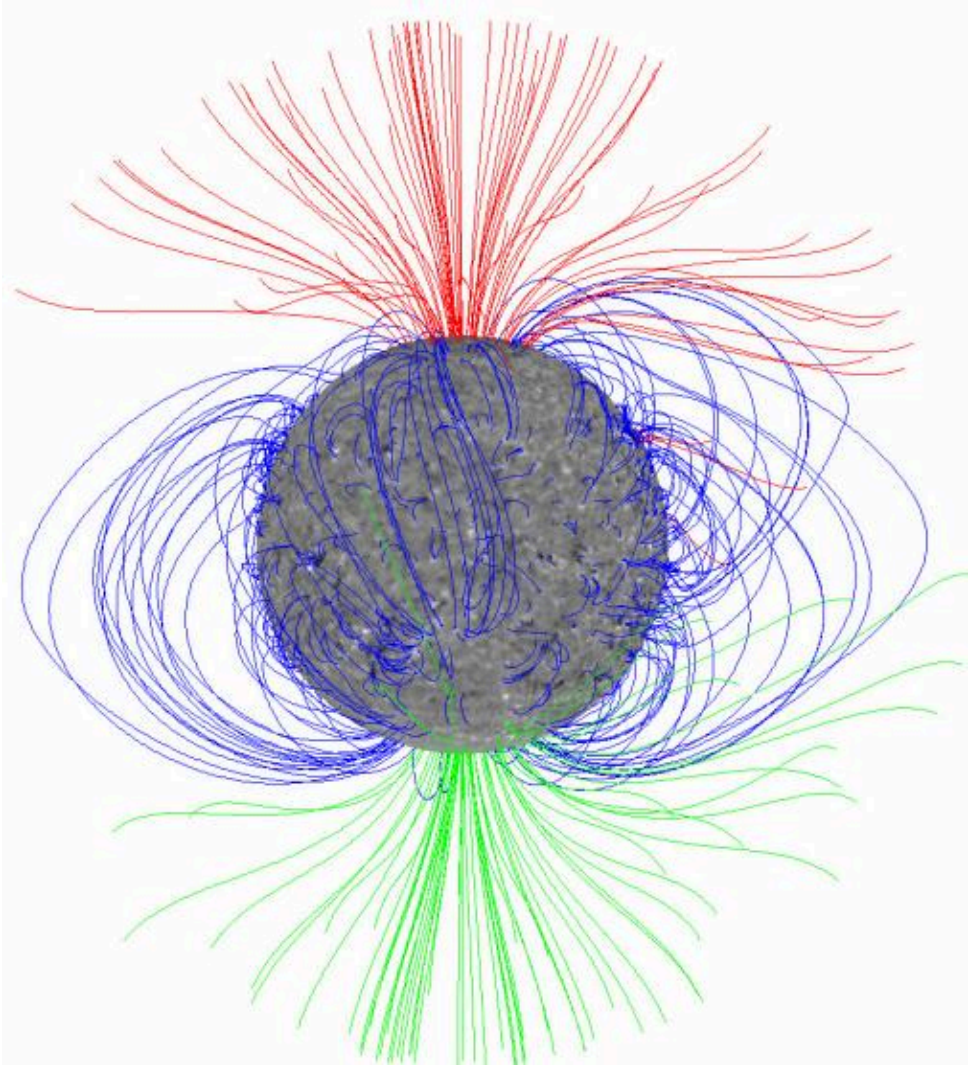

Figure 4.3: This figure displays a Potential Field Source Surface (PFSS) model of the Sun's magnetic field, showing the radial photospheric field strength via grayscale (saturated at 100 G, white for positive, black for negative polarity) and magnetic field lines. Open field lines are color-coded: green for positive polarity, red for negative polarity, and blue for closed field lines. The model illustrates a solar minimum configuration, where the dipole axis is aligned with the rotation axis, resulting in a nearly symmetric distribution of open flux with visible green (positive) and red (negative) field lines extending from opposite poles. The closed field lines (blue) form loops concentrated near the equator, indicating active regions. This configuration contrasts with solar maximum, where the dipole axis is tilted and open flux is asymmetric. (source: ref 127)

4.2 PCA and the Two Wave Decomposition

To distill the main parameters of the waves present in observational solar magnetic data, researchers applied Principal Component Analysis (PCA) to low-resolution full disk solar background magnetic field measurements. [150] This orthogonal linear transformation reduces multi-dimensional data to lower dimensions for analysis, ensuring that the greatest variance by any projection of the data lies on the first coordinate, known as the Principal Component (PC), with the second PC orthogonal to the first defined by the second largest variance. [150] The technique simultaneously reduces data dimensionality, increases signal-to-noise ratios, and orthogonalizes the resulting components so they can be ascribed to separate physical processes. [150] PCA was applied to the poloidal magnetic field data measured by the Wilcox Solar Observatory, which became available from cycle 21 to cycle 24 with an accuracy better than 0.5 Gauss. [150] By calculating the covariance matrix of the magnetic field data and its variance as the eigenvalues of magnetic oscillations, the analysis derived the eigenvalues of the Sun's own magnetic

oscillations. [151] The sets of eigenvalues and eigenvectors were derived from the observed magnetic synoptic maps and sorted by the variance of the data contributing to each eigenvector. [11] This process revealed that the eigenvalues and corresponding eigenvectors come in pairs, with the first two eigenvalues covering 39% of the observed magnetic data variance, the next two covering 18%, and all four pairs covering about 95% of the magnetic data variance. [11] The first pair of two largest eigenvalues, with the maximum variances of the data corresponding to the two largest eigenvectors, were considered to be the Principal Components. [150] These PCs are considered the main dipole dynamo waves of the solar poloidal magnetic field. [150] The PCA method uses the covariance matrix of the magnetic field data and its variance as the eigenvalues of magnetic oscillations, defining the magnetic wave properties as shown in the Scree plot. [151] Using PCA, researchers managed to derive the eigenvalues of the Sun's own magnetic oscillations, showing clearly at least four noticeable pairs with large eigenvalues covering 96% of the total data variance. [151] The first two highest eigenvalues were used to build eigenvectors for the two principal components, or coherent magnetic waves, corresponding to these eigenvalues. [150] This is equivalent to deriving different wavelengths of white light after it is split in a prism. [141] Now these two magnetic waves can be assigned to unique physical processes. [151] By applying Parker's model for two layers with meridional circulation, researchers derived that these PC waves correspond very closely to the waves generated by dipole magnetic sources. [150] Principal Component Analysis (PCA) of synoptic magnetic maps from cycles 21–24 yields eigenvectors that cover the majority of magnetic data variance. The leading eigenvectors are thus interpreted as coherent dipole dynamo waves, suggesting that the solar poloidal field is dominated by a small number of distinct physical modes. [11][150][151][155][153]

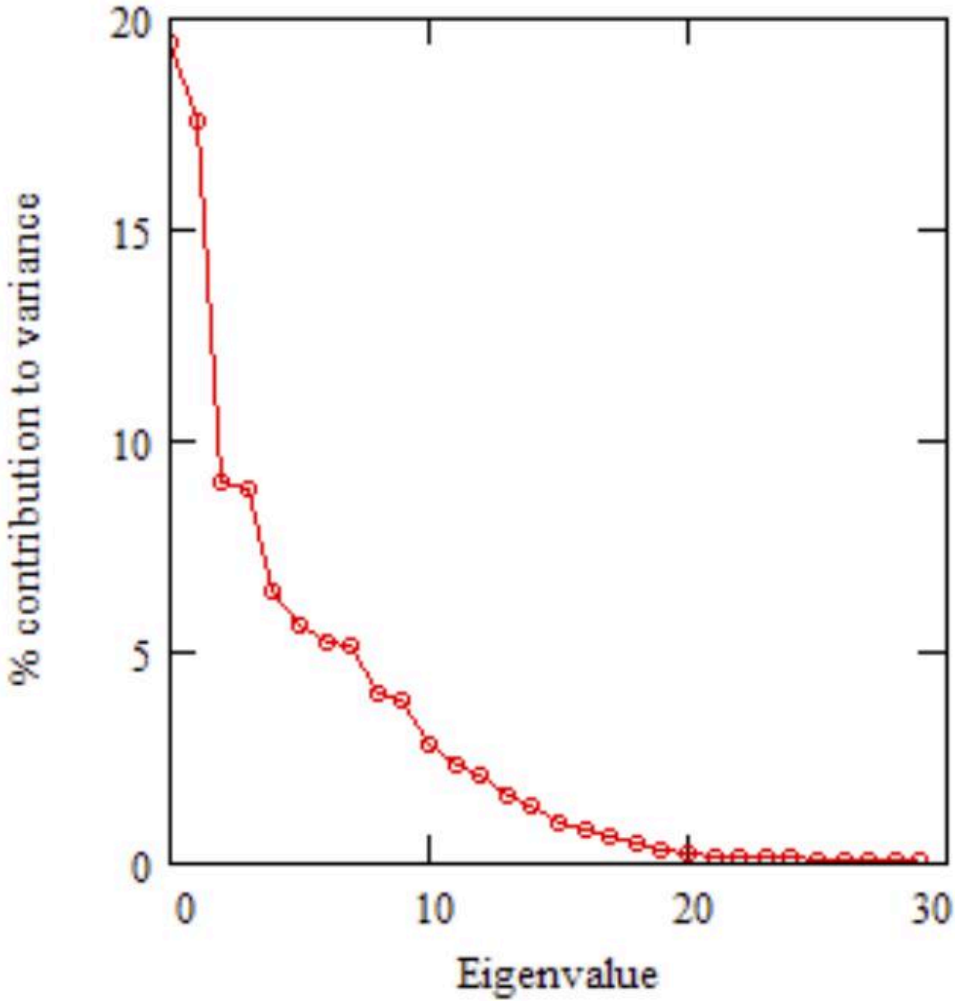

Figure 4.4: This scree plot displays the percentage contribution to variance (y-axis) against eigenvalue number (x-axis) from a principal component analysis of the solar background magnetic field (SBMF) across solar cycles 21–24, using data from the Wilcox Solar Observatory. The curve shows a steep decline in variance contribution for the first few eigenvalues, followed by a long tail of diminishing contributions, indicating that a small number of principal components capture most of the variability in the SBMF data. The pattern is consistent with that previously reported for cycles 21–23. (source: ref 155)

Principal Component Analysis of the low-resolution full disk solar background magnetic field, measured by the Wilcox Solar Observatory from synoptic full disk magnetic maps, isolates the dominant eigenvalues covering the maximum variance of the data. [150] The first pair of two largest eigenvalues, corresponding to the two largest eigenvectors, accounts for 39% of the observed magnetic data variance, while all four pairs cover about 95%. [160] Extrapolating these principal components backward reveals two 350-year grand cycles superimposed on the 22-year cycles, reproducing historical features such as the Maunder and Dalton minima. [150] This approach confirms that the interaction of dynamo waves with close frequencies leads to beating effects responsible for grand cycles, providing a confident prediction of solar activity on a millennium timescale. [150] These two principal components, covering about 39% of the variance of the whole magnetic field data, are found originating in opposite hemispheres and travelling with an increasing phase shift, defining the active hemisphere for odd and even cycles. [150] This stability reassures the health of the dynamo machine, while variations in wave frequencies cause a beating effect that produces grand cycles and grand minima occurring every 350–400 years. [161]

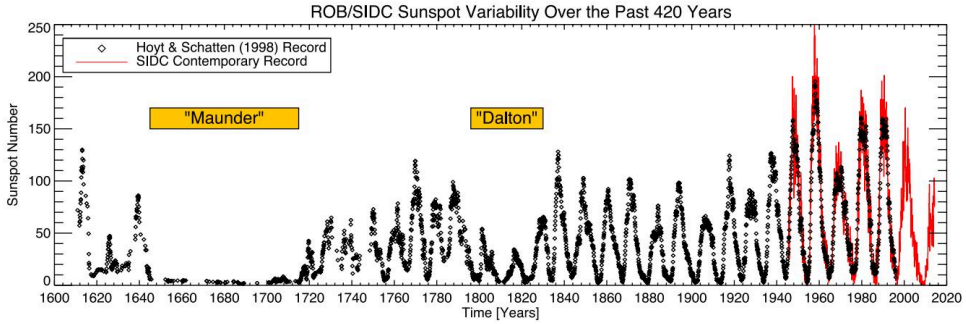

Figure 4.5: This line plot displays the total sunspot number from 1600 to 2020, showing solar activity over the past 420 years. The data, sourced from WDC-SILSO, reveals a dominant ~11-year cycle and two extended periods of low activity labeled "Maunder" (1645–1715) and "Dalton" (1790–1830), representing grand minima. The plot compares the Huyt & Schatten historical record (black dots) with the SIDC contemporary record (red line), highlighting the long-term variability of solar output. (source: ref 164)

Principal Component Analysis applied to low-resolution full disk solar background magnetic field data from the Wilcox Solar Observatory reveals that eigenvalues and corresponding eigenvectors emerge in pairs, with the first two accounting for 39% of the observed magnetic data variance and the first four pairs covering approximately 95%. [11] However, converting the resulting eigenvector summary curve into a modulus summary curve is necessary to detect the 11-year solar cycle, as the raw eigenvector data alone does not clearly resolve this periodicity without such transformation. This mathematical step ensures that the oscillatory nature of the magnetic waves is properly captured, allowing the superposition of these principal components to reconstruct the historical sunspot envelope and predict future solar activity minima. [124][11][156][150][161]

Principal Component Analysis of the low-resolution full-disk solar background magnetic field, measured by the Wilcox Solar Observatory, isolates dominant eigenvalues that correspond to eigenvectors reflecting the main dipole dynamo waves in the solar poloidal magnetic field. [150]

The decomposition of solar magnetic data reveals that the Sun's activity is not driven by a single oscillator, but rather by the superposition of multiple waves generated by distinct magnetic sources within the solar interior. [162] Theoretical evaluations indicate that the quadruple magnetic wave, originating in the inner layer at the bottom of the Solar Convective Zone, accounts for the occurrence of centennial oscillations in the summary curve of solar activity. [163] This mechanism supports the restoration of historical features such as the Dalton minimum at the beginning of the nineteenth century and another Gleissberg minimum at the start of the twentieth century, which were not fully captured by dipole-only models. [163] The beating effect between the dipole and quadruple waves naturally produces an envelope wave with a period of approximately 100 years, aligning with the observed centennial cycle. [151]

4.3 Isotope Validation

Studies such as those by Delaygue and Bard have examined Beryllium-10 records from Central Antarctica, specifically from the South Pole and Dome Fuji stations, covering the last millennium to quantify the relationship between ice-core deposition and production rates. [63] In contrast, ^{10}Be offers a more direct proxy; as an aerosol-borne isotope, it is removed from the atmosphere relatively fast within a few years and stored in natural archives such as polar ice sheets. Because of its short atmospheric residence time, ^{10}Be directly reflects cosmic ray intensity variations with almost no attenuation and a delay of only 1–2 years. [52]

The global carbon cycle imposes significant constraints on the resolution of solar activity records derived from radiocarbon. [165] Furthermore, the carbon cycle delays the response of atmospheric ^{14}C concentration relative to production variations, creating a phase lag that ranges between 0 and 90°, with larger lags occurring for shorter periods. For centennial variations, this phase lag is approximately 45°, meaning atmospheric ^{14}C concentration lags production by roughly 12 years. [63] This specific lag aligns with the delay estimated by Bard et al. between the South Pole ^{10}Be record and the IntCal04 ^{14}C record. [63] While 12-box models predict larger phase lags due to stratospheric transfer times, adequate observations remain lacking to fully validate these predictions. [63] Consequently, the uncertainty in reconstructed ^{14}C

due to carbon inventory remains a critical factor, with different box models showing varying attenuations and time lags that complicate the direct interpretation of high-frequency solar signals in tree-ring data.

Ice-core records of beryllium-10 (^{10}Be) provide a critical proxy for solar activity, as this isotope is produced by high-energy galactic cosmic-ray interactions with atmospheric oxygen and nitrogen. [166] Because the solar wind's magnetic field deflects these cosmic rays, ^{10}Be production rates are anti-correlated with solar activity, meaning higher sunspot numbers correspond to lower ^{10}Be concentrations in polar ice. [166] To validate solar modulation models during the Maunder Minimum (1645–1715), researchers compared model results with ^{10}Be observations from two independent ice cores, Dye3 and NGRIP, which are separated by more than 1000 km. [167] The NGRIP dataset, in particular, shows an inverted phase relation during the Maunder Minimum that was not employed in earlier studies, suggesting that the ^{10}Be cycling observed during this grand minimum was indeed a solar modulation effect rather than a terrestrial artifact. This consistency between spatially separated ice-core proxies and sunspot reconstructions supports the reliability of using cosmogenic isotopes to hindcast solar variability and validate dynamo models. [167][166][168] For instance, simulated $\Delta^{14}C$ levels have been found to deviate from IntCal04 data by several percent during specific centuries, often driven by anomalies in the South Pole or Dome Fuji ^{10}Be records. [63]

Cosmogenic isotopes such as beryllium-10 and carbon-14 serve as proxies for past cosmic-ray flux, offering a record that extends far beyond the era of neutron monitors. [139] Consequently, extracting the solar component from the ^{14}C record becomes significantly more difficult for the modern period, as the anthropogenic trend competes with and often overwhelms the subtle variations driven by solar activity. Thus, the isotope validation section concludes that the two-wave model's robustness is best confirmed in the pre-industrial record, where anthropogenic noise is absent, while the modern era requires careful deconvolution of fossil-fuel-induced isotopic shifts to assess the model's accuracy.

4.4 The 2020 2053 Modern Grand Solar Minimum Prediction

Analysis of this double-dynamo system establishes that the Sun entered a modern Grand Solar Minimum in 2020, a period of reduced solar activity expected to last until 2053. This prediction is supported by multiple independent methodologies; for instance, Velasco Herrera et al. applied a Bayesian algorithm to averaged sunspot numbers and obtained similar results, reporting the modern Grand Solar Minimum to occur in cycles 25-27. [156][169][170] Furthermore, these prediction results were confirmed by other researchers, including Kitiashvili and Obridko et al., who utilized the same WSO synoptic magnetic field data to obtain spectra of the zonal harmonics of the solar background magnetic field approaching the Grand Solar Minimum, interpreting them with 3D solar dynamo models. The current quiet Sun is caused by a significantly reduced magnetic field generated by the interference of double dynamo magnetic waves, which means that during this Grand Solar Minimum, solar irradiance will be reduced by about 3 W/m², or 0.22%. [169] This reduction in solar irradiance caused by the Grand Solar Minimum effect works in opposition to the increase of solar irradiance caused by orbital solar inertial motion effects, creating a complex interplay of forcing mechanisms that define the thermal baseline for the coming decades. [169]

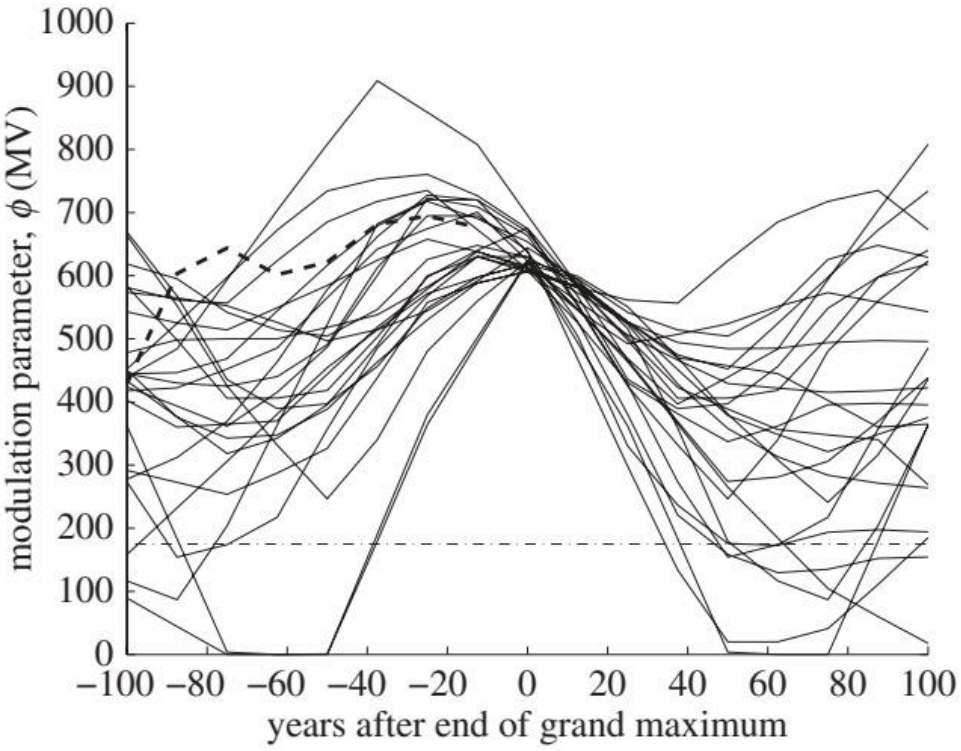

Figure 4.6: The chart displays a superposed epoch analysis of the heliospheric modulation parameter φ (in MV) over 9000 years, with 24 individual case trajectories aligned at t = 0—the point when φ drops below 600 MV, marking the end of a grand solar maximum. Each line represents a separate historical event, showing a general decline in φ following the peak, with the thick dashed line highlighting the recent 100-year trend. A horizontal dot-dashed line at 175 MV indicates a reference level from prior analysis, and the convergence of trajectories around t = 0 reveals a consistent pattern in the post-maximum decay of solar modulation. (source: ref 177)

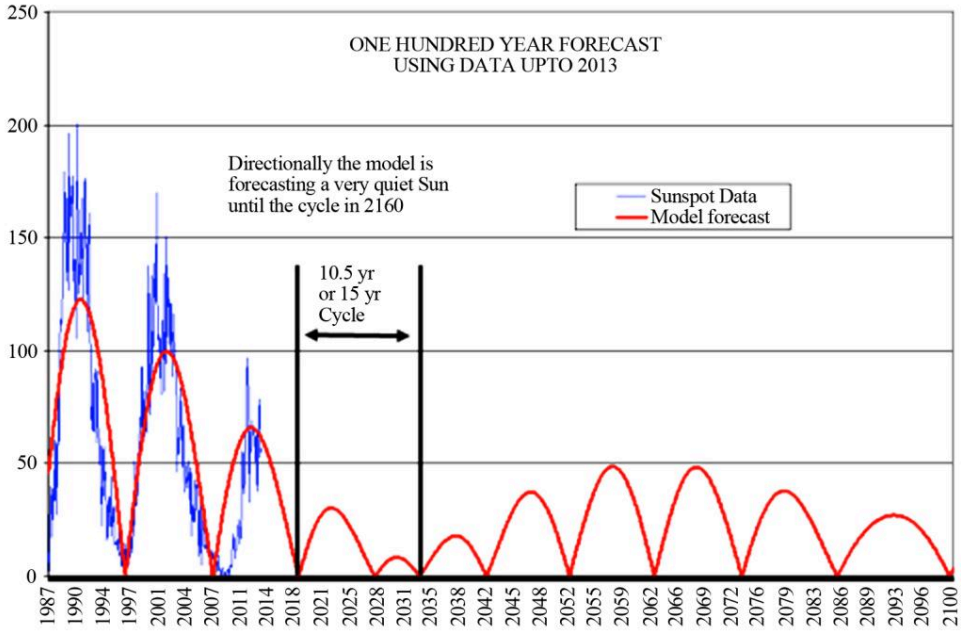

Figure 4.7: The figure displays a time-series plot comparing monthly sunspot numbers from 1987 to 2013 (blue line) against a model forecast of the absolute value of solar activity (red line) extending to 2100. The x-axis spans years from 1987 to 2100, with the y-axis representing sunspot numbers up to 250. The model forecast, derived using data up to 2013, predicts a prolonged period of low solar activity, indicating a very quiet Sun until a cycle in 2160, with a cycle duration of 10.5, 15, or 15 years. (source: ref 176)

Statistical analysis of past grand maxima suggests a 1-in-12 probability of a Maunder-like grand minimum occurring within 50 years. This estimate derives from a superposed epoch analysis of the modulation parameter at the end of the previous grand solar maxima in the last 9300 years, based on the composite reconstruction of the modulation parameter from Steinhilber et al.. [171][170][156][147][172] Furthermore, Owens et al. created a data set for solar wind parameters dating back to 1617 to investigate Maunder minimum conditions and find the most probable coronal magnetic field configuration for this period. This configuration could be used for any past or future grand minima. [171]

Predicting the amplitude of solar cycles remains highly uncertain, with models for Cycle 24 showing wide disagreement. This uncertainty stems from the fact that cycle prediction is a fairly model-dependent affair, as evidenced by contradictory forecasts for Solar Cycle 24. [173][174][175][170] While Dikpati et al. predicted it would be the strongest cycle in fifty years, Choudhuri et al. concluded it would be the weakest in a century. [174] These divergent outcomes highlight that there are still many uncertainties in solar dynamo models, making it worthwhile to analyze the physical basis of solar cycle prediction carefully rather than having too much faith in predictions from any particular model. [123] The community-wide panels convened to construct consensus opinions on upcoming cycles often receive a broad range of submissions that cover almost all potential physically reasonable outcomes. [175] Consequently, the strength of every solar cycle a few years before its onset cannot be determined with precision, demonstrating the inherent difficulty in forecasting solar activity. Consequently, the modest irradiance decline predicted for the upcoming Modern Grand Solar Minimum implies a limited direct radiative cooling effect, consistent with the model results assuming small TSI variation.

The thermal implications of the predicted solar dimming are quantified through simple energy-balance calculations that relate changes in Total Solar Irradiance (TSI) to Earth's effective temperature. [144] Taken at face value, the predicted ~3 W/m² (0.22%) drop in TSI works out — once spread over the spinning globe and corrected for reflection — to a direct radiative cooling of only one or two tenths of a degree: real, but modest. That is precisely why this book's argument does not rest on irradiance arithmetic alone. The chapters that follow lay out the amplifiers — the cosmic-ray cloud seeding of Chapter 6, the volcanic coupling of Chapter 7 — that turn a two-tenths-of-a-degree nudge into Little Ice Age winters. Wherever this book quotes a larger cooling, it is a claim about that amplified response, not about the bare radiative term.

The solar activity became systematically decreasing from cycle 21, coinciding with a decrease of the solar background magnetic field in the approach of the grand solar minimum (GSM) (Zharkova et al. [170]

2015; Zharkova & Shepherd 2022). These prediction results about the modern GSM in cycles 25-27 were confirmed by some other researchers (Kitiashvili 2020; Obridko et al. [170] This long-term perspective, which incorporates both the historical sunspot number record covering the last 400 years and paleoreconstructions extending throughout the Holocene, provides critical observational constraints for dynamo models. [111]

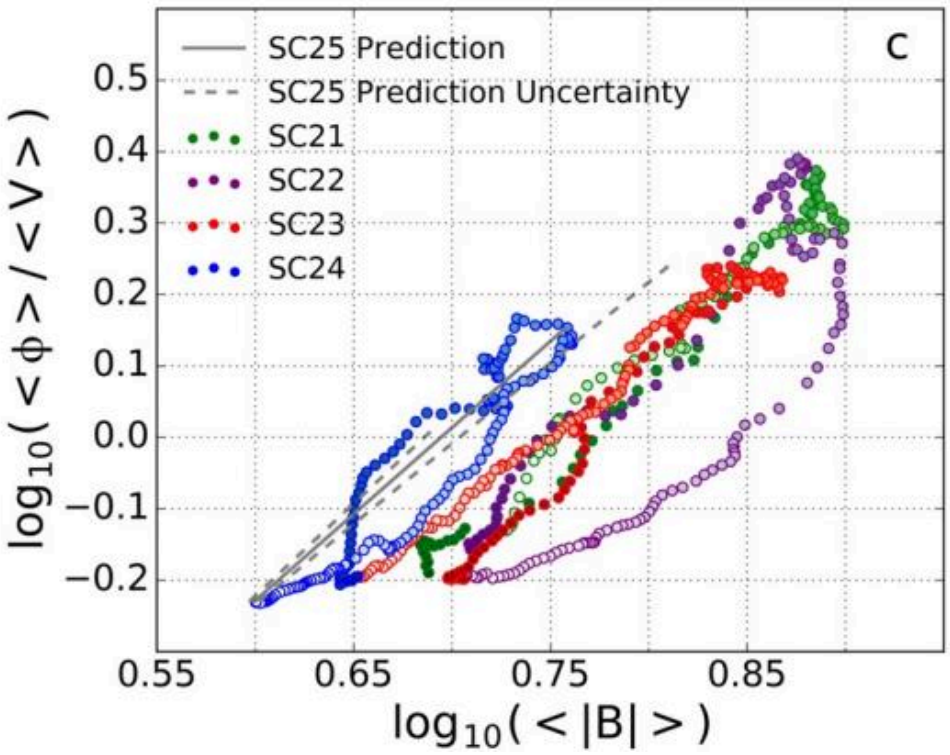

Figure 4.8: >) on the x-axis and $\log_{10}(\langle\Phi\rangle/\langle\bar{V}\rangle)$ on the y-axis, showing data for solar cycles SC21 through SC24 and a prediction for SC25. The data points for each cycle are color-coded, with SC25 represented by a gray solid line and its uncertainty by a gray dashed line, based on a predicted maximum magnetic field strength of B_Max = 5.74 ± 0.80. The plot illustrates a transition toward a potential modern secular minimum, with SC24 and the SC25 prediction aligning with lower activity levels. (source: ref 171)

4.5 Flare Physics the Same Magnetic Field

To understand the magnetic architecture that drives long-term solar variability, one must first anchor the analysis in the established physics of the solar dynamo, the engine that generates the 11-year Schwabe cycle. [43] The classical Parker model, proposed in 1955, demonstrates that this cycle arises from a self-exciting loop of magnetic field generation. [120] Furthermore, large-scale circulation patterns, such as the azimuthal rolls discovered by Ribes and Mein in 1984, modulate surface rotation and appear to regulate the internal shear that drives the dynamo.

The Babcock–Leighton type dynamo models demonstrate that meridional circulation regulates the solar cycle period by transporting magnetic flux from the surface to the tachocline. This advective process is central to the flux transport dynamo framework, where the poloidal field generated by tilted bipolar regions is carried poleward and then downward to the tachocline. [174][178] The time scale of this circulation sets the dynamo period, establishing a direct link between flow speed and cycle length. [134] Models suggest that stochastic fluctuations in the alpha-effect cannot trigger grand minima, whereas a strong decrease in meridional circulation can. [178] Thus, the variability of this transport mechanism provides the physical basis for the irregularities seen in the solar record, connecting the large-scale dynamo operation to the potential for Maunder-like grand minima. [178]

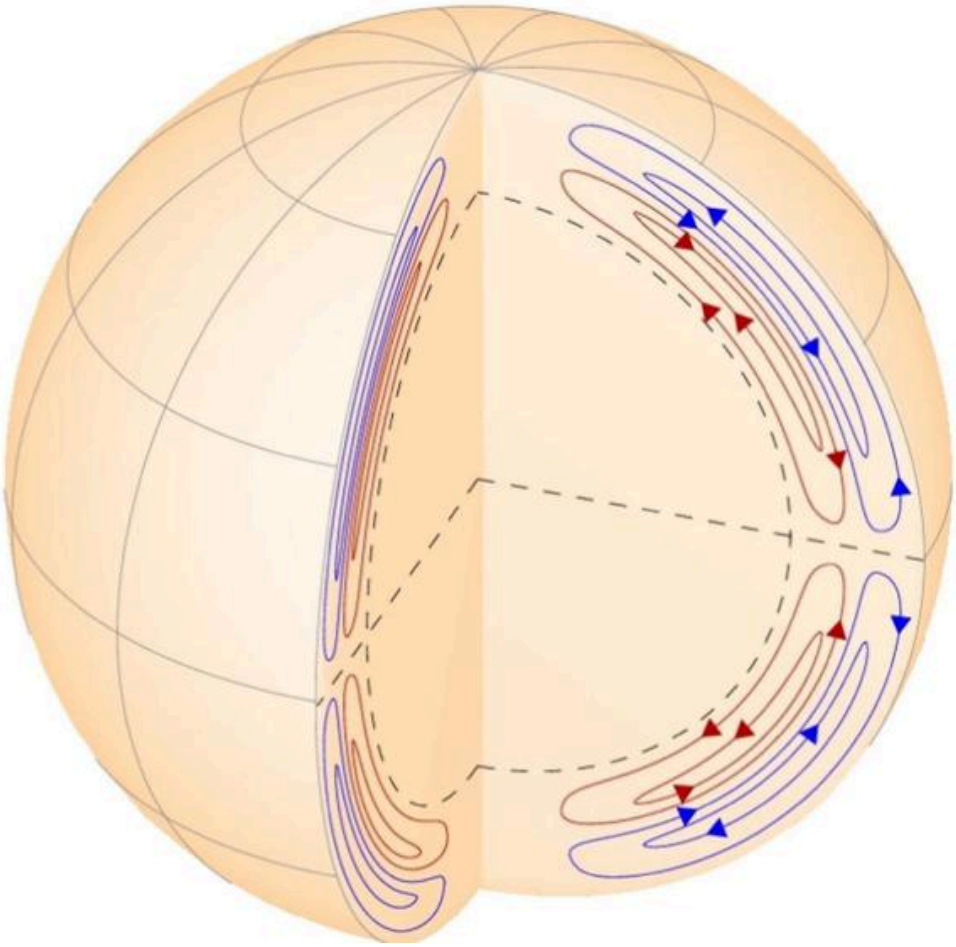

Figure 4.9: This figure illustrates a schematic model of the solar dynamo, depicting two opposing meridional circulation cells within the Sun's interior. The model, derived from HMI/SDO observations, shows flow patterns represented by blue and red arrows indicating upward and downward motions, respectively, along with nested streamlines illustrating the circulation. The opposing flows in the northern and southern hemispheres suggest a mechanism for generating the solar magnetic cycle, with the dashed lines indicating the solar equator and the grid representing latitude and longitude. (source: ref 150)

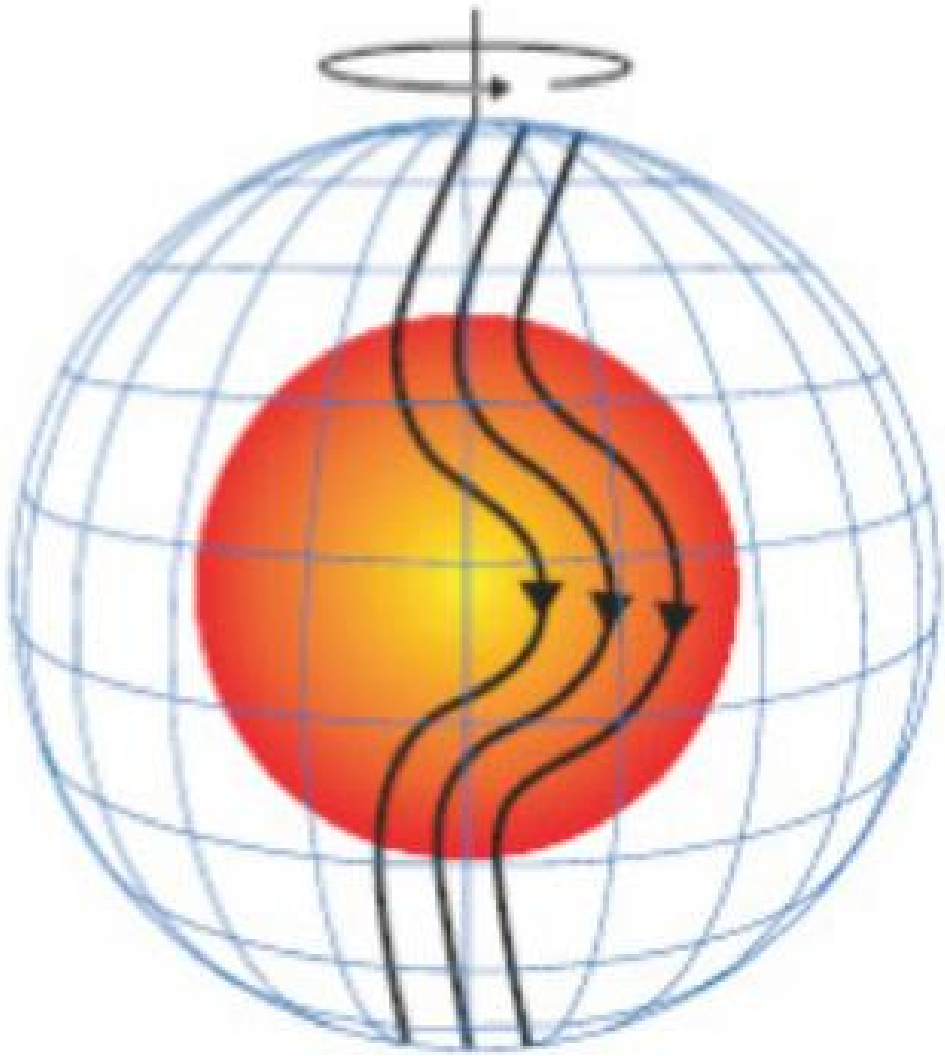

Figure 4.10: This schematic diagram illustrates the solar dynamo process, showing the Sun's internal structure with a red radiative core and a blue mesh representing the photosphere, separated by the convection zone. It depicts the generation of magnetic fields through differential rotation shearing poloidal field lines into toroidal fields at the base of the convection zone, followed by the buoyant rise of magnetic flux tubes that emerge at the surface as tilted bipolar regions. The diagram further shows the poleward transport of magnetic flux by meridional flow, which reverses the polar magnetic fields and returns some flux to the base of the convection zone, completing the cycle. (source: ref 127)

The irregular occurrence of grand minima observed in cosmogenic isotope records suggests that stochastic drivers in dynamo models are essential for reproducing long-term solar activity variability. Studies indicate that long-term fluctuations, including secular trends and extreme activity levels, originate from stochastic fluctuations in the driving parameters of the solar dynamo mechanism. [179][180][181][182] [183] For instance, random fluctuations in the angular momentum transport process and the Babcock-Leighton mechanism generate grand minimum and maximum-like periods in fully non-linear flux-transport dynamo simulations. [181] Thus, the inclusion of stochastic drivers supports the understanding that grand minima are a special state of the solar dynamo, distinct from normal or high activity phases, driven by chaotic or random processes within the solar interior. By solving the time-dependent Fokker–Planck equation, the studies evaluate how electron beams precipitate into the solar atmosphere, revealing that magnetic convergence significantly alters energy deposition. [184] Thus, the flare work is not an isolated phenomenon but part of a unified research programme where the same magnetic field configurations that predict grand minima also dictate the intensity and depth of flare heating. Observations of the 23 July 2002 flare reveal that sharp temporal increases in hard X-ray emissions are closely correlated with variations in the photospheric magnetic field, particularly around the apparent magnetic neutral line. [185] Cross-

correlation analysis of this event shows a noticeable positive correlation of 0.5–0.6 between temporal magnetic variations and HXR light curves, with a time lag no larger than 1–2 minutes across all energy bands. [186] These irreversible, steplike changes in magnetic flux, which reach a new steady state without returning to preflare values, demonstrate that magnetic field restructuring is responsible for initiating flare phenomena. [185] Observations of the 2006 December 14 X-class flare, utilizing GONG, Hinode, and RHESSI, revealed extended ribbon emission propagating through umbrae and penumbrae in both hemispheres, with energy deposition at the photospheric level occurring over a more confined area than the overlying chromosphere. [187] These measurements demonstrated asymmetries in hard X-ray source intensity and size between Northern and Southern ribbons, alongside strong impulsive changes in longitudinal magnetic flux at magnetic reversals. [187] Observations of the 23 July 2002 flare provide concrete evidence of this linkage, revealing that sharp temporal increases in hard X-ray (HXR) emissions are closely correlated in time with variations of the magnetic field measured in the photosphere. [185] Specifically, the magnetic flux change over the duration of this flare was approximately 1.2×10^{21} Mx, a significant alteration that occurred primarily around the apparent magnetic neutral line (AMNL). [185] Crucially, these magnetic field changes were found to be irreversible or steplike; the field reached a new level of steady state and did not return to its preflare value, a pattern consistent with theoretical expectations that irreversible magnetic changes are responsible for the initiation and development of flare phenomena. This connection is further strengthened by cross-correlation analysis, which shows a noticeable positive correlation of 0.5–0.6 between temporal magnetic variations covering the AMNL and HXR light curves, with a time lag no larger than 1–2 minutes for all energy bands. [186] Indeed, the presence of quadruple and sextuple magnetic field wave components appears to play a key role in initiating flaring activity, as these complex wave interactions can create the necessary conditions for magnetic reconnection and particle acceleration.

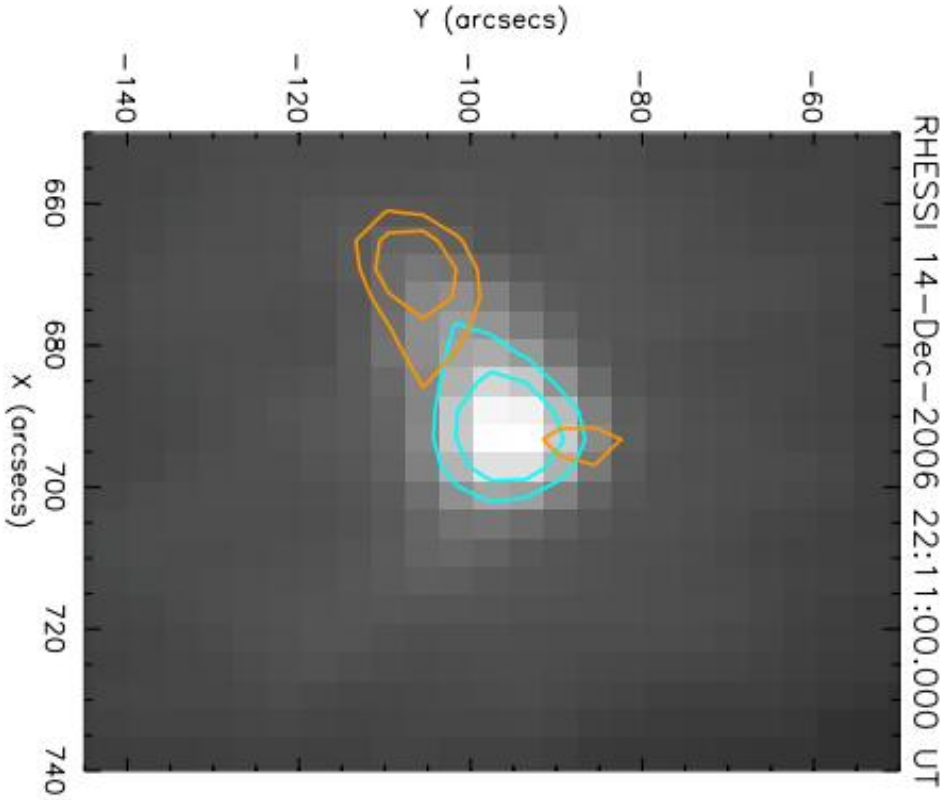

Figure 4.11: This image displays a time series of hard X-ray (HXR) solar flare observations from 22:08–22:15 UT on 14 December 2006, captured by RHESSI. The grayscale background represents 20–30 keV emission, with cyan contours outlining regions at 50% and 70% of the peak intensity. Overlaid orange contours indicate 40–100 keV emission at the same relative intensity levels, revealing the spatial distribution and energy-dependent structure of the flare emission across the solar surface. (source: ref 187)

5. The Sun's Inertial Motion

The Sun's barycentric orbit under Jupiter–Saturn–Uranus–Neptune forcing modulates insolation on decadal-to-centennial timescales via the Jose cycle and longer planetary-resonance beats.

5.1 How Exoplanets Reveal Stellar Wobble

This same observational principle, when turned inward, reveals that the Sun is not a fixed center but a wobbling star, its motion dictated by the gravitational pull of the giant planets. [169] To model this complex dance with precision, researchers employ semi-analytical planetary motion theory, specifically constructing an averaged Hamiltonian for the Sun–Jupiter–Saturn–Uranus–Neptune four-planet system. [188] Crucially, the Hori–Deprit method is applied to average the Hamiltonian, a process that eliminates short-period perturbations determined by terms containing the mean longitude. By removing these rapid oscillations, the method establishes a framework that allows for significantly larger integration time steps in the equations of motion, thereby enabling the study of orbital evolution over long-time scales. [189] The exclusion of short-period terms confirms that the long-term secular evolution of the system can be isolated from the immediate gravitational tugs of individual planetary conjunctions. [188] Consequently, the semi-analytical theory proves that the Sun's motion around the solar system barycentre is governed by stable, long-period cycles, such as the Jose cycle, which modulate the Sun–Earth distance on decadal-to-centennial timescales.

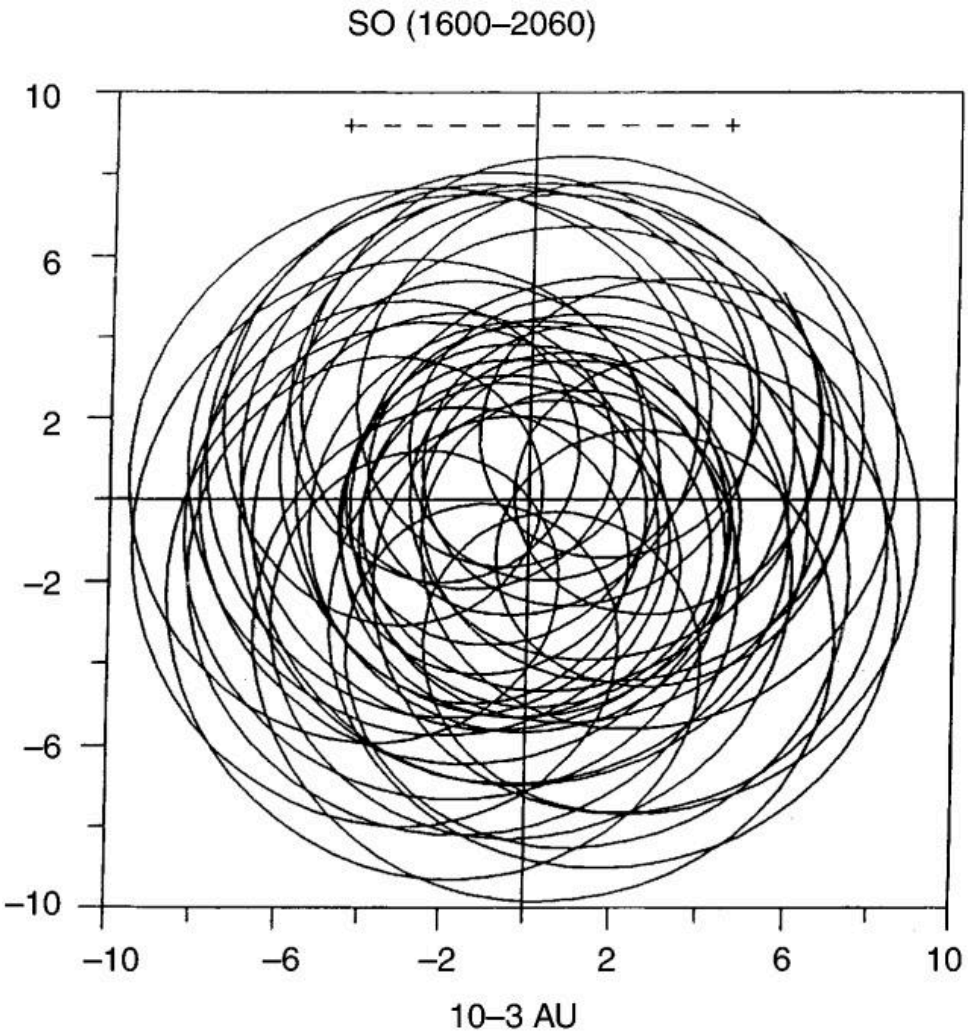

Figure 5.1: The figure displays a polar plot of the Sun's orbital path around the solar system barycenter from 1600 to 2060, with coordinates in units of 10^{-3} AU. The plot shows a complex, nested pattern of overlapping loops, indicating the Sun's motion due to gravitational interactions with the planets, primarily Jupiter and Saturn. A dashed horizontal line at the top represents the Sun's diameter, providing a scale reference for the orbital deviations. (source: ref 188)

Instead, computer algebra systems like Piranha are used to perform the complex symbolic manipulations required for high-order Hamiltonian expansions. This automated approach ensures that the generating functions and averaged Hamiltonians are derived without error, enabling numerical integration via methods such as the Everhart method. [190][190][188] This same principle applies to our own Solar System. [191] The Sun does not sit still; it orbits the barycenter, the center of mass, of the entire system. [192] The giant planets—Jupiter, Saturn, Uranus, and Neptune—dominate this motion. [188] Their combined gravity pulls the Sun in complex paths. [192] To verify these paths, scientists use numerical integration. [190] They compare different mathematical methods to ensure accuracy over long timescales. [189] One study compared the 15th-order Everhart method with the 11th-order Runge–Kutta method. [189] They integrated the equations of motion for the four giant planets. [189] This large motion affects the distance between the Sun and Earth. [162] Together, they shape the climate record.

The semi-analytical theory, constructed via the Hori–Deprit averaging method and Lie transformations, provides a framework for deriving averaged equations of motion from the Hamiltonian expanded in powers of planetary masses. However, the theory may be unacceptable near mean-motion resonances due to extreme growth in Hamiltonian terms, a limitation that suggests the need for complementary numerical simulations using symplectic integrators like NBI in such cases. Consequently, a hybrid strategy that combines semi-analytical insights with targeted numerical verification is likely to offer the most robust characterization of system dynamics. [190] Consequently, for systems exhibiting orbital flips or strong

resonances, numerical simulations using symplectic integrators are required to complement analytical results when studying phenomena like orbital flips. The real evolution of a system, including the actual presence of flips, can only be studied using numerical methods that preserve the analytical properties of functions without accumulating the rounding errors typical of purely numerical theories. [190][66] However, this technique possesses an inherent geometric limitation: because the orbital inclination of the planetary system relative to our line of sight is generally unknown, the measured velocity amplitude yields only a lower limit on the planetary mass, expressed as $M \sin I$. For instance, studies of flaring stars have shown that while criteria like the Reduced Proper Motion (RUWE) can help filter out obvious binaries, they are less sensitive to close companions with semi-major axes below 0.1 astronomical units, meaning that some level of uncertainty regarding the true nature of the companion remains. [193] This limitation does not carry over when we turn the same tool inward to our own Sun: its motion about the solar system's centre of mass is computed directly from the known planetary masses and orbits, with no inclination ambiguity and no M sin i lower bound. [194] Just as we detect the wobble of distant stars to infer the presence of unseen planets, we can calculate the Sun's motion around the Solar System barycentre due to the gravitational influence of the giant planets. [162]

5.2 Solar Inertial Motion SIM

The geometry of the Sun's motion around the Solar System barycentre is not a simple, smooth ellipse but a complex trajectory shaped by the gravitational pull of the giant planets, particularly Jupiter and Saturn. [169] This motion creates specific configurations of solar acceleration that have profound implications for solar activity. [192] Analysis of the normal component of solar acceleration, denoted as a_h, reveals exceptional increases at specific epochs, which are explained by the inversion of angular momentum when the Sun's orbit becomes retrograde. [192] This inversion aligns the angular momentum vector, L, towards the planetary acceleration direction, meaning that a_h represents the maximum projection of L in the solar acceleration direction, albeit in a contrary sense. [192] These changes are driven by orbital libration rather than an impulsive change in planetary acceleration, as planetary acceleration remains near the ecliptical plane. [192] However, these features are significant because they indicate that at times of angular momentum inversions, L is almost anti-parallel to the acceleration vector, with the angle between them oscillating between approximately 130 and 179 degrees. Crucially, these radial impulses never occurred before 1632 during the last millennium, even though similar planetary configurations did happen, demonstrating that these impulses arise only at epochs of orbital inversions and are responsible for particular phenomena. The periods of L_z inversion were characterized by a unique geometry of planetary acceleration with respect to the Sun-barycentre system, where the radial component of solar acceleration had an exceptional magnitude and the L vector was anti-parallel to acceleration. [192] However, further investigation is required to determine whether this relationship is causal or merely coincidental.

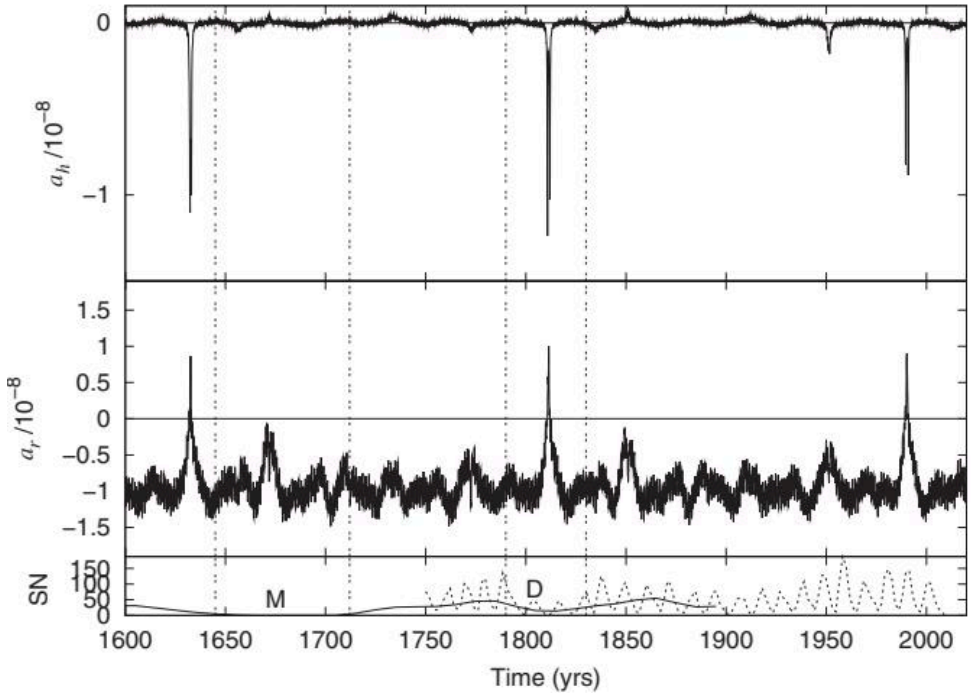

Figure 5.2: The chart displays three time-series plots from 1600 to 2000 CE: the normal acceleration a_h (top), radial acceleration a_r (middle), and sunspot number (SN, bottom). The sunspot number is shown as a solid line from a ^{14}C reconstruction (Solanki et al., 2004) and a dashed line representing observed-smoothed data. Vertical dashed lines mark the Maunder (M) and Dalton (D) Minima. Impulses in both acceleration components are clearly visible during the Maunder Minimum, the Dalton Minimum, and at the peak of solar cycle 22. The accelerations are in units of 10^{-8} astronomical units per day squared, with the sunspot number scaled from 0 to 1500. (source: ref 197)

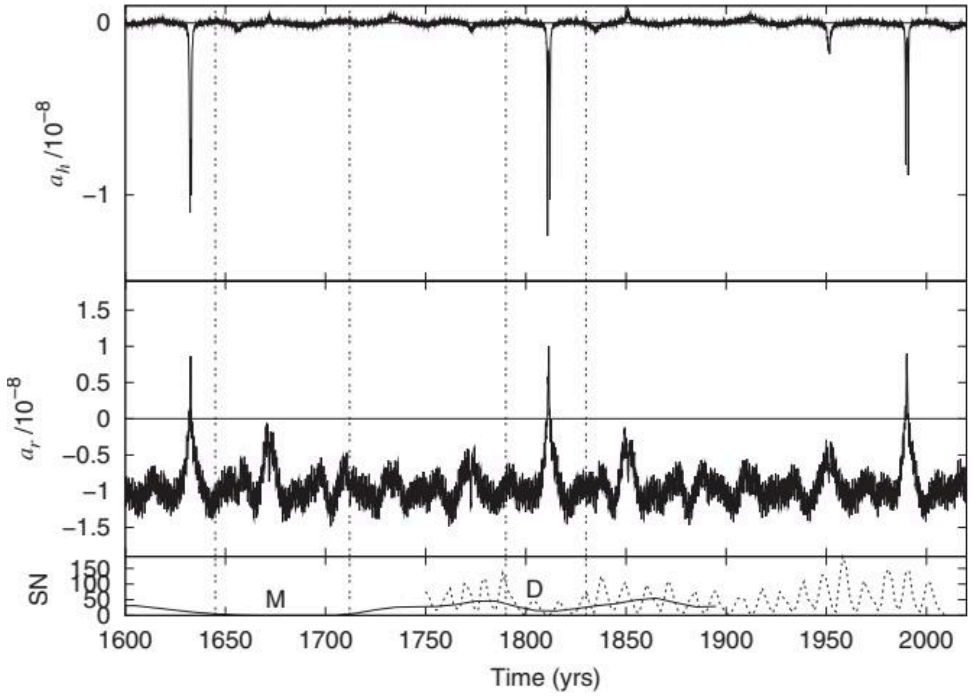

Figure 5.3: The chart displays three time-series plots from 1600 to 2000 CE: the normal acceleration a_h (top), radial acceleration a_r (middle), and sunspot number (SN, bottom). The sunspot number is shown as a solid line from a ^{14}C reconstruction (Solanki et al., 2004) and a dashed line representing observed-smoothed data. Vertical dashed lines mark the Maunder (M) and Dalton (D) Minima. Impulses in both acceleration components are clearly visible during the Maunder Minimum, the Dalton Minimum, and at the peak of solar cycle 22. The accelerations are in units of 10^{-8} astronomical units per day squared, with the sunspot number scaled from 0 to 1500. (source: ref 197)

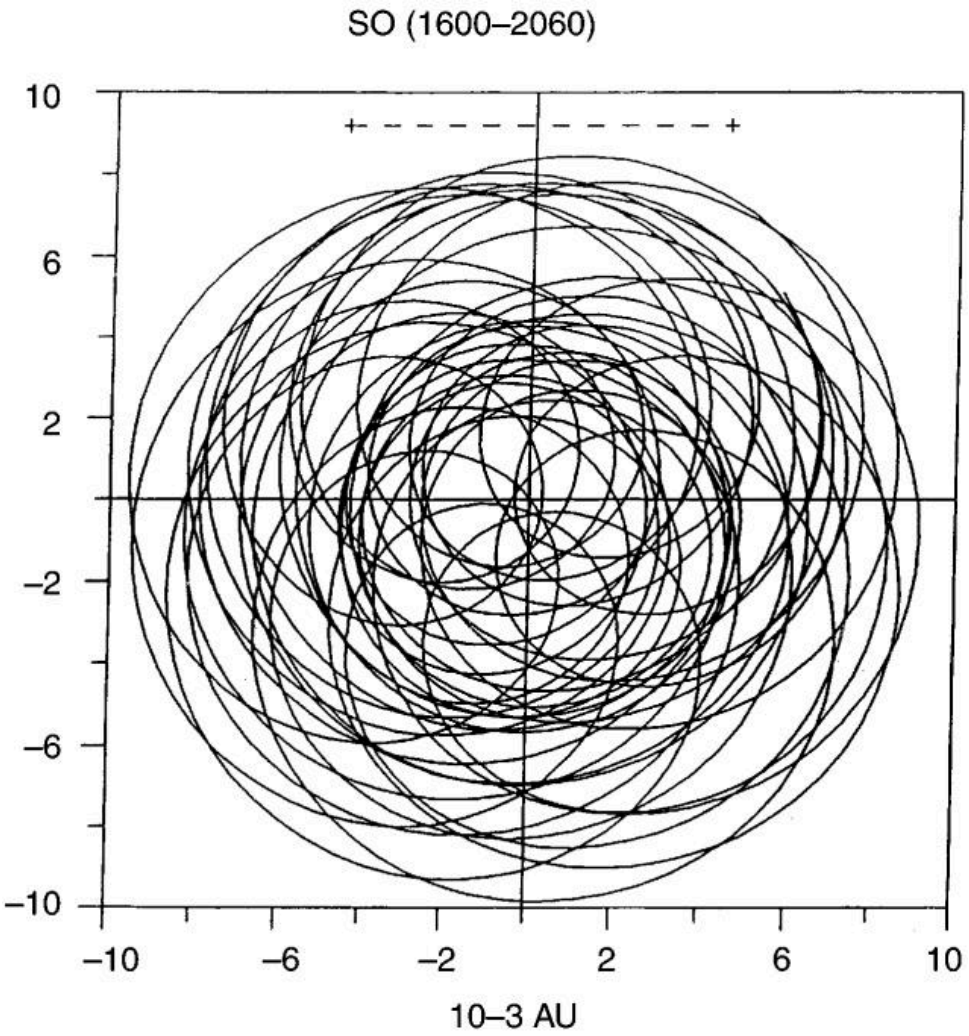

Figure 5.4: The figure displays a polar plot of the Sun's orbital path around the solar system barycenter from 1600 to 2060, with coordinates in units of 10^{-3} AU. The plot shows a complex, nested pattern of overlapping loops, indicating the Sun's motion due to gravitational interactions with the planets, primarily Jupiter and Saturn. A dashed horizontal line at the top represents the Sun's diameter, providing a scale reference for the orbital deviations. (source: ref 66)

Solar barycentric dynamics, derived from a new solar-planetary ephemeris, reveal that orbital inversions are not strictly periodic in terms of the Jose-period but appear in irregular groups of three to nine events. [195] These retrograde motion intervals manifest with a bimillennial cycle, averaging approximately 2.2 kyr, yet within these broader periods, they do not occur regularly at the Jose-period. [195] For instance, some intervals of retrograde motion are separated by about 140 yr, such as between the years 2168 and 2308 or between −2458 and −2318. [195] Although the Jose-period beginning at −2458 is maintained, with another orbital inversion occurring at −2279, an intermediate lapse of retrograde motion takes place at the year −2318, which is 39.26 yr before the expected event of the year −2279. [195] Notably, before the retrograde interval of the year −2994, all orbital inversions inside each bimillennial cycle occur at the Jose-period. [195] The explanation for these shorter periods is straightforward: at each Jose-period, which is strongly related to the Uranus–Neptune synodic period of ~171 yr, a quasi-conjunction between Jupiter and the other giants tends to occur. [195] However, these quasi-alignments are not always able to produce a solar retrograde motion because of the ever-changing planetary positions and velocities at these particular events.

Analysis of the Sun's barycentric dynamics reveals distinct radial impulses in solar velocity that align precisely with major periods of reduced solar activity. [192] This pattern demonstrates that radial impulses in the Sun's velocity occurred at the beginning of the Maunder Minimum and Dalton Minimum. The alignment of these impulsive accelerations with historical grand minima confirms a phenomenological

link between the barycentric motion of the giant planets and long-term solar cycle behavior. [66][192] Furthermore, the most recent impulsive event coincided with the maximum of cycle 22, preceding the current prolonged minimum of solar activity. Observational data show an apparent phase synchronization between sunspot numbers and the inclination of the orbital plane of the solar system barycenter, with correlation coefficients shifting from 0.76 to −0.52 after the radial impulse. [192]

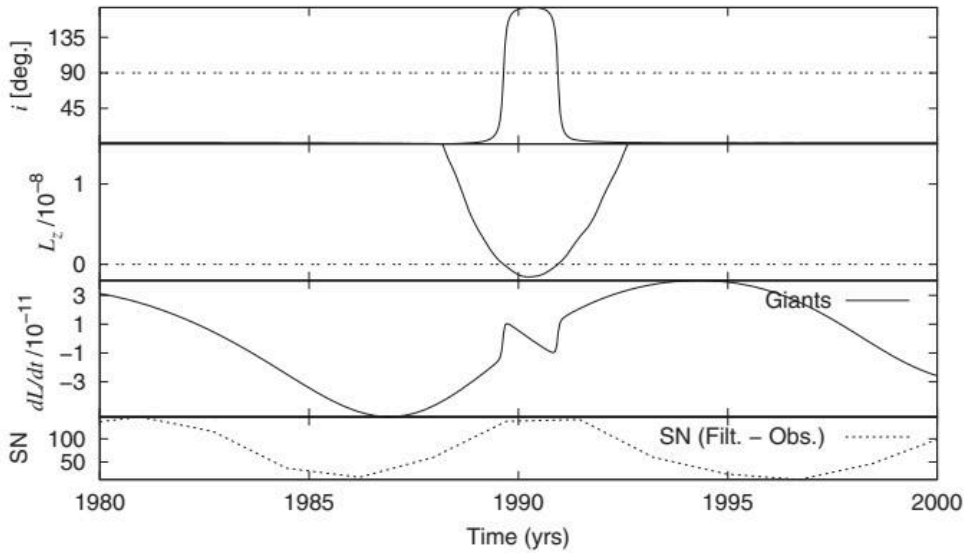

Figure 5.5: The chart displays four time series from 1980 to 2000: OSO inclination (i) in degrees, the Lz component of angular momentum in 10^{-8} AU²·M⊙·day⁻¹, the rate of change of angular momentum (dL/dt) for giant planets in 10^{-11} AU²·M⊙·day⁻², and the sunspot number (SN) in a filtered-observed form. The inclination i exceeds 90° around 1990, indicating retrograde motion. A strong anticorrelation is evident between dL/dt and SN, with dL/dt peaking during the sunspot minimum of cycle 22, which is prolonged compared to previous cycles. (source: ref 197)

Analysis of the Sun's barycentric dynamics reveals distinct impulsive events that correlate with major shifts in solar activity. [192] Specifically, a radial impulse in the Sun's velocity occurred at the maximum of Solar Cycle 22, before the present extended minimum. This timing is significant because it coincides with a violation of the Gleissberg–Ohl rule involving cycles 22 and 23. [192] Although the nature of the current prolonged minimum remains unconfirmed, the accumulation of spotless days is comparable to that seen near the Dalton Minimum. [196] The radial component, which points toward or away from the barycentre, exhibits particularly dramatic changes during episodes of planetary quasi-alignments. [195] During these intervals, the Sun's path undergoes orbital inversions, where the direction of its motion relative to the barycentre reverses. [192] The sudden changes in radial acceleration are so significant that they dominate the overall coplanar acceleration, which is the vector sum of the radial and tangential components. [192] These spikes in acceleration occur when the Sun fails to loop the barycentre, a phenomenon that happens when the barycentre lies outside the Sun's orbital path. [192] This geometric configuration is a direct result of the specific alignments of the planets, which exert a combined gravitational force that pulls the Sun in a particular direction. [192] The magnitude of these acceleration spikes is much larger than the average values observed during other phases of the solar inertial motion. [192] The exceptional magnitude of the radial acceleration during retrograde intervals provides a clear signature of the planetary forcing on the Sun's motion. [192] The separation of these two influences allows for a more precise understanding of the factors that drive solar variability. [116]

5.3 The Jose Cycle and Longer Beats

Power spectra of the sunspot record demonstrate that the 11-year Schwabe sunspot cycle is made up by three interfering cycles, which can be interpreted as due to the 9.93-year spring tidal cycle between Jupiter and Saturn, the 11.86-year Jupiter orbital tidal cycle, and a central oscillation of about 10.87 years that is almost, but not precisely, the average between the two tidal cycles and may emerge from the solar dynamo cycle as a collective synchronization harmonic. [198] This structure suggests that the 11-

year Schwabe sunspot cycle consists of three periods linked to planetary orbital periods, including the Jupiter/Saturn spring period. Scafetta [11, 12] also noted that there are gravitational recurrence patterns of about 11.07-11.08 years due to the Mercury-Venus system and the Venus-Earth-Jupiter system, which correspond to the average solar cycle length. [198][119] Thus, numerous planetary tidal oscillations resonate around the 11-year Schwabe solar cycle, as postulated by Wolf. Taking these considerations into account, a simple solar model was developed by Scafetta involving just three harmonics, namely the two Jupiter/Saturn tidal cycles and a hypothetical solar dynamo cycle with a 10.87-year period. [198] This model reproduces a varying 11-year cycle that correlates approximately with the Schwabe sunspot cycle, and produces beats at about 61 years, 115 years, 130 years and 983 years, which are synchronous with major solar and climatic multidecadal, secular and millennial oscillations observed throughout the Holocene. [198] The model recovers the Roman Warm period, Dark Ages Cold Period, Medieval Warm Period, Little Ice Age, and Current Warm Period. [117] Instead of linking the periods of Sun's long-term cycles to corresponding periods of planetary influences, another concept is pursued in which long-term cycles emerge as beat periods between the basic Hale/Schwabe cycle with the typical synodic periods of Jupiter with other Jovian planets. [119] The beat period of 193 years, as resulting from the 22.14-year Hale cycle and the 19.86-year synodic cycle of Jupiter and Saturn, has been noticed by several authors. [119] The aim is to corroborate how such beat periods actually emerge in a specific solar dynamo model, which had already demonstrated synchronization of the Schwabe cycle with the 11.07 years tidal period, based on the resonance of the intrinsic helicity oscillations of the current-driven m = 1 Tayler instability with the m = 2 tidal forcing. [119] The geometry of this solar orbit is essentially planar, with the Sun moving in the plane of the solar system, allowing for a clear separation into ordered and disordered orbital types. [66] This millennial-scale variability is further confirmed by analyses of the solar background magnetic field baseline, which reveal weak oscillations with a period of 2000 ± 95 years. [162] This millennial-scale oscillation is characterized by clustered occurrences of grand minima and maxima around its lows and highs, respectively, indicating a solar origin rather than purely climatic or geomagnetic variability. [106] The correspondence between the semi-Hallstatt cycle and the Eddy cycle indicates that the longer Hallstatt period is composed of two ~1000-year oscillations, corresponding to the Eddy cycle. This interpretation implies that the ~2200-year Hallstatt cycle may not be a fundamental solar mode, but rather an emergent property of two superimposed ~1000-year Eddy cycles. [35][8][106][15][104]

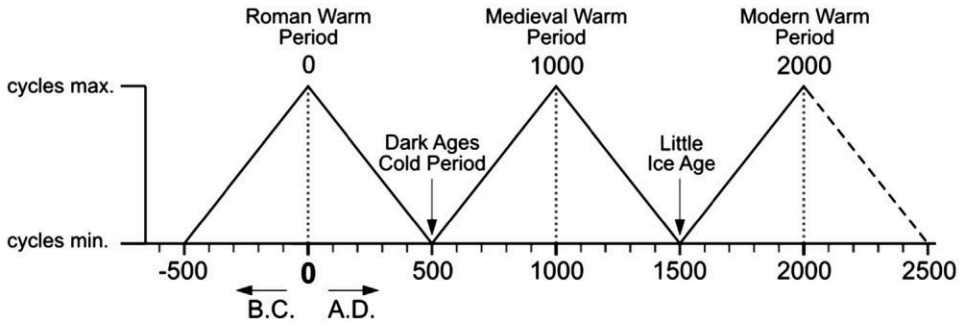

Figure 5.6: The figure illustrates a schematic sketch of the 1000-year Eddy solar activity cycle, showing a repeating triangular pattern of solar maxima and minima over time. The x-axis represents time in years before and after the Common Era (B.C. and A.D.), with labeled historical warm periods—Roman Warm Period, Medieval Warm Period, and Modern Warm Period—corresponding to solar maxima, and cold periods—Dark Ages Cold Period and Little Ice Age—aligning with solar minima. The current position is at the peak of the modern maximum, indicating that solar activity is expected to decline over the coming centuries, reaching a minimum around 2500. (source: ref 8)

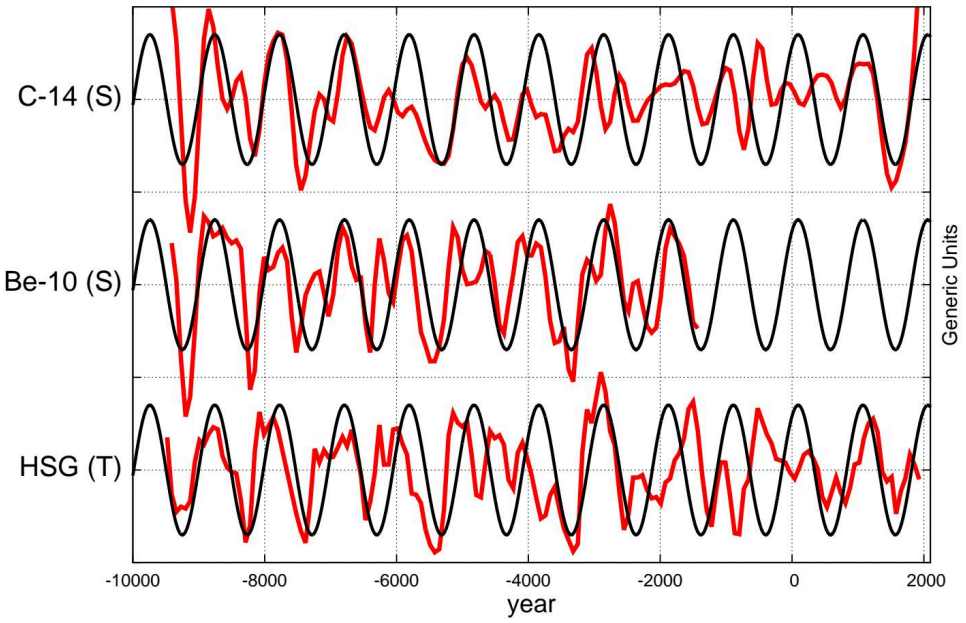

Figure 5.7: The figure displays three time-series plots spanning the Holocene, comparing solar activity proxies (carbon-14 and beryllium-10) and a global temperature proxy (HSG) against a modeled solar harmonic function. The top two panels show the C-14 (S) and Be-10 (S) records, while the bottom panel shows the HSG (T) record, all plotted against a common calendar year axis from −10,000 to 2000. A black harmonic function with a period of 983.4 years and a phase of 2059.7 A.D. is overlaid on each series, illustrating a strong millennial-scale oscillation. The plots reveal a relatively good correlation between the solar and climate records and the modeled harmonic, with correlation coefficients of 0.43 for C-14, 0.30 for HSG, and 0.57 for Be-10, all statistically significant ($P < 0.1\%$). (source: ref 117)

Analysis of the Holocene solar activity record reveals that the occurrence of grand minima is defined by stochastic or chaotic processes rather than long-term cyclic variations. Researchers examined possible quasi-periodicities in the rate of grand minima and maxima occurrence, finding only a weak, marginally significant quasi-periodicity of 2000–2400 years, a period well-known in ^{14}C data. [147][199][128][162] No other periodicities were observed in the occurrence rate of grand minima. [200] While a marginal hint for a periodicity of about 1200 years and its harmonics appeared in SN-S data for grand maxima, no periodic feature was found in the SN-L series. [200] This indicates that the 2400-year periodicity is related likely to the clustering of grand minima rather than to a long-term “modulation” of solar activity. [200] [116]

The statistical analysis of solar activity over the last millennia, derived from cosmogenic isotope records in natural terrestrial archives and historical sunspot data, reveals that the Sun spends the majority of its time at moderate activity levels, with approximately one-sixth of that duration characterized by a Grand minimum state and intermittent periods of Grand maximum activity. [199] While the occurrence of these extreme states is not the result of long-term cyclic variations but is instead defined by stochastic or chaotic processes, a distinct pattern emerges when examining the clustering of these events. [43] This long-term clustering is supported by the presence of a well-known period in radiocarbon data, as noted by Damon and Sonett and Vasiliev and Dergachev, which aligns with the marginally significant quasi-periodicity identified in the analysis. [200] The distinction between the clustering of grand minima and the occurrence of grand maxima is further clarified by the absence of periodic features in the grand maxima occurrence rate in the SN-L series, although a marginal hint for a periodicity of about 1200 years and its harmonics is found in SN-S data. [200] This evidence supports the conclusion that the 2400-year periodicity is related likely to the clustering of grand minima rather than to a long-term modulation of solar activity. [200]

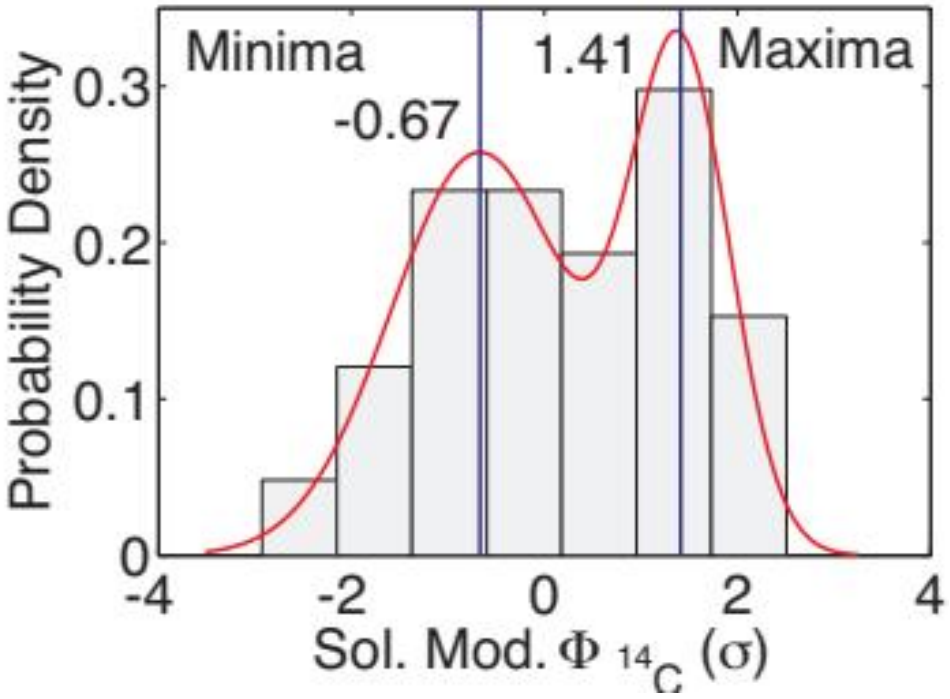

Figure 5.8: The image displays two overlapping histograms of solar modulation potential (Φ_{14}) reconstructed from GRIPI[10]Be and IntCal13[14]C data over the Holocene, with probability density plotted against Φ_{14} (σ). A bimodal Gaussian distribution is fitted to the combined data, shown as a red line, highlighting two distinct modes: a minimum at −0.67σ and a maximum at 1.41σ. Vertical lines and text labels identify the threshold values used to classify grand minima and grand maxima in solar activity. (source: ref 201)

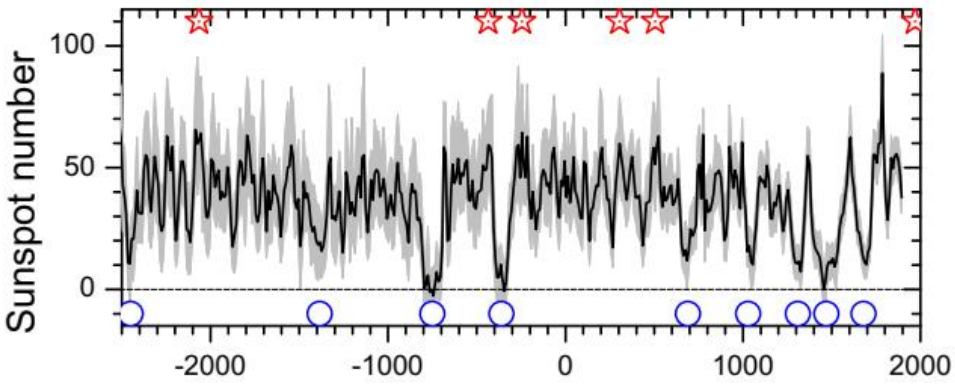

Figure 5.9: This figure displays decadal sunspot activity reconstructed from ^{14}C data over the Holocene, with the y-axis showing sunspot number and the x-axis representing time in years before present. The plot reveals a fluctuating solar activity pattern, with blue circles marking grand minima and red stars indicating grand maxima, highlighting periods of significantly reduced and enhanced solar output, respectively. (source: ref 106)

5.4 Harmonic Analysis Yndestad and Abdussamatov

To isolate the long-term gravitational influences of the giant planets on the Sun's motion, researchers must first strip away the rapid, short-period oscillations that dominate immediate orbital dynamics. [188] This separation is achieved through semi-analytical planetary motion theory, which relies on advanced mathematical techniques to average the Hamiltonian of the system. The Hori–Deprit method, a cornerstone of this approach, uses Lie transformations to systematically eliminate short-period perturbations from the equations of motion. By removing these high-frequency noise terms, the method allows for a

much larger time step in the numerical integration of the equations of motion, making it feasible to model the slow, secular evolution of planetary orbits over centuries or millennia. [190] In recent implementations, such as those using the computer algebra system Piranha, the Hamiltonian of the four-planetary problem is expanded into a Poisson series in osculating elements of the second Poincare system. [190] The transformation between the original osculating elements and the new averaged elements is defined by change-variable functions derived from the second approximation of the Hori–Deprit method. [190]

The algorithm proceeds by deriving second-order terms, H_2 and T_2, through the same procedural logic applied to first-order terms, maintaining consistency across the expansion hierarchy. [190] Crucially, the calculation of Poisson brackets, such as $\{T_2, h_1 + \langle h_1 \rangle\}$, involves decomposing the expression into constituent parts like $\{T_2, h_1\}$ and $\{T_2, H_1\}$, with partial derivatives of T_2 serving as change-variable functions computed by the $chn\_n(2)$ script. This semi-analytical approach, constructed with computer algebra systems like Piranha to handle complex symbolic manipulations, contrasts sharply with purely numerical theories that yield only single trajectories and accumulate rounding errors. Instead, semi-analytical theories show insights into phase space properties and long-term stability, establishing a clearer view of the system's dynamical behavior over extended periods. Applications to the Sun–Jupiter–Saturn–Uranus–Neptune system demonstrate the quasi-periodic nature of planetary motion up to 10 Gyr, with numerical integration of the averaged equations using Gragg–Bulirsch–Stoer and Everhart methods showing excellent agreement with numerical motion theories. [189][188][190] Specifically, simulations of the Sun–Jupiter–Saturn–Uranus–Neptune system over 100 Myr utilized the modified 15th-order Cowell–Störmer integrator and the symplectic Wisdom–Holman integrator, initialized with barycentric coordinates from the DE 430 ephemeris. [188] The results demonstrate that the osculating orbital elements derived from averaged equations maintain strong qualitative agreement with these direct numerical methods. [190]

The orbital evolution of the Sun–Jupiter–Saturn–Uranus–Neptune system on long time scales was studied using a Hamiltonian expansion into the Poisson series in elements of Poincaré second system, constructed up to third degree in the small parameter. [188] The estimation accuracy of this Hamiltonian expansion was evaluated by orbital elements of the Solar System's giant planets, reaching about 10^{-12}. [188] The averaged Hamiltonian and the equations of motion in averaged Poincaré elements were constructed by the Hori-Deprit method up to third degree of the small parameter, with functions for the change of variables obtained in second approximation to transform between osculating and averaged orbital elements. [190] These constructed analytical equations of motion were applied to study the orbital evolution of the Solar System's giant planets on long time scales with high precision, showing that the amplitudes and periods of the planetary motion are in good agreement with numerical theories. [188] The short-periodic perturbations of the orbital eccentricities and inclinations save small values over the entire interval of the integration. [189] Furthermore, the integration of the equations of motion with slightly different initial values of Uranus' semi-major axis showed that the Lyapunov time for the orbits of giant planets is about 10–30 Myr. If the difference between the perturbing functions in the first and second approximations exceeds an amount obviously larger than the small parameter, this may testify to the presence of a resonance whose strength increases with this difference. [189]

The construction of semi-analytical theories for the orbital evolution of planetary systems, primarily focusing on the Sun–Jupiter–Saturn–Uranus–Neptune system and specific extrasolar systems such as HD 39194, HD 141399, and HD 160691, relies heavily on the Hori–Deprit averaging method. This framework utilizes Lie transformations to derive averaged equations of motion from the Hamiltonian expanded in powers of planetary masses, contrasting with purely numerical theories that provide only single trajectories and accumulate rounding errors. The process involves computer algebra systems, specifically Piranha, to handle complex symbolic manipulations for high-order approximations, expanding the Hamiltonian using Jacobi coordinates and the second system of Poincaré elements. [190] However, for extrasolar systems, the theory may be unacceptable near mean-motion resonances due to extreme growth in Hamiltonian terms. The real evolution of a system in this case, including the real presence of flips, can be studied only using numerical methods, confirming that symplectic integrators are essential for cases involving mean-motion resonances or orbital flips where analytical series diverge. Thus, the semi-analytical approach is best suited for secular evolution far from resonances, whereas numerical integration remains indispensable for capturing chaotic dynamics and resonance crossings. [202][189][188]

5.5 How Planetary Forcing Reaches Earth S Climate

The statistical consistency between periodic spiral arm crossings, cosmic ray flux variations recorded in meteorites, and glaciation epochs over the past billion years suggests that these signals are not random phenomena. [202] By combining eight total measurements of HI data, the predicted spiral arm crossing

period is estimated at 134.6 ± 22 Myr, while the period derived from Fe/Ni meteorites for cosmic ray flux variation is 143.6 ± 10 Myr. [202] These values align closely with the average observed recurrence period of glaciations on Earth, which stands at 145.5 ± 6.7 Myr. [202] A best-fit analysis comparing the actual prediction for the location of the spiral arms to the glaciations yields a periodicity of 143.65 Myr, suggesting that the phase of all three signals fits the predictions. [202] Specifically, the average mid-point of glaciations lags by 33.6 ± 20 Myr after the spiral arm crossing, consistent with the predicted lag of 31.6 ± 8 Myr. [202] Furthermore, the CR exposure ages of iron meteorites cluster around troughs in the glaciations, reinforcing the link between increased cosmic ray flux and reduced global temperature. This alignment suggests a non-random phenomenon for the appearance of glaciations with high statistical significance, indicating a potential connection between galactic structure and Earth's climate history. Consequently, the data suggest that galactic environmental factors may play a significant role in modulating terrestrial climate cycles. [202] Thus, the SIM topology provides a potential mechanical basis for understanding how planetary forcing modulates insolation over long timescales, independent of internal solar dynamo processes.

Solar wind variations interact with the Earth's magnetosphere, a process that suggests changes in the planet's rotation rate during solar minima. [203] This interaction alters the Earth's total moment of inertia and atmospheric angular momentum, causing the interior rate of rotation to adjust as reflected in measured length-of-day variations. [204] These rotational shifts are associated with influences on ocean circulation and climate, particularly evident in the North Atlantic where speeding-up periods at grand solar minima may control main ocean surface circulation and Gulf Stream directional shifts. [203] The link between solar variability and terrestrial responses appears to go via the interaction of the Solar Wind with the Earth's magnetosphere, which is consistent with observed rises and falls in sea level in the Indian Ocean. [176] Furthermore, the semi-annual component of changes in the Earth's speed of rotation responds to changes in solar activity, supporting the idea that zonal wind circulation changes affect the speed of rotation of the planet. The Maunder Minimum time period, characterized by a lack of visible sunspots as noted by Eddy 1976, serves as a likely recent instance of reduced solar activity producing a noticeable effect on the climate system. [45] These findings challenge the notion that solar minima had negligible impact, suggesting that reduced solar activity significantly altered the thermal structure of the North Atlantic, thereby influencing global climate dynamics during these historical periods. [49]

The phasing of solar cycles indicates that a New Grand Solar Minimum may arrive by 2030–2040 — squarely inside the 2020–2053 window this book adopts — a prediction supported by convergent data from multiple independent analyses. [176] Dr. Theodor Landscheidt's research at the Schroeter Institute for Research in Cycles of Solar Activity suggests a long period of cool climate with its coldest phase around 2030 — again within the 2020–2053 window — aligning closely with the author's own calculations for the bottom of the next solar hibernation. [46] Peter Harris concludes there is a 94 percent probability of imminent global cooling. [46] Dr. S. Duhau and C. For the centuries preceding modern instrumentation, researchers have turned to cosmogenic radionuclides, specifically ^{10} Be and ^{14} C, preserved in ice cores and tree rings, to reconstruct long-term trends in solar activity. [43] These isotopes are produced in the Earth's atmosphere by nuclear reactions of cosmic ray particles with atmospheric nitrogen and oxygen, serving as a natural neutron monitor for cosmic radiation intensity. [52] However, it is crucial to recognize that these records do not measure total solar irradiance directly; instead, they reflect the modulation of galactic cosmic rays by the heliospheric magnetic field. Studies of Antarctic ice cores from the South Pole and Dome Fuji stations indicate that ^{10} Be variations provide a valuable proxy of solar activity, though complex production pathways and atmospheric transport processes impede quantitative interpretation. [63] Thus, while the planetary forcing mechanism provides the external trigger, the cosmogenic record confirms that the Sun's magnetic response, not just its geometric position, is the variable that couples to Earth's climate system.

6. The Cloud Hypothesis: Cosmic Rays and Climate

Galactic cosmic rays seed low-cloud condensation nuclei via ion-induced aerosol nucleation; the Sun modulates this flux; this controls albedo and surface temperature.

6.1 How Cosmic Rays Reach the Lower Atmosphere

Before galactic cosmic rays can influence Earth's climate, they must first navigate the vast expanse of the heliosphere, the region of space dominated by the Sun's outflowing magnetized solar wind. [43] The solar wind is not merely a stream of plasma; it carries the Sun's magnetic field, known as the interplanetary magnetic field, which permeates interplanetary space. [205] The strength of this shielding varies with solar activity, modulating the flux of incoming galactic cosmic radiation that reaches the inner solar system. [158] When the Sun's magnetic field is strong, particularly during solar maximum, it effectively deflects these charged particles, preventing them from penetrating deeply into the planetary system. [206] Conversely, during periods of low solar activity, such as the Maunder Minimum, the weakened magnetic field allows greater penetration of galactic cosmic rays. [14] This modulation mechanism suggests that the interplanetary magnetic field carried by the solar wind shields the heliosphere from galactic cosmic radiation. The variability in this shielding is crucial because it determines the intensity of cosmic rays that eventually collide with Earth's atmosphere. [207][206][208][114][209][60] It is within these denser layers that atmospheric ionization occurs, creating the conditions necessary for potential cloud-seeding effects. [210]

The flux of galactic cosmic radiation reaching Earth is modulated by solar variability, a relationship that suggests the Sun's control over this incoming particle stream on solar cycle timescales. This modulation arises because the solar wind, carrying the solar magnetic field, shields the inner solar system from high-energy galactic particles. [211][95][212][96][206][213] During periods of high solar activity, this shielding intensifies, reducing the cosmic ray flux that penetrates to Earth. [122] Conversely, during solar minima, the weakened heliospheric magnetic field allows a greater influx of these particles. [214] These high-energy charged particles, primarily protons and alpha particles originating from supernovae, collide with air molecules to produce a variety of secondary particles, including X-rays, gamma rays, neutrons, and heavy ions. [215] While the atmosphere largely protects the surface from destructive radiation, the secondary cascade remains critical for understanding how cosmic rays influence lower atmospheric chemistry and cloud formation mechanisms. [206]

When energetic cosmic rays strike the Earth's atmosphere, they initiate a complicated nucleonic-muon-electromagnetic cascade that ionizes the ambient air across various altitudes. [211][104] Modeling of cosmogenic isotope production, such as ^{7}Be, reveals that the most effective energy for particle interaction shifts from approximately 1 GeV/nucleon in the stratosphere to about 3 GeV/nucleon in the lower troposphere as altitude decreases. [216] This process releases secondary particles, including protons, neutrons, and muons, which penetrate deeper into the atmospheric layers. [104] The cascading effect continues until particle energy falls too low for further collisions, generally ending around 16 kilometers above the surface in the lower atmosphere. [206] Within this region, below 16 km, muons and electrons from high-energy collisions are the primary contributors to charged particle intensity. The ions produced within the troposphere by these cosmic rays serve as an important element of aerosol production. [217][211] [206][207][218] Specifically, ionization contributes to the gas-particle formation of ultra-fine aerosols, smaller than 20 nanometers, which build into cloud condensation nuclei. [219] Consequently, water vapor condenses into larger water droplets that form clouds, linking the initial cosmic-ray impact to the final cloud structure. These ions are critical because they serve as likely candidates responsible for observed correlations between cosmic ray intensities and cloud or aerosol parameters. [220] Consequently, ion chambers at the top of the atmosphere show a very much larger modulation with the solar cycle than instruments at sea-level, with a change in ionization at 10 mb bound to be approximately a 50 per cent reduction between sunspot minimum and sunspot maximum. In controlled chamber experiments simulating conditions found in the lower troposphere over oceans, researchers observed that the production of new

aerosol particles is proportional to the negative ion density. [221] These experiments utilized a mercury discharge lamp to initiate photochemical reactions, producing sulfuric acid through the photolysis of ozone and subsequent reactions with sulfur dioxide, oxygen, and water. [221] Ionization was achieved through cosmic radiation, natural radon decay, and a 35 MBq Cs-137 gamma source, allowing for precise measurement of ion pair production rates ranging from approximately 3.7 to 35 cm^{-3} s^{-1}. [222] These findings suggest that ions are active in continuously generating a reservoir of small thermodynamically stable clusters that can rapidly grow in the presence of condensable vapors. [221] This ion-mediated chemistry provides a plausible explanation for nucleation events that cannot be accounted for by classical nucleation theory alone. [221] Further field studies are therefore needed to quantify the relative importance of ion-induced nucleation in the global aerosol budget. [223]

6.2 Forbush Decreases the Natural Experiment

To understand this mechanism, we must look to the young solar twin κ^1 Ceti, a star that provides a crucial case study for how solar activity affected the climate during the early history of the Earth. [212] When these ejections are directed toward the Earth, they trigger sudden and significant reductions in the influx of galactic cosmic rays over time scales ranging from hours to days, a phenomenon known as Forbush decreases. These temporary dips in cosmic ray flux are not merely theoretical curiosities; they serve as natural experiments that allow scientists to observe the immediate atmospheric response to changes in ionization. [212][213][219][202][60] While such large Forbush decreases are too rare in the modern era to have a significant ongoing effect on the Earth's climate, their impact may have been far more profound in the distant past. [212] Four billion years ago, when life started to evolve on the Earth, coronal mass ejections were expected to be much more common on the early Sun, suggesting that the reduction in galactic cosmic ray influx originating from Forbush decreases could have been significant compared to the reduction from the Sun's more effective shielding at that time. [212] By using the flare rate of κ^1 Ceti to estimate the coronal mass ejection rate, scientists can gauge how common these events would have been on an Earth-like planet around such a young star, offering a window into the climatic conditions that shaped the origins of life. [212]

Forbush decreases, sudden drops in cosmic ray flux caused by coronal mass ejections, serve as natural experiments to test hypotheses about solar influences on Earth's weather and clouds. These events are ideal for isolating the link between cosmic rays and clouds because they produce a sharp, transient signal lasting for a week or two. [96][60][213] Observations using three independent cloud satellite datasets and one aerosol dataset reveal a clear response in clouds and aerosols to these decreases. [224] The data shows that reductions in the cosmic ray flux translate into changes in cloud properties, with the timing difference between the cosmic ray minimum and the cloud response reflecting the time it takes for aerosols to grow into cloud condensation nuclei. [224]

Solar coronal mass ejections generate plasma clouds that sweep past Earth, triggering sudden, week-long drops in galactic cosmic ray flux known as Forbush decreases. [219] These rare events provide a natural experiment to test the causal chain from solar activity to cloud formation. [224] Analyses of the five strongest Forbush decreases between 1990 and 2005, utilizing three independent cloud satellite datasets and one aerosol dataset, demonstrate clear signals of changes in low cloud liquid water content. The data reveal a distinct delay of five to seven days between the minimum in cosmic rays and the subsequent response in clouds and radiative forcing. [225][60][212][219][96] The observed reduction in cloud properties, particularly in low liquid clouds over the oceans, confirms that the entire chain—from cosmic rays to aerosols to clouds—is active in the Earth's atmosphere. [225] By isolating these strong events, researchers maximized the signal-to-noise ratio, establishing a statistically significant linear relationship between the strength of the Forbush decreases and the globally averaged shortwave radiation response. [225]

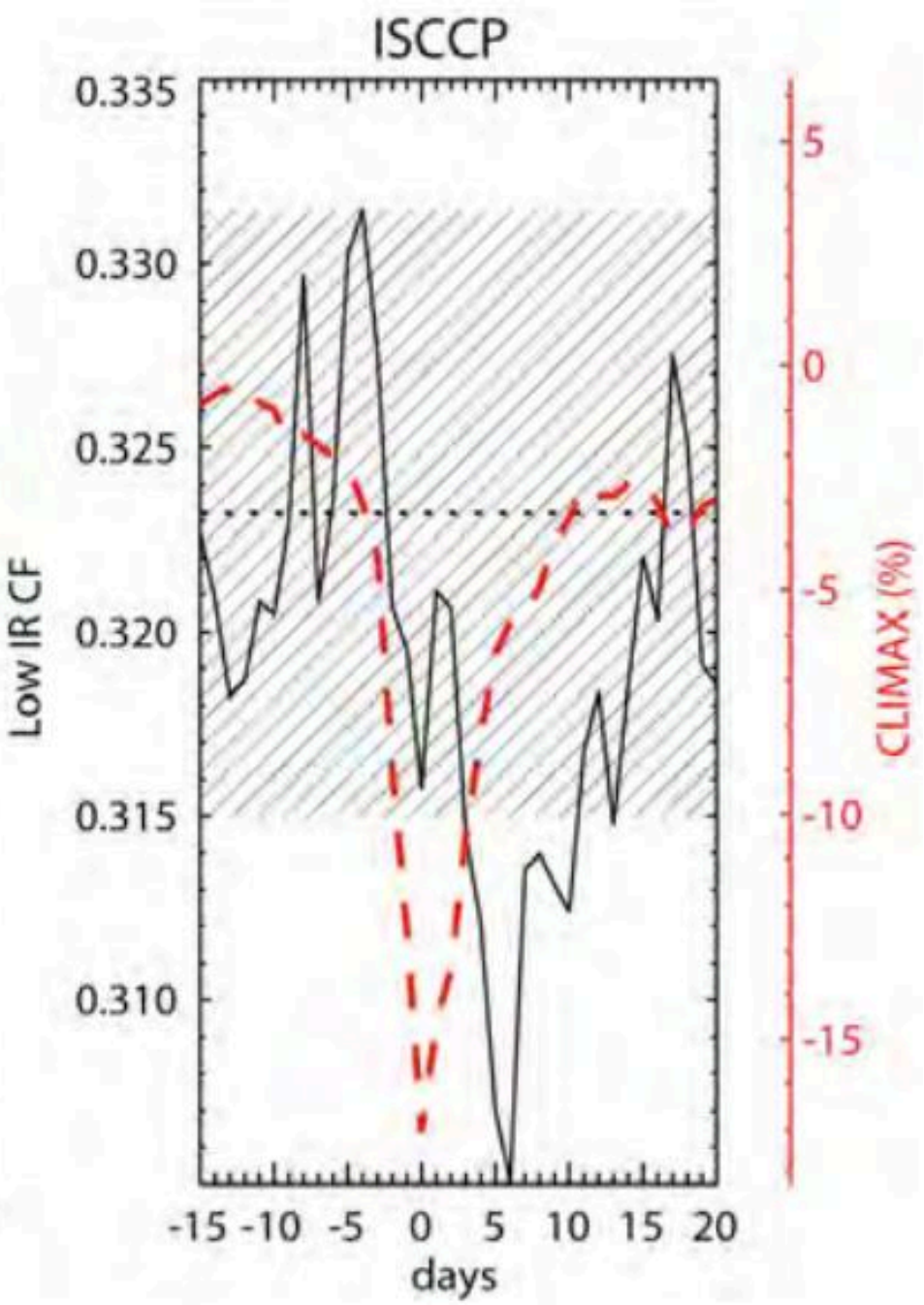

Figure 6.1: This figure displays the daily average low infrared-detected cloud fraction (Low IR CF) from ISCCP data (left y-axis, black line) and the CLIMAX cosmic ray flux (right y-axis, red dashed line) relative to Forbush decreases, averaged over five strong events from 1987 to 2005. The data shows a significant drop in low IR cloud fraction around day 0, coinciding with the minimum in cosmic ray flux, with the cloud fraction recovering in the days following the event. (source: ref 207)

When coronal mass ejections directed toward Earth cause sudden, week-long drops in galactic cosmic ray influx known as Forbush decreases, they provide a natural experiment to test atmospheric responses. [219] Specifically, these observations demonstrate that Forbush decreases are associated with changes in the relative abundance of fine atmospheric aerosols, establishing a link from solar activity through cosmic rays to aerosols and finally to clouds. The delay between the cosmic ray minimum and the cloud parameter minimum reflects the time required for aerosols to grow into cloud condensation nuclei. [226] [60][212][219][96][202] During these influential recent events, liquid water in the oceanic atmosphere decreased by as much as seven percent, confirming that the whole chain of effects is active in the real

atmosphere. [224] This discernible response supports the hypothesis that cosmic ray ionization controls the number of cloud condensation nuclei, thereby affecting Earth's climate. [219] Statistical analyses of these events reveal distinct atmospheric signatures, particularly in polar regions. [225] Studies by Pudovkin and Veretenenko reported a reduction of mean cloud cover following Forbush decreases at high latitudes greater than 60°N, while Roldugin and Tinsley found associated changes in atmospheric transparency at latitudes exceeding 55°N. These observations suggest that the sudden drop in ionizing radiation is associated with measurable alterations in cloud properties and optical depth. [227][213][60][96][202][212] While early studies by Pudovkin and Veretenenko reported cloud cover reductions at high latitudes, subsequent research by Kniveton and Tinsley, as well as Todd and Kniveton, identified zonal mean total cloud anomalies associated with Forbush decreases, particularly in polar and equatorial regions. These findings suggest that the primary effect of cosmic rays may relate to vorticity and cyclogenesis, especially during cold seasons in high-latitude areas. [202][213][212][96][60]

The natural experiment provided by Forbush decreases offers a critical test of the cosmic ray–cloud hypothesis, isolating the mechanism from long-term solar trends. [219] These events, triggered by coronal mass ejections that send plasma clouds past Earth, cause sudden, short-term drops in cosmic ray flux lasting a week or two. [219] The data revealed a clear, reproducible response in both clouds and aerosols, with the timing of the minima offset by the time required for aerosols to grow into cloud condensation nuclei. [219] This latitudinal gradient aligns with theoretical expectations for cosmic ray penetration. [96] Crucially, the magnitude of the observed cloud and aerosol responses suggests that the cosmic ray–cloud link could explain approximately 1 W/m² of solar cycle forcing. This estimate is consistent with crude calculations indicating that a 3% variation in cloud cover during an average 11-year solar cycle corresponds to a radiative forcing of 0.8 to 1.7 W/m². [96] Consequently, while the physical link appears robust, its global climatic significance requires further quantification.

6.3 Chamber Evidence Sky and Cloud

To move beyond statistical correlations and establish a physical basis for the cosmic-ray cloud hypothesis, researchers have turned to controlled laboratory environments that replicate the complex chemistry of the lower atmosphere. [228] The pivotal SKY experiment, conducted at the Danish National Space Center in Copenhagen, was designed to isolate the specific role of ionization in aerosol formation by using natural cosmic rays and gamma rays to simulate atmospheric ionization under conditions representative of Earth's atmosphere over the oceans. This experimental setup allowed scientists to introduce trace amounts of ozone, sulfur dioxide, and water vapor into an eight-cubic-meter reaction chamber, where ultraviolet light initiated photochemical reactions to produce sulfuric acid, a key precursor for cloud condensation nuclei. [50][229] By varying the ionization levels using cesium-137 gamma sources, the researchers could directly observe the response of aerosol concentrations to changes in ion density. [229]

Controlled chamber experiments provide the critical link between ionization and aerosol growth, moving beyond theoretical speculation to observable physical mechanisms. [219] The SKY experiment at the Danish National Space Institute established that electrons released by cosmic rays act as catalysts, accelerating the formation of stable sulphuric acid and water clusters. In these tests, researchers observed that without ionization, molecular clusters failed to grow sufficiently to provide significant numbers of cloud condensation nuclei larger than 50 nm in diameter. [223][229][60][50] However, when the air in the chamber was exposed to ionizing radiation to simulate the effect of cosmic rays, the clusters grew much more quickly to the sizes at which they help water droplets form and make clouds. This result contradicts earlier numerical modelling results, indicating that an important part of the ion-mechanism was missing from the theory. [229] The solution involves a so-far-ignored contribution to growth from the mass of the ions themselves. [219]

To isolate the microphysical mechanism linking cosmic rays to cloud formation, researchers moved from observational correlations to controlled laboratory settings. [228] This experimental design allows for the isolation of ionization effects from other atmospheric variables. [219] The results from these chambers demonstrate that ion-induced nucleation occurs under near-tropospheric conditions, confirming that ions facilitate the initial formation of small aerosols from trace gases like sulfuric acid. [223] By increasing ionization, the number density of nucleated aerosols increases, providing a direct physical link between cosmic ray flux and aerosol production. [219] This confirms the viability of the ion-aerosol clear-air mechanism, showing that cosmic rays can indeed seed the particles necessary for cloud droplet formation, thereby validating the core premise of the Svensmark hypothesis in a controlled environment. However, the magnitude of this effect in the real atmosphere remains uncertain, as laboratory conditions may not fully capture the complexity of natural aerosol processing. [96][60] Consequently, while the mechanism is physically plausible, its climatic significance is still debated.

To bridge the gap between cosmic-ray ionization and cloud formation, researchers turned to controlled laboratory settings. [228] While these experiments establish the initial nucleation step, the path to cloud condensation nuclei (CCN) remains complex. [229] However, state-of-the-art aerosol simulations suggested otherwise, indicating that additional aerosols create competition for available gases. This competition results in slower growth and a higher probability that a small aerosol becomes incorporated into a larger one before reaching CCN size, challenging the direct link between nucleation and cloud droplet formation. [229] In controlled settings where ultraviolet light generates aerosols from trace amounts of ozone, sulfur dioxide, and water vapor, researchers observed that ionization by gamma sources consistently increased aerosol production. [229] This relative increase remained constant from the initial nucleation stage through to diameters larger than 50 nm, a size range appropriate for cloud condensation nuclei. [229] This unpredicted experimental outcome points to a process not included in current theoretical models, possibly involving an ion-induced formation of sulfuric acid in small clusters. [229] By demonstrating that ions facilitate the growth of particles into the cloud-condensing size regime, the SKY data supports the mechanism by which galactic cosmic rays could modulate cloud cover and, consequently, global surface temperature. [228] These models suggested that additional aerosols create competition for available gases, slowing growth and increasing the likelihood that small particles are incorporated into larger ones before reaching CCN size. [229] These controlled experiments show that ions can seed the formation of aerosol particles, which are essential precursors for cloud condensation nuclei. [219] However, the path from these initial nucleation events to the formation of observable cloud droplets remains an area of active research, with open questions regarding the efficiency of this process in the real atmosphere. The consistency across different cloud records suggests that the correlation is not merely an artifact of data persistence, but the precise causal link remains contested. [96] Consequently, while the chamber experiments confirm the microphysical possibility of ion-induced nucleation, the translation of this effect into a dominant climate forcing mechanism is not yet settled. The debate centers on whether the observed correlations in satellite records are robust enough to support the hypothesis that galactic cosmic rays play a significant role in modulating global cloud cover and, by extension, surface temperature. [96]

6.4 Heliospheric Modulation and Global Temperature

The relationship between solar activity and global surface temperature is not merely a matter of direct irradiance but involves complex modulation mechanisms that amplify the Sun's influence on Earth's climate system. [230] While Total Solar Irradiance (TSI) varies only slightly over the solar cycle, its impact on surface temperatures appears to be significantly enhanced by other factors, particularly those linked to cosmic rays and cloud formation. [60] The evidence thus points to a more nuanced understanding of solar-climate interactions, where the Sun's magnetic activity and its effect on cosmic rays are key drivers of surface temperature variability. [96] In these records, solar changes lead temperature anomalies, a pattern consistent with both climate modeling and other climate and solar variability studies. [1] The climatic effect of the de Vries solar cycle is thus well established across multiple paleoclimate archives, including Central Asian ice-cores, Asian and South American monsoon-record speleothems, Mesoamerican lake-sediment cores used as drought proxies, and Alpine glaciers. [1] These diverse datasets collectively support the existence of a significant delay between solar forcing and terrestrial thermal response. [1] A delay of approximately 11 years exists between changes in Total Solar Irradiance and corresponding changes in surface temperatures. This finding further implies that the observed lag may reflect complex atmospheric or oceanic feedback processes rather than a simple radiative response. [8] The basic evidence supports a picture where temporal correlations link expected spiral arm crossings, variable cosmic-ray flux observed in iron meteorites, and the appearance of ice ages. [202] These temporal correlations support a picture in which climate on Earth is affected by our changing location in the Milky Way, by way of a variable cosmic-ray flux, with the basic evidence supporting relations between expected spiral arm crossing, variable CRF observed in iron meteorites, and the appearance of ice ages on Earth. [202] The data confirms that Greenland's interior ice sheet experienced a growth trend starting as far back as 1992, gaining mass by a net 11 billion tons per year plus or minus three billion tons per year, according to Dr. [46] H. Jay Zwally et al. in a 2005 article in the journal Glaciology. [46]

The mid-century cooling trend, specifically the global cooling from 1945 to 1977, occurred during a period of increasing post-1945 CO2 emissions. This divergence demonstrates that rising greenhouse gas concentrations were not the dominant driver of surface temperatures during this interval. [8] The coincidence of two warming periods in this oscillation with the Modern Solar Maximum suggests that natural forcing and internal variability made a significant contribution to observed warming. [1] Consequently, the natural contribution to observed warming should come at the expense of considerably reducing the

anthropogenic contribution. Furthermore, there is very solid evidence that periods of low solar activity in the past, identified by a higher rate of cosmogenic isotopes production such as ^{14}C and ^{10}Be, have a high degree of correlation with periods of climate deterioration manifested mainly as temperature decrease and precipitation changes. 2500-yr Bray cycle, with comparison of climate and solar variability records leading to the important observation that the period of the cycle correlates with the amplitude of the climate effect observed. [1] In general, the longer the cycle period, the more profound effect it appears to have on climate. [1]

6.5 Shaviv and the Spiral Arm Record

The long-term climate record of the Phanerozoic eon reveals a pattern of alternating cool and warm intervals rather than a unidirectional trend, a variability that spans the last 570 million years. [1] 150-Myr periodicity, a pattern first identified by G.E. [1]

Reconstructions of local supernova rates over the past 500 Myr, derived from open cluster ages and trajectories, demonstrate that cosmic ray flux variations on million-year timescales are determined by the local galactic environment rather than solar activity. Monte Carlo simulations combining open cluster dynamics with stellar evolution reveal that nearby supernovae cause significant spikes in Galactic cosmic ray flux, inducing atmospheric ionization changes larger than those caused by solar activity. [213][202]

The alignment between galactic structure and Earth's climate history suggests a deep connection between cosmic-ray flux and long-term glaciation. [202] This periodicity excludes random phenomena for glaciation appearance with high statistical significance, supporting the hypothesis that galactic environment drives Earth's ice age epochs. [202]

The Phanerozoic temperature record displays a c. [1] 150-Myr periodicity, a pattern first reported by G.E. [1] However, the spiral-arm climate hypothesis remains controversial because the solar system's past path, speed, and the position of the galactic arms in the distant past are not well constrained.

On geological timescales exceeding a million years, cosmic-ray variations are determined by the local galactic environment, with density expected to be higher when Earth resides within dense galactic spiral arms. [202] However, interpreting this correlation is not straightforward, as it assumes the constancy of other drivers and climate type throughout millions of years. During the Phanerozoic period, cold glacial periods coincided with high local supernova frequency and high cosmic rays, while warm climates appeared when the flux was low. [231] The CRF record exhibits a clear variability signal with a periodicity of 143±10 Myr, which is consistent in phase with the predicted CR diffusion model incorporating spiral arms. [232] The concentration of trace elements in pyrite serves as a proxy for nutrient availability in the oceans, correlating closely with cosmic ray changes throughout the Phanerozoic. [231] Since nutrients such as phosphorus are fundamental limiting factors for biological systems, the energy flow through biological systems is constrained by these cosmic-driven climatic shifts. [231] The results depicted in the relevant studies are consistent with the hypothesis that this chain of causality—supernovae to climate to nutrient flow to bioproductivity—holds true over millions of years. [231] Furthermore, the periodicity of ice age epochs aligns with a cosmic ray flux record showing a variability signal of approximately 143 ± 10 Myr, which agrees in phase with the predicted cosmic ray diffusion model incorporating the Milky Way's spiral arms. This agreement provides a qualitative link pointing to cosmic rays as a driver of climatic variability. [233] Thus, the long-timescale climate sensitivity question is addressed by the persistent influence of galactic cosmic rays on Earth's biosphere and climate, supporting the view that cosmic ray modulation is a primary factor in global temperature and productivity fluctuations.

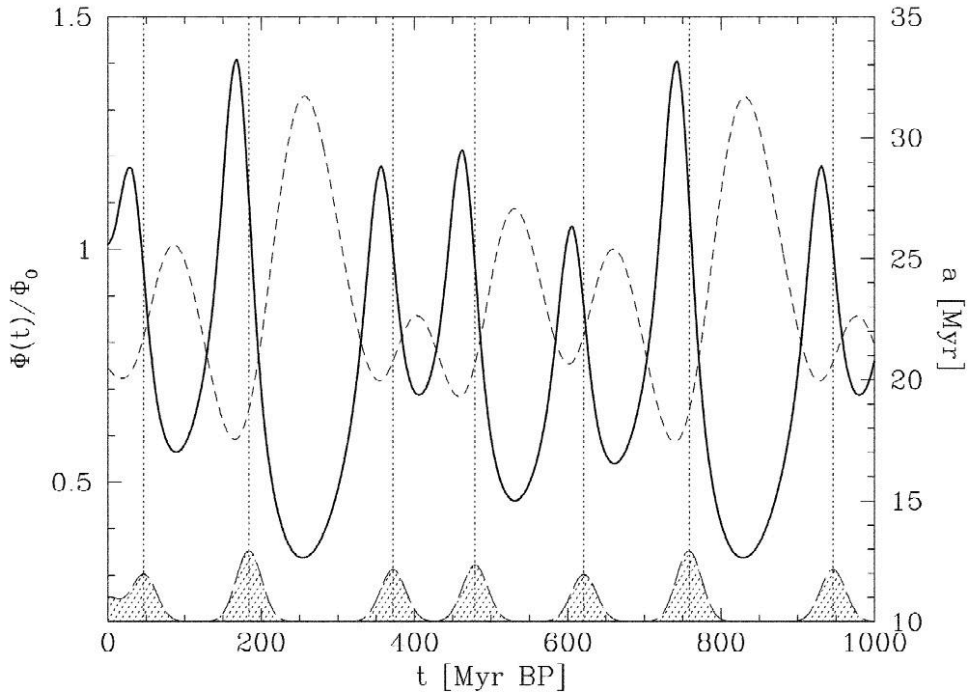

Figure 6.2: The plot shows the cosmic-ray flux ($\Phi(t)/\Phi_0$, solid line) and cosmic-ray age (a, in Myr, dashed line) as functions of time (t, in Myr BP) for a diffusion coefficient D = 10^{28} cm²/s and a scale height l_H = 2 kpc. The flux exhibits periodic peaks that are phase-lagged behind the spiral arm crossings, which are indicated by vertical dashed lines and correspond to the locations of spiral arms defined by the Taylor and Cordes free electron density model. The shaded regions at the bottom represent the relative amplitude and width of these spiral arms, and the flux distribution is skewed toward later times, consistent with a delay between supernova explosions and the subsequent propagation of cosmic rays through the interstellar medium. (source: ref 202)

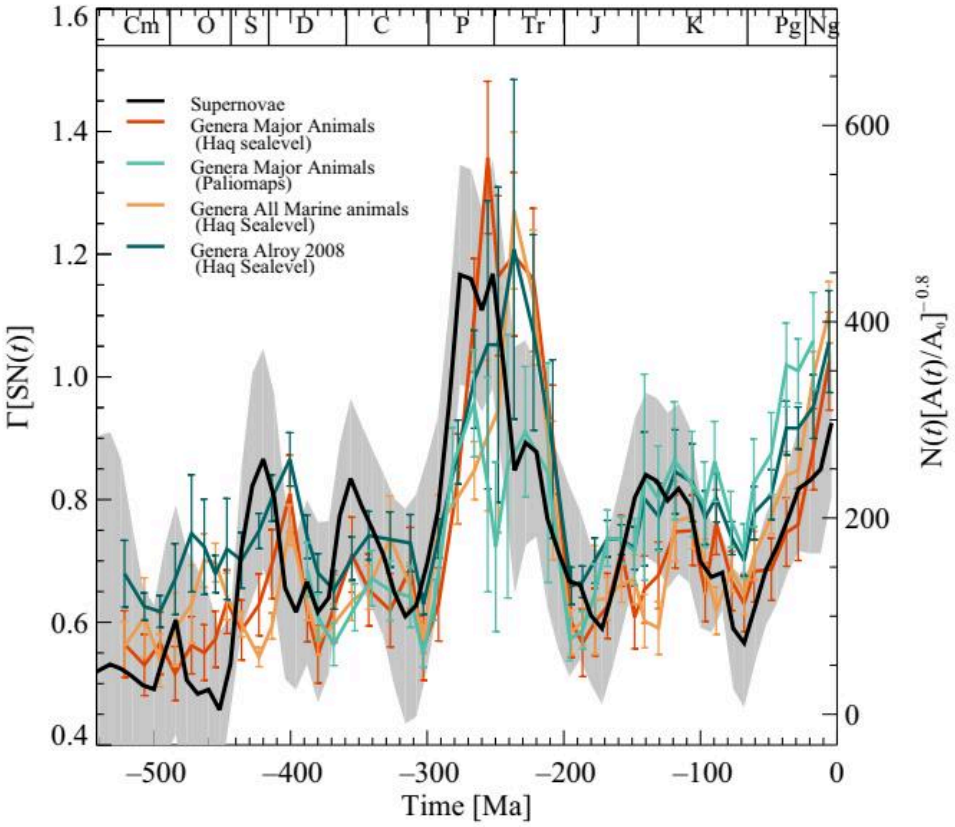

Figure 6.3: The figure displays a time-series comparison of supernova rate variations and marine animal diversity over the past 500 million years. The black curve, representing supernova activity, is derived from Equation (4) and shows fluctuations with a gray shaded region indicating 1-σ uncertainty from Monte Carlo simulation. Multiple curves depict marine animal diversity: orange and teal lines show major marine animal genera normalized to shallow marine margin area using data from Haq et al. and Haq & Schutter, and Cao et al., respectively; a dark green line represents the genera-level diversity of marine invertebrates from Alroy et al.; and another dark green line shows all marine animals normalized to shallow marine area using Haq et al. and Haq & Schutter. Error bars on the genera curves reflect minimum 1-σ uncertainty due to unavailable area estimates. The data suggest a correlation between supernova activity and marine biodiversity trends, particularly during major extinction and diversification events. (source: ref 231)

7. The Underground Connection: Volcanism and the Sun

Grand minima have coincided with anomalously intense volcanism; plausible mechanisms — lithospheric stress, isostatic rebound, deep-Earth degassing — are testable and matter for the coming minimum.

7.1 When the Sun Goes Quiet the Earth Gets Loud

By analyzing carbon-14 derived from tree rings and beryllium-10 extracted from Greenland and Antarctic ice cores, researchers have established that solar activity exhibits long-term variability, including periods of significantly reduced activity known as grand minima. These isotopic archives serve as proxies for cosmic-ray flux, which increases when the Sun's magnetic shielding weakens during quiet phases. [52][45][45][234][61] This increased cosmic-ray flux is not merely a theoretical construct but a measurable phenomenon captured in geological archives, providing a baseline for understanding solar-climate interactions. [235] The consistency of these signals across different isotopes and geographic locations suggests that regional anomalies are not the primary driver, indicating that the observed variations are global in scale and linked to solar modulation. [231] The Maunder Minimum, for instance, is characterized by a distinct lack of visible sunspots and a corresponding spike in radionuclide production, offering a signature of reduced solar activity. [43]

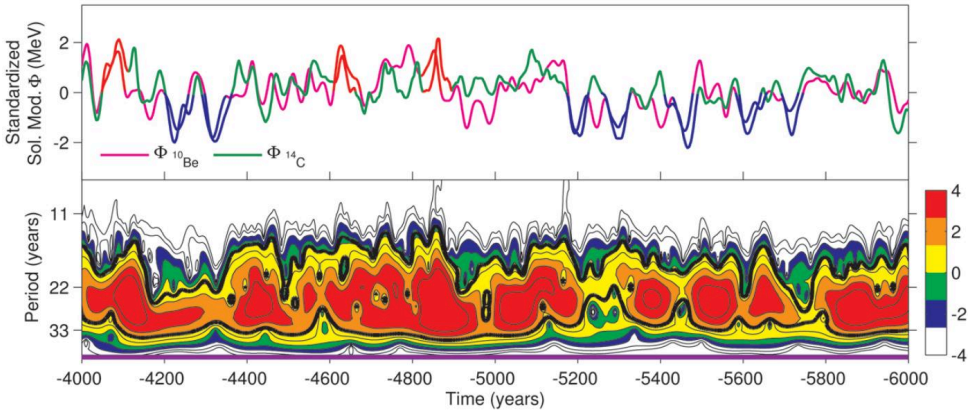

Figure 7.1: The image displays two panels: the top panel shows standardized solar modulation potential time series for cosmogenic isotopes ^{10}Be (pink line) and ^{14}C (green line), with blue and red lines indicating identified grand minima and maxima, respectively. The bottom panel presents a local cross-wavelet spectrum of high-pass filtered ^{10}Be and ^{14}C data, with a cutoff frequency of 1/30 year^{-1}, highlighting periods of strong coherence between the two proxies during identified grand minima; the color scale indicates wavelet power, and the purple line marks dates in BC. (source: ref 156)

Holocene reconstructions indicate that grand minima are not periodic but appear as the result of chaotic or stochastic processes within clusters separated by 2000–2500 years. Analysis of radiocarbon data reveals a weak, marginally significant quasi-periodicity of 2000–2400 years, a well-known period in ^{14}C records that likely relates to the clustering of grand minima rather than to a long-term modulation of solar activity. [32][1][147][200] This pattern suggests that the occurrence of grand minima and maxima is defined by stochastic or chaotic processes, with no clear periodicities observed in the occurrence of grand maxima. [236] The observed effect of the 2500-year Bray solar cycle is to result in long Spörer-type solar grand minima or clusters of such minima at its lows. [200] These climatic shifts, registered mainly as significant reductions in winter temperatures and increases in precipitation in the North Atlantic region, have historically coincided with societal disruptions, including food crises and population decreases. [200]

The biological and temperature subdivisions of the Holocene display transitions related to the lows of the Bray cycle, suggesting that climate-related disruptions have been quasi-periodic drivers of societal change. [200] Thus, while the timing of individual grand minima may be stochastic, their clustering within the broader 2000–2500 year cycle provides a structural framework for understanding long-term solar variability and its associated climatic impacts.

Reconstructions of solar activity during the Holocene period, spanning from 10,000 B.C. to the present, reveal that the Sun exhibits great variability in the strength of each solar cycle. [1] While some cycles produce a high number of sunspots, others result in low numbers, leading to distinct epochs of suppressed activity known as solar Grand Minima. [237] A solar Grand Minima is defined as a period when the (smoothed) sunspot number is less than 15 during at least two consecutive decades. [236] Detailed analysis of these reconstructions shows that the Sun spends about 17 percent of the time in a Grand Minima state. This finding suggests that grand minima are not rare anomalies but a recurring feature of solar behavior over the past ten millennia. [104][1] In contrast, energetic solar Grand Maxima states are typically short-lived, lasting in the order of 50 years.

The sunspot number records establish a solar quasi-period of 90 ± 10 years, known as the Wolf-Gleissberg cycle, as the most prominent of the longer solar cycles. This periodicity is supported by wavelet power spectrum analysis of sunspot data from 1700 to 2020, which yields a mean total wavelet period of Tsa = 4*22.5 = 90.0 years. [237][204][19][238] Fast Fourier Transform (FFT) computations on the full sunspot number time series, including subsets of the first half, second half, and middle half, reveal that the 87.6-year Gleissberg peak is sharp and prevalent across all intervals, although it is absent in recent data. [115] While earlier hypotheses, such as those by Stothers, suggested an 11-year periodicity in volcanic activity, recent analyses of 3,829 eruptions with a Volcanic Explosivity Index (VEI) of 2 or greater reveal a dominant 22-year period that aligns with the solar background magnetic field (SBMF) cycle. [238] Specifically, the evidence suggests that more volcanic eruptions occur during the maximum phases of the doubled solar cycles when the solar background magnetic field possesses a southern polarity. [170] This correlation is not uniform across all historical periods; a rather high positive correlation between the number of volcanic eruptions and the southern polarity of the SBMF was established for the period 1868–1950, whereas a much smaller negative correlation was observed during 1750–1868. [11] The proposed link involves increased electromagnetic interaction between the SBMF and the terrestrial magnetic field, causing geomagnetic disturbances that can lead to shifts of the crusts, most powerful earthquakes, and volcanic eruptions. [239] The reduced correlation between volcanic eruptions and solar activity indices recorded during the period 1750–1868 can be associated with a geomagnetic jerk and the related migration of the North pole towards lower latitudes. [239] Differences in eruption frequencies over the phases of solar cycles may also relate to differences in solar activity indices defined by sunspots and eigen vectors of magnetic fields related to different types of solar magnetic fields, specifically the toroidal and poloidal fields. [170] The lack of correlation in the period 1950–1980 is linked to open air nuclear bomb testings that distorted the effects of the solar magnetic field. [170] In summary, the increase of volcanic eruptions established during solar cycles with the southern polarity of the SBMF emphasizes the importance of solar-terrestrial interaction in volcanic eruptions. [238] Hence, despite links between volcano occurrences and solar activity not being clear yet, the consequences of volcanic eruptions for the terrestrial atmosphere during cycle 26 with the southern polarity of the solar magnetic field can be expected to be noticeable during the modern Grand Solar Minimum (2020–2053).

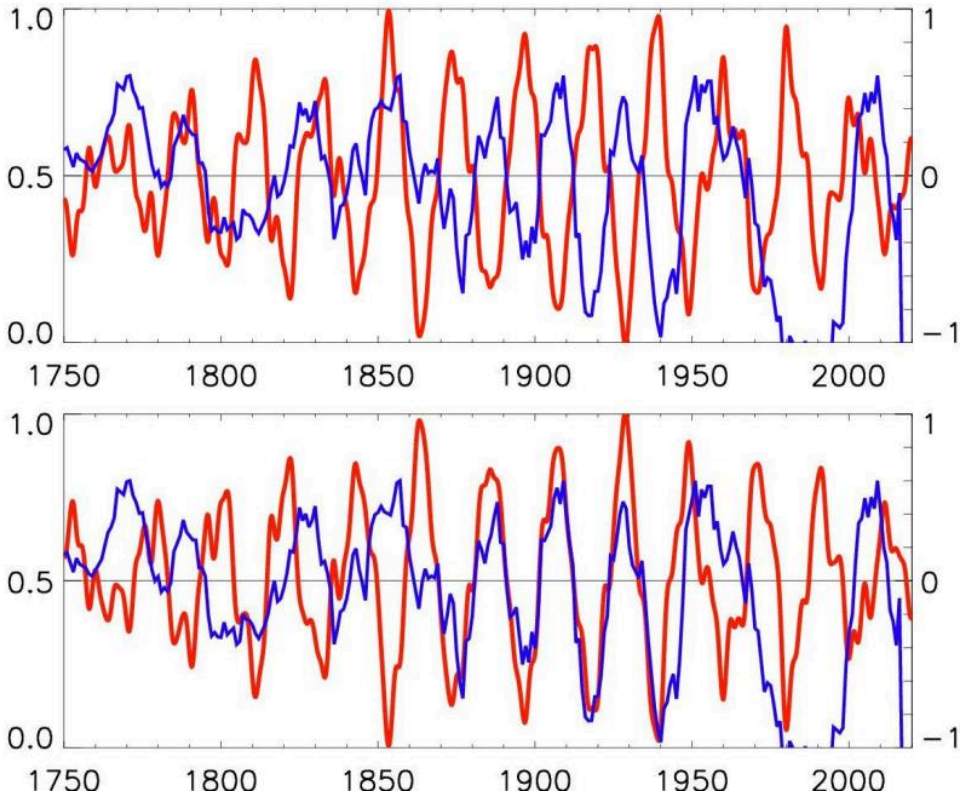

Figure 7.2: The figure displays two time-series plots from 1750 to 2000, comparing the normalized number of volcanic eruptions (blue curves, left y-axis) with the normalized eigen vectors of the solar background magnetic field (red curves, right y-axis). The top plot shows the eruption count versus the summary eigen vector curve, where positive values indicate northern polarity and negative values indicate southern polarity of the solar magnetic field. The bottom plot presents the same eruption data against an inverted eigen vector curve, with positive values corresponding to southern polarity and negative to northern polarity. Both plots exhibit correlated oscillatory patterns, suggesting a potential relationship between solar magnetic field dynamics and volcanic activity, with correlation coefficients detailed in the text and Figure 7. (source: ref 11)

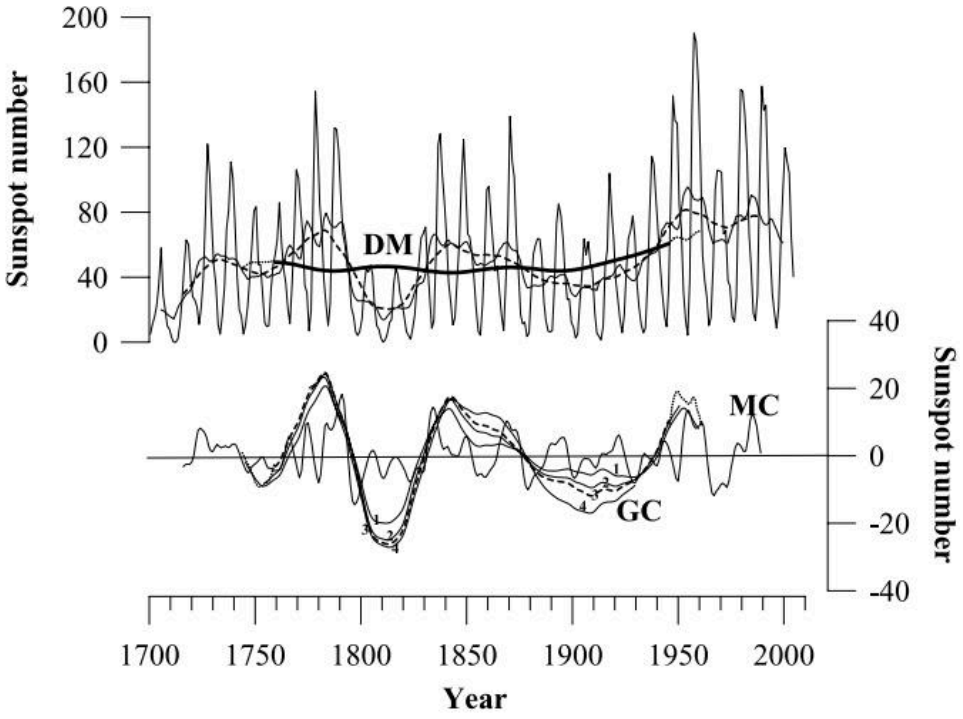

Figure 7.3: The figure displays two panels analyzing sunspot number data from 1700 to 2000. The top panel shows the raw sunspot number time series (thin curve) alongside successive running averages: an 11-year average (thick curve), a 22-year average (dashed curve), and an 88-year average (short, thick curve), with a dotted extension of the R88 signal; the Dalton Minimum (DM) is marked. The bottom panel presents filtered signals of the Hale cycle (solid curve, MC) and the Gleissberg cycle (dashed curve, GC), with a dotted extension of the GC signal, illustrating long-term oscillations in solar activity. (source: ref 128)

7.2 The Maunder Era Eruptions

This event, which began on February 19 and continued until mid-March, stands out as the largest historical explosive event in the Andes, classified as VEI 6. The eruption's magnitude is confirmed by the correlation of geologic evidence with early Spanish chronicles, which document a sustained Plinian column reaching 27–35 km in height and delivering a dacitic pumice fall with a dense rock equivalent volume of 3.1 km^3. [240][241][242][243] Ash fall was reported 200–500 km away in south Peru, west Bolivia, and north Chile, while strong winds carried fine ash more than 500 km to the west and into the Pacific Ocean. [240] The onset of this high-discharge eruption was fueled by the disruption of an active hydrothermal system enclosed in the pre-AD 1600 amphitheater, with computed volumetric eruption rates between 5.4–6.6 × 10^4 and 1 × 10^5 m^3/s. [240] The preservation of tephra-fall deposits in the arid and semi-arid environments of the Central Andes provides a critical archive for understanding the dispersal and impact of these massive explosive events. [241] From 260 thickness measurements of the plinian pumice fall made over an area of approximately 95,000 km^2, they surmised a reconstructed 7.87-km^3 bulk volume of the plinian pumice-fall deposit. [240] This figure was considered potentially underestimated beyond the 1-cm-isopach. [240] Adding the volume of post-plinian tephra to that of the plinian pumice fall led to a total bulk volume of 11.4–12.1 km^3. [240] The chemical composition of glass in juvenile tephra was also examined, linking it to glass in the Antarctic ice. [244]

The chemical characteristics of juvenile tephra from the AD 1600 Huaynaputina eruption allow a firm cause–effect link to be established with glass found in Antarctic ice, improving estimates of stratospheric loading. [244]

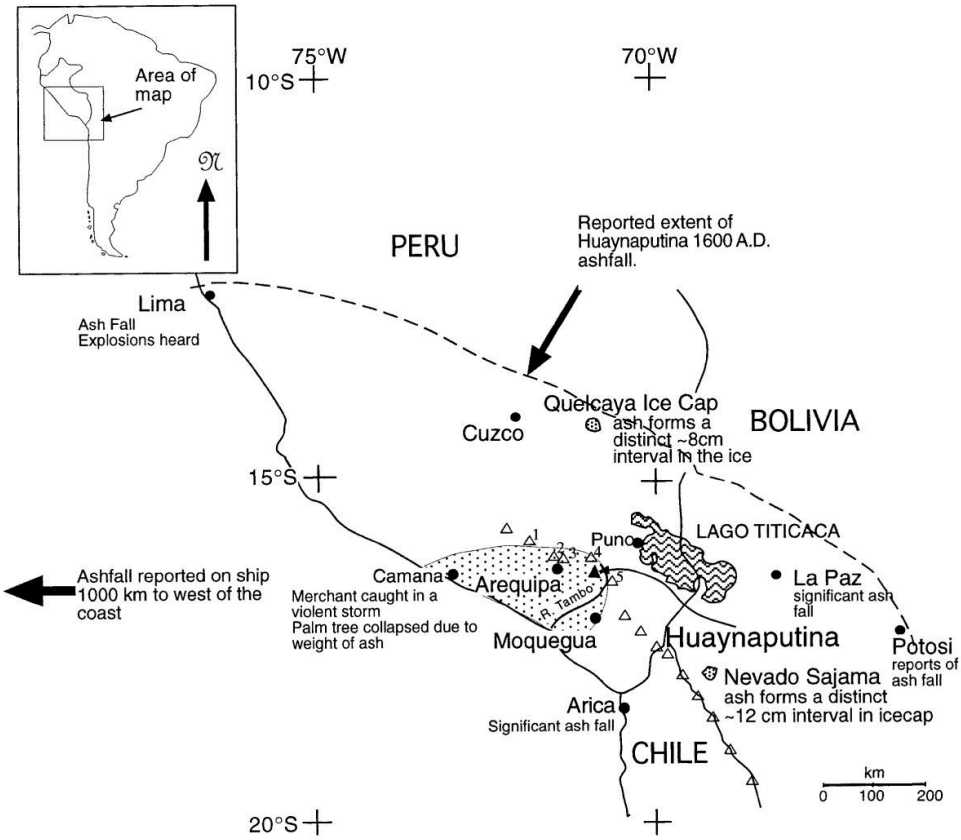

Figure 7.4: This map illustrates the regional context of Volcán Huaynaputina in southern Peru, showing the extent of its 1600 A.D. ashfall across Peru, Bolivia, and northern Chile. It highlights the distribution of volcanic ash deposits, including the stage-I pumice fall (stippled area) dispersed primarily west-southwest, and identifies key locations with ashfall evidence such as ice cap layers in the Queucaya and Nevado Sajama ice caps, historic reports from Lima and Potosí, and a ship log recording ashfall 1,000 km west of the coast. The map also marks active volcanoes in the Central Volcanic Zone, including Sabancaya, Chachani, Misti, Ubinas, and Ticsani. (source: ref 170)

The AD1600 eruption of Huaynaputina in southern Peru stands as one of the largest explosive events in historic times, with tephra deposits and juvenile glass chemistry establishing a firm cause–effect link to acidity spikes in Antarctic ice. [244] This stratospheric loading suggests statistically significant global cooling, consistent with the severe climatic anomalies recorded across multiple proxy datasets in the immediate aftermath. [244] Tree-ring chronologies from the Swiss and Austrian Alps, along with maximum latewood density data from thirteen sites along the northern tree line of North America, indicate extremely low temperatures in 1601 AD. [245] Significant frost and light rings identified in western USA, near Bush Lake in Canada, and in the Polar Urals further support this widespread cooling signal. [246] Historical records corroborate these biological proxies, noting an unusually cold summer in England and Italy, a severe winter in Russia, Latvia, and Estonia, and widespread crop failures in northern China due to killing frost. [245]

The ecological aftermath of the AD 1600 Huaynaputina eruption provides a precise chronometer for studying rapid biological colonization in the northern Atacama desert. [247] On the deep pumice substrates near Omate, Moquegua, Peru, floristic inventories demonstrate that approximately 59 angiosperm species established themselves within the last 400 years. This unique vegetation type, dominated by therophytes and chamaephytes, exhibits a floristic composition with the highest similarity to the coastal Lomas de Tacna rather than geographically closer Sierra formations, despite stark climatic differences. [247][248] The presence of nine species representing highly disjunct populations, with nearest living relatives located 200 to over 700 km away, confirms that long-distance dispersal events were the primary colonization mechanism on the denuded substrate. [247] Morphological analysis further establishes that four taxa have undergone considerable divergence from their source populations, with two potentially representing neoendemics, proving that speciation can occur rapidly on suitable target areas. [247] These

findings highlight how the specific edaphic and climatic filters of the Omate pumice slopes precluded establishment from adjoining habitats while allowing successful colonization from remote source areas, offering insights into the speed of phyto-diversity processes following major explosive volcanic events. [247]

The ecological aftermath of the 1600 AD Huaynaputina eruption provides a unique natural laboratory for studying rapid colonization on deep pumice substrates in the northern Atacama desert. [247] Research into the vascular plants establishing themselves on the Huaynaputina pumice slopes near Omate, Moquegua, Peru, reveals a distinct floristic composition that has developed over the last 400 years. [247] Floristic composition on Huaynaputina slopes shows highest similarity to the coastal Lomas de Tacna rather than geographically closer Sierra formations. This finding is quantified by a Sørensen index of 24 at the species level between the Omate sites and the Lomas de Tacna, a similarity nearly twice that of any other compared sites. [247][247] The porous pumice absorbs precipitation only in upper layers, keeping subsoil dry year-round, which mimics the climatic constraints of the coastal Lomas rather than the moisture-retaining Sierra soils. [247] Consequently, the Lomas vegetation serves as the natural recruiting ground for this unique Andean vegetation type, despite the significant altitudinal and geographical barriers. This strong ecological link demonstrates how specific substrate properties can override proximity in determining post-eruption flora, highlighting the role of long-distance dispersal mechanisms in repopulating denuded volcanic landscapes. [248] Crucially, nine species on these slopes represent highly disjunct populations, with their nearest known living populations located 200 to greater than 700 kilometers away in central Peru, Chile, Bolivia, or Argentina. These disjunctions suggest recent long-distance dispersal as the primary colonization mechanism, given that the substrate was denuded in 1600 AD. [247] Abiotic conditions, including soil type and climate, appear to limit establishment from neighboring vegetation. [247] Morphological analysis reveals that four taxa exhibit clear differences from populations elsewhere, with two potentially representing neoendemics, indicating rapid morphological divergence over the 400-year period. [247] Rodent midden data suggest no dramatic late Holocene climatic changes since 1600 AD, though a strong El Niño event in 1652 AD may have facilitated Lomas flora expansion and subsequent dispersal to Omate. [247] This young, annual-dominated community contrasts with the shrub-dominated flora on adjacent rocky soils, identifying the Omate pumice slopes as the first recorded Andean vegetation type dominated by annuals and floristically akin to coastal Lomas. This unique assemblage likely reflects a specific post-eruption colonization trajectory rather than a stable equilibrium state. [247] Consequently, the site serves as a critical natural experiment for understanding rapid ecological succession in extreme volcanic environments.

7.3 Tambora and the Year Without a Summer

The April 1815 eruption of Mount Tambora stands as a defining event in the instrumental record, classified at an intensity of 7 on the volcanic explosivity index, a relative measure of volcanic explosiveness that ranges from 0 to 8. [249] This aerosol umbrella, six times the size of Mount Pinatubo's 1991 cloud, disrupted normal patterns of temperature and precipitation across the hemispheres by entering the meridional currents of the global climate system. [77] The subsequent year of 1816 has been termed the "Year Without a Summer," a period marked by significant climate anomalies and harvest failures across Europe and North America. [250] The dust veil increased visual extinction in the stratosphere by 1.4 ± 0.2 mag at northern middle latitudes, implying a worldwide stratospheric aerosol load of ~2.0 × 10^14 g, in near agreement with values estimated from Greenland ice acidities. [74] The relation between volcanism and climate depends on eruptive scale, with volcanic ejecta and gases penetrating high enough to reach the stratosphere where sulfate aerosols form and spread aloft by winds and meridional currents. [77] The telltale sulfate imprint left on the ice for paleoclimatologists to discover more than a century and a half later confirms the global reach of this atmospheric perturbation. [251]

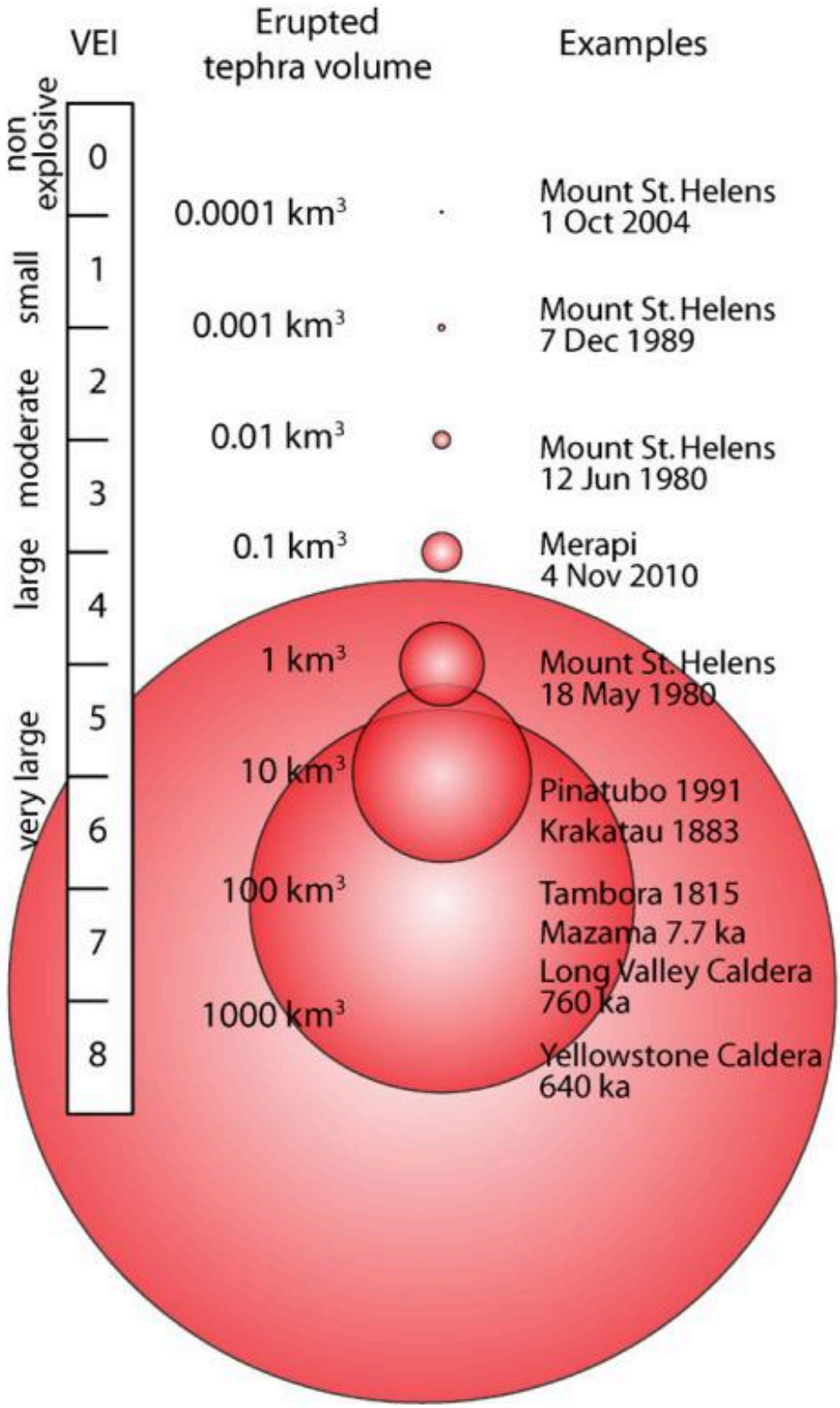

Figure 7.5: The image displays a logarithmic scale of the Volcanic Explosivity Index (VEI), illustrating the relationship between eruption magnitude and erupted tephra volume in cubic kilometers. It uses a series of concentric circles to represent increasing volumes from 0.0001 km³ to 1000 km³, with each circle corresponding to a VEI level from 0 to 8. The chart includes examples of historical eruptions, such as Mount St. Helens at VEI 5 and the Yellowstone Caldera (640 ka) at VEI 8, showing how specific events map to their respective explosive magnitudes and volumes. (source: ref 256)

The 1815 eruption of Mt. Tambora discharged approximately 150 km³ of ash and pumice — about 50 km³ of dense-rock-equivalent magma, creating a dust veil that increased visual extinction by 1.4 ± 0.2 magnitudes at northern middle latitudes. [74] These stratospheric sulfate aerosols scattered incoming solar radiation, establishing a global cooling of approximately 0.4 to 0.8°C during 1815–1818. The climatic anomalies were particularly severe in eastern North America and central and western Europe, where persistently cold and wet weather defined the late spring and summer of 1816. [252][74][70] This period, known as the "Year Without A Summer," caused significant socio-economic impacts, including severe famine, and was perceived by contemporary populations as a catastrophic event. [253] While the Dalton Minimum contributed a small additional cooling effect, the primary driver was the volcanic forcing. [79] The magnitude of Tambora's impact, exceeding any other known eruption in the past 10,000 years, provides a high-accuracy calibration standard for investigating earlier explosive volcanic events. [74] These conditions caused widespread crop failures, leading to famine and social distress compounded by the aftermath of the Napoleonic wars. [253] This cooling is further evidenced by climatic indicators such as late grape harvests in France and frost damage rings in trees in the western United States and South Africa. [70] The dot marks Geneva, located within a region of negative SLP anomaly. [254]

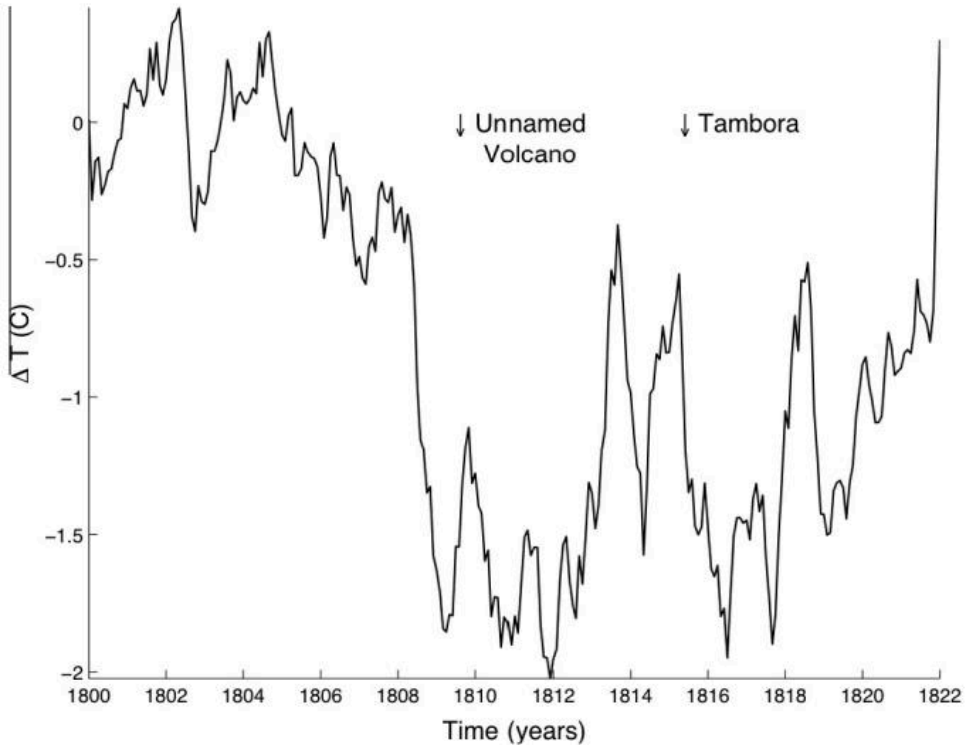

Figure 7.6: This line graph shows land temperature anomalies (ΔT in °C) from 1800 to 1822, based on data from the Berkeley Earth Project, illustrating the cooling during the Dalton (CGC) minimum. The plot reveals a significant temperature decline beginning in 1809, prior to the eruptions of the unnamed volcano and Tambora (marked by arrows), with the most pronounced cooling occurring around 1812. Temperature fluctuations of approximately 1.5 °C are evident between 1815 and 1820, highlighting the period's climatic instability. (source: ref 24)

The summer of 1816 in western Europe was cool and exceedingly wet, a condition that compounded the aftereffects of the Napoleonic Wars to produce famine, disease, and social unrest. [70] Data from Manley show that the summer months of 1816 in central England were about 1.5°C cooler than during the summer of 1815, while pressure anomaly charts reconstructed by Kelly et al are dominated by negative pressure anomalies over Europe beginning in early 1816. [70] This atmospheric shift led to a southward track for middle-latitude cyclones, creating a cold, wet summer centered over England and extending across much of western Europe. [77] In North America, records from Hudson's Bay Company posts on the eastern side of Hudson Bay indicate that the summers of 1816 and 1817 were the coldest in the modern record, a finding supported by tree-ring data from northern and western Quebec. [70] The summer of 1816 was the coldest in New Haven, Connecticut, for the entire period from 1780 to 1968. [250] Repeated

frosts in New England during late spring through summer caused severe crop failures, resulting in poor harvests and food shortages. [76] Indian corn in Pennsylvania rotted on the stock, frozen hard by the cold, while newspapers from England noted that 1816 was a year in which there was no summer. [39] These widespread crop failures, particularly of corn in America and grain in Europe, demonstrate the devastating impact of the 1816 climate anomalies. Consequently, the resulting socioeconomic disruptions appear to have been significantly exacerbated by these climatic conditions. [255][70][39][77]

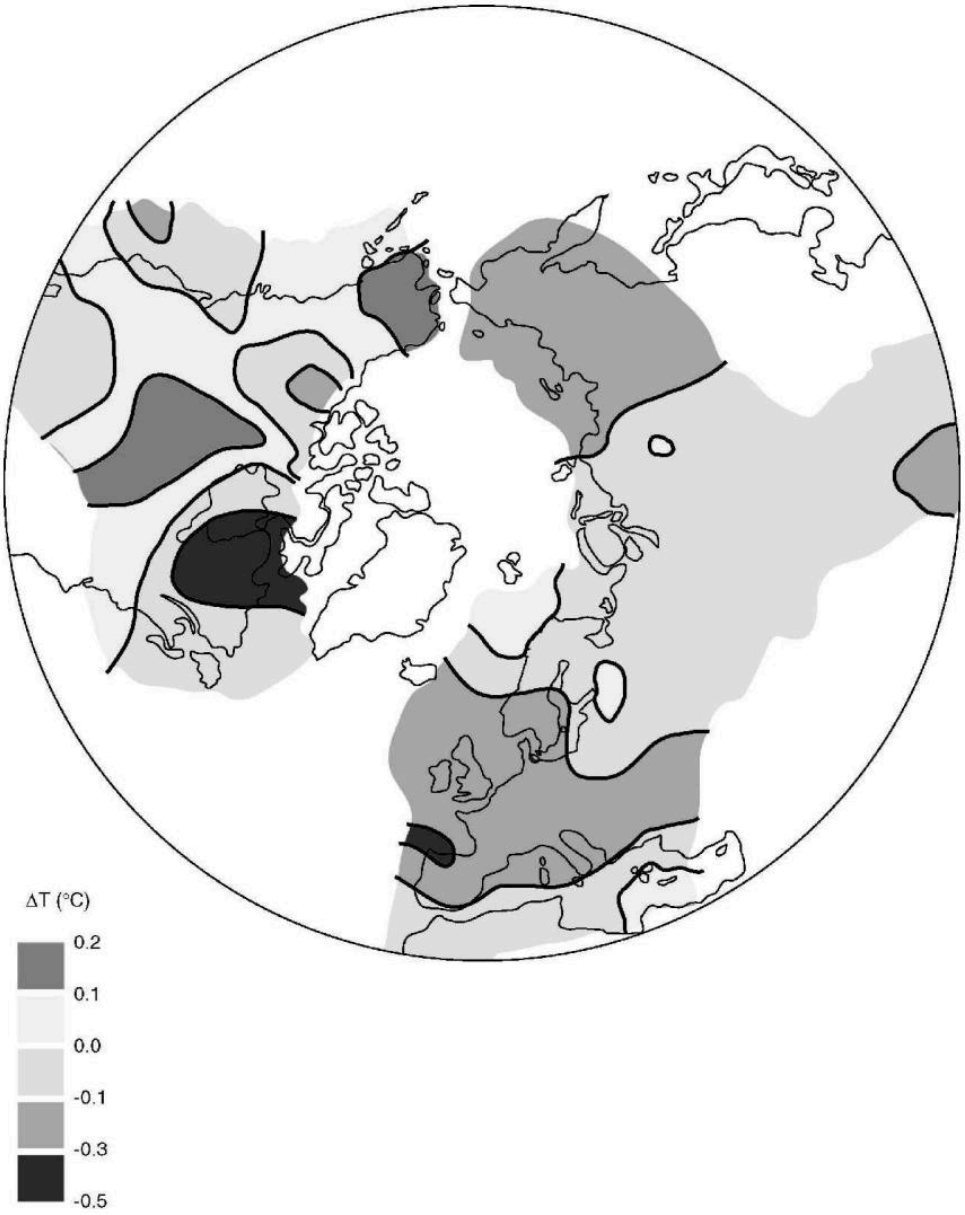

Figure 7.7: This figure displays a gridded map of reconstructed surface temperature anomalies (ΔT in °C) for summer 1816, derived from latewood density in tree rings across the Northern Hemisphere. The data, based on Briffa et al., shows widespread negative anomalies, with the most severe cooling (down to −0.5°C) concentrated over northern Europe and parts of Siberia, while milder cooling (around −0.1 to −0.3°C) extends across much of the continent and into North America. (source: ref 253)

The summer of 1816 in western Europe was cool and exceedingly wet, a condition that compounded the aftereffects of the Napoleonic Wars to produce famine, disease, and social unrest. [70] This period, referred to by Post as "The Last Great Subsistence Crisis in the Western World," saw negative pressure anomalies dominate Europe beginning in early 1816, leading to a southward shift in middle-latitude cyclone tracks. [70] Data from Manley indicate that the summer months of 1816 in central England were about 1.5°C

cooler than during the summer of 1815. [70] In North America, records from Hudson's Bay Company posts on the eastern side of Hudson Bay show that the summers of 1816 and 1817 were the coldest of any in the modern record, a finding supported by tree-ring data from northern and western Quebec. [70] Repeated frosts in New England caused crop failures, resulting in poor harvests and food shortages. [76] The resulting food insecurity and social distress following the 1816 harvest failures contributed to outbreaks of typhus and other diseases in Europe. [253] At the height of the typhus epidemic in September 1817, Dublin doctors warned of impending ruin, while the medical establishment in Edinburgh expressed alarm at the continued fever spreading across the British Isles. [77] This anomalous cooling followed the spectacular April 1815 eruption of Tambora volcano on Sumbawa Island in Indonesia, which ejected approximately 150 km^3 of ash and pumice, equivalent to about 50 km^3 of dense rock equivalent magma, into the atmosphere. [70] The eruption column reached an estimated 50 km into the stratosphere, dispersing ash over an area exceeding 4×10^5 km^2 and causing darkness for up to two days at distances of 600 km from the source. [70] However, the severity of the 1816 cooling cannot be attributed to Tambora alone. Crucially, European temperature measurements during the Dalton Minimum showed a decline in place well before the Tambora eruption, with the lowest temperatures recorded prior to 1816 according to the European temperature profile done by David Archibald in his work, The Past and Future Climate.

7.4 Hunga Tonga the Eruption That Warmed the World

The January 2022 eruption of the Hunga Tonga–Hunga Ha'apai volcano represents a singular event in the modern observational record, distinguished not by sulfur dioxide but by an unprecedented injection of water vapour into the stratosphere. Satellite observations from the NASA Aura satellite and balloon data collected by the National Oceanic and Atmospheric Administration (NOAA) near Reunion Island confirm that approximately 150 Tg of water vapour was blasted roughly 60 km into the air, increasing the existing global stratospheric burden by 10% — the largest stratospheric perturbation of water vapour observed in the satellite era, which spans more than 30 years.[257][258][259] While classic explosive eruptions like Pinatubo or Tambora are defined by their sulfate aerosol loads, which scatter sunlight and induce a temporary cooling effect, Hunga's primary radiative forcing agent was water. The immediate atmospheric response included strong cooling in the Southern Hemisphere mid-latitude stratosphere, which strengthened the mid-latitude jet and slowed the Brewer–Dobson Circulation, while simultaneously perturbing polar ozone chemistry through increased HOx and polar stratospheric cloud formation. Satellite records show the dark patch of high humidity spreading globally from the Southern Hemisphere to the north over the course of a year.

What made Hunga different was the ratio of water to sulfur. TROPOMI satellite-based measurements of SO_2 concentrations in the atmosphere establish that the total stratospheric SO_2 mass was approximately 0.4 Tg, a figure consistent with other estimates of ~0.5 Tg that confirm the eruption injected only a modest amount of sulfur dioxide.[260][259][261] This disparity is critical because SO_2 oxidizes into sulfate aerosols that reflect sunlight and cool the surface, whereas stratospheric water vapour acts as a greenhouse gas that warms it. Atmospheric physics demonstrates that stratospheric water vapour effectively alters radiative forcing and influences global surface temperature once it enters the stratosphere.[1][262][259][263][170] Consequently, the Hunga event produced a transient natural warming pulse rather than the classic volcanic winter associated with Pinatubo-type eruptions — a thermal anomaly that acted in direct opposition to the traditional volcanic winter narrative.

How long will the pulse last? In the first two years post-eruption, the stratospheric burden hardly changed, leaving the residence time of the volcanically injected water vapour uncertain, and early estimates varied widely — some projections suggested a return to baseline conditions as early as 2025, while others predicted a lingering presence for more than a decade. The Microwave Limb Sounder (MLS) instrument aboard NASA's Aura satellite, however, has provided continuous, high-resolution observations of the Hunga-enhanced water since the eruption, and recent data show a substantial decline from 2024 to early 2025, marking the largest drop since the event. Comparison with 3-D numerical model simulations demonstrates that the long-term removal of the Hunga water has entered a new phase, with stratosphere-troposphere exchange playing an increasingly important role, exceeding Antarctic dehydration in 2024. The primary sinks for this excess water include ice polar stratospheric cloud sedimentation and stratosphere-to-troposphere transport in middle-to-high latitudes, with additional minor loss in the mesosphere due to photolysis. The additional stratospheric water vapour is now decaying steadily with an e-folding time of 3 years, a trajectory that will bring the perturbation back within the observed pre-Hunga range of variability around 2030 — quantifying the residence time of the Hunga stratospheric water vapour perturbation at 9 years.[259] The decay estimate is statistically well-constrained: combining the formal

fitting uncertainty of the exponential fit to the MLS time series through July 2025 with the spread arising from natural variability yields a total two-sigma uncertainty of roughly 0.29 years.

This transient natural warming pulse contributed to the global temperature surge observed in 2023 and 2024, challenging narratives that attribute recent heat solely to anthropogenic carbon dioxide. Unlike the persistent cooling shadow cast by sulfate aerosols, which can linger for years and mask underlying solar trends, the radiative impact of stratospheric water vapour is inherently temporary, governed by the atmospheric residence time of the molecule itself. As the vapour dissipates toward 2030, the radiative forcing will wane, allowing the underlying climate drivers — solar irradiance and cosmic-ray modulation among them — to reassert their influence on global surface temperatures. Understanding the timeline of this decay is critical for disentangling natural variability from long-term climate trends, particularly in assessing the compounding effects of solar minima and volcanic activity.

7.5 Mechanisms Why Might the Sun Affect the Earth S Crust

In the 1970s, John Eddy noticed a correlation between solar activity and the European climate over the previous millennium, observing that the Little Ice Age (1300–1850 AD) was a cold period that took place while the Sun was particularly inactive, whereas the Medieval Warm Period (1000–1200 AD) occurred while the Sun was active. [60] A new reconstruction of temperature variability in the extratropical Northern Hemisphere during the last two millennia correlates reasonably well with the assumed low-frequency variability in solar forcing of the last millennium, revealing that several periods with especially low solar activity are visible in the reconstruction, including the Wolf Minimum (c. [2] AD 1645–1715). Figure 5a shows recent reconstructions of temperature variation over the last 1000 years, while Figure 5b displays cosmic ray reconstructions based on ice cores from Antarctica and an ice core from Greenland, demonstrating a remarkable correlation between the changes in temperature and changes in cosmic rays caused by solar activity. [60] Historical data associate the European Maunder Minimum winter cooling with enhanced northeasterly advection of continental air, consistent with an anomalous negative NAO, and reconstructions of large-scale surface temperature patterns from networks of diverse proxy information, such as tree rings, ice cores, corals, and historical records, provide empirical estimates of the large-scale climate response to solar forcing. [264] When filtered to isolate the multidecadal-to-centennial time scales associated with the Maunder Minimum, the empirical regression shows a clear AO/NAO-type pattern of alternating cold land and warm ocean temperature anomalies, indicating that solar forcing affects regional scales much more strongly than global or hemispheric scales. [264] Ocean sediments show a decreased SST of 1° to 2°C in the Sargasso Sea during the 16th to 19th centuries, which is consistent with a reduced NAO but not with uniform basin-wide cooling, while other evidence suggests colder North Atlantic temperatures during those centuries, including evidence for increased sea ice around Iceland. [264]

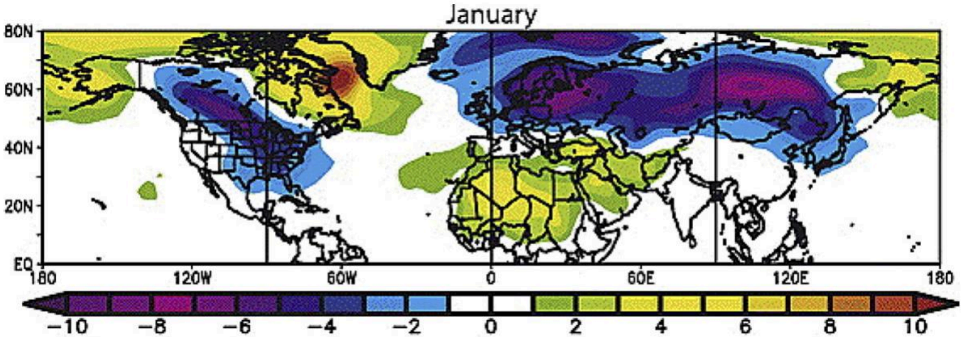

Figure 7.8: This figure displays a global map of surface temperature anomalies for January, illustrating the pattern associated with the negative phase of the North Annular Mode, which corresponds to periods of reduced solar output. The map uses a color scale from −10°C (dark purple) to +10°C (dark red), showing significant cooling (purple/blue) over the Arctic and northern North America, with warming (yellow/green) in mid-latitudes and tropical regions. This pattern closely matches the temperature anomalies observed during the late Little Ice Age (1650–1850). (source: ref 268)

The proposed link between solar activity and climate hinges on a microphysical mechanism connecting cosmic ray ionization in the Earth's atmosphere to cloud formation. [265] This relationship may provide

an explanation for reported tropospheric and stratospheric oscillations, supporting the hypothesis that solar modulation of cosmic rays affects cloud cover and, consequently, the climate. [96] A comparison of this low-noise radionuclide production record with changes in the geomagnetic dipole field strength demonstrates that geomagnetic shielding is the primary driver of multimillennial variability, establishing that stronger geomagnetic fields correspond to lower cosmic radiation levels. While solar modulation dominates cosmic radiation variations on multidecadal to centennial time scales, as indicated by the coincidence of radiation maxima and grand solar minima, the influence of solar activity diminishes over longer periods. [52][213][11][204][266][170] Research at the GeoForschungsZentrum (GFZ) Potsdam provided fine detail of relative paleointensity variations, recording the magnetic field strength at the Kolbeinsey Ridge in the Iceland Sea over the past 300,000 years. [206] This data indicates that when the magnetic field is strong, it shields the Earth from galactic cosmic rays, whereas weak fields near reversals allow bombardment of equatorial regions. [206] Magnetostratigraphic studies established that the pattern of ice sheets in North America changed with each major reversal of the Earth's magnetic field polarity, correlating with topographic changes. [267] Consequently, periods of geomagnetic field reversal roughly correspond to cold episodes in paleoclimatic reconstructions, though this correlation is not strong. A detailed study revealed a weak but persistent correlation between Northern hemisphere temperature and geomagnetic field intensity during the last millennium, implying that cosmic rays play a role in climate variations. [213] The last two interglacial periods ended abruptly when the magnetic field was weak and at the point of a reversal, approximately 70,000 and 180,000 years ago, suggesting that geomagnetic weakening can amplify global cooling effects. [206] The existence of a physical mechanism, which is sufficiently strong, indicates that the deduced inverse correlation between solar cycle length and long-term variations in global temperature may be related to long-term variations in the solar modulation of cosmic-ray flux. [96] Thus, the atmospheric evidence, though indirect, supports the broader thesis that solar variability plays a significant role in modulating Earth's climate and geological activity.

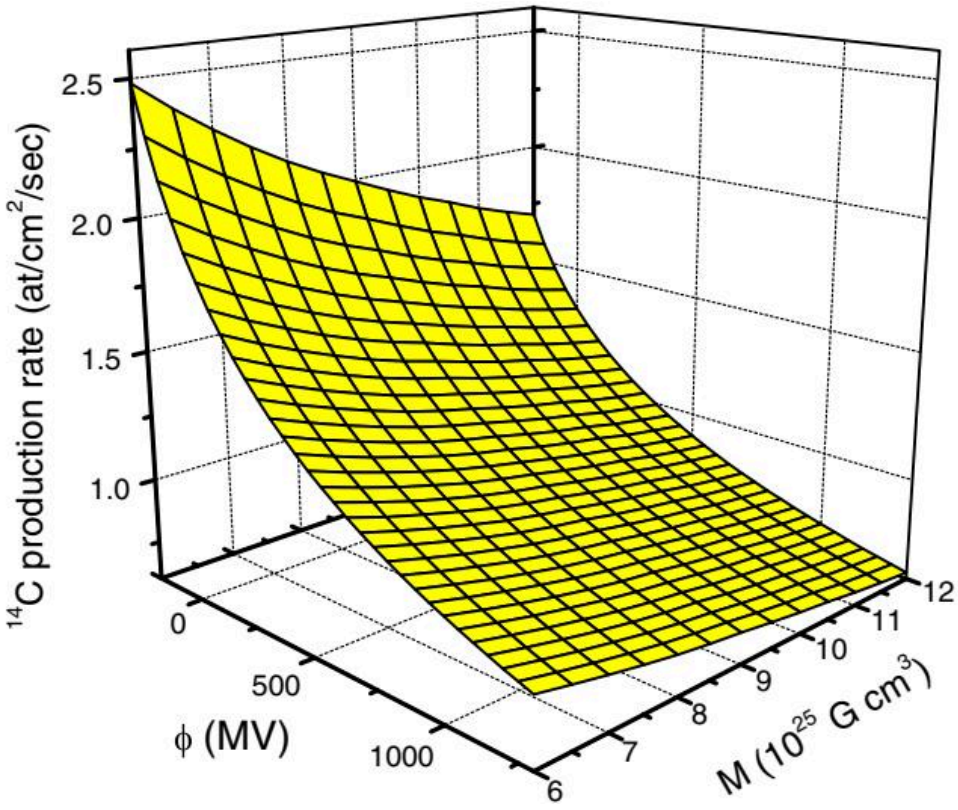

Figure 7.9: A 3D surface plot shows the globally-averaged production rate of carbon-14 (^{14}C) in atoms per square centimeter per second as a function of modulation potential (φ, in MV) on the x-axis and geomagnetic dipole moment (M, in 10^{25} G cm^3) on the y-axis. The surface, colored yellow, decreases monotonically with increasing φ and M, indicating that higher solar modulation and stronger geomagnetic fields reduce cosmic-ray-induced ^{14}C production. The plot illustrates the combined influence of solar activity and Earth's magnetic field on cosmogenic nuclide generation. (source: ref 43)

7.6 What If the Next Minimum Brings the Next Big Eruption

The Smithsonian Institution's Global Volcanism Program (GVP) database, which catalogs 1,408 Holocene volcanoes and 9,928 eruptions, provides the foundational data for such analyses, yet the completeness of this record varies significantly by era and eruption magnitude. [170] As noted by Newhall and Self, the relative completeness of eruption dates only begins around 1800 for Volcanic Explosivity Index (VEI) $\geq$ 5 events, around 1900 for VEI = 4, and around 1960 for VEI = 3. [204] This temporal bias means that the striking increase in recorded VEI = 3 eruptions since 1800 likely reflects the progressive improvement in observing and reporting smaller eruptions, rather than an actual increase in worldwide volcanism. [204] Consequently, the historical record is spotty, especially for the period before the sixteenth century, and any analysis of long-term trends must account for these data gaps. When examining the annual frequency of eruptions from 1700 to 2020, researchers have applied smoothing filters to eliminate random variations, assuming that data gaps are a random process. [156] However, the incompleteness of the pre-modern record implies that many significant eruptions may have gone unrecorded or remain unknown to science. This uncertainty is critical when projecting future hazards. [76] Consequently, establishing these geological baselines indicates the potential for future large-scale eruptions to coincide with solar minima, highlighting the critical need for rigorous hazard assessment in regions like Peru where populations reside near active volcanic structures.

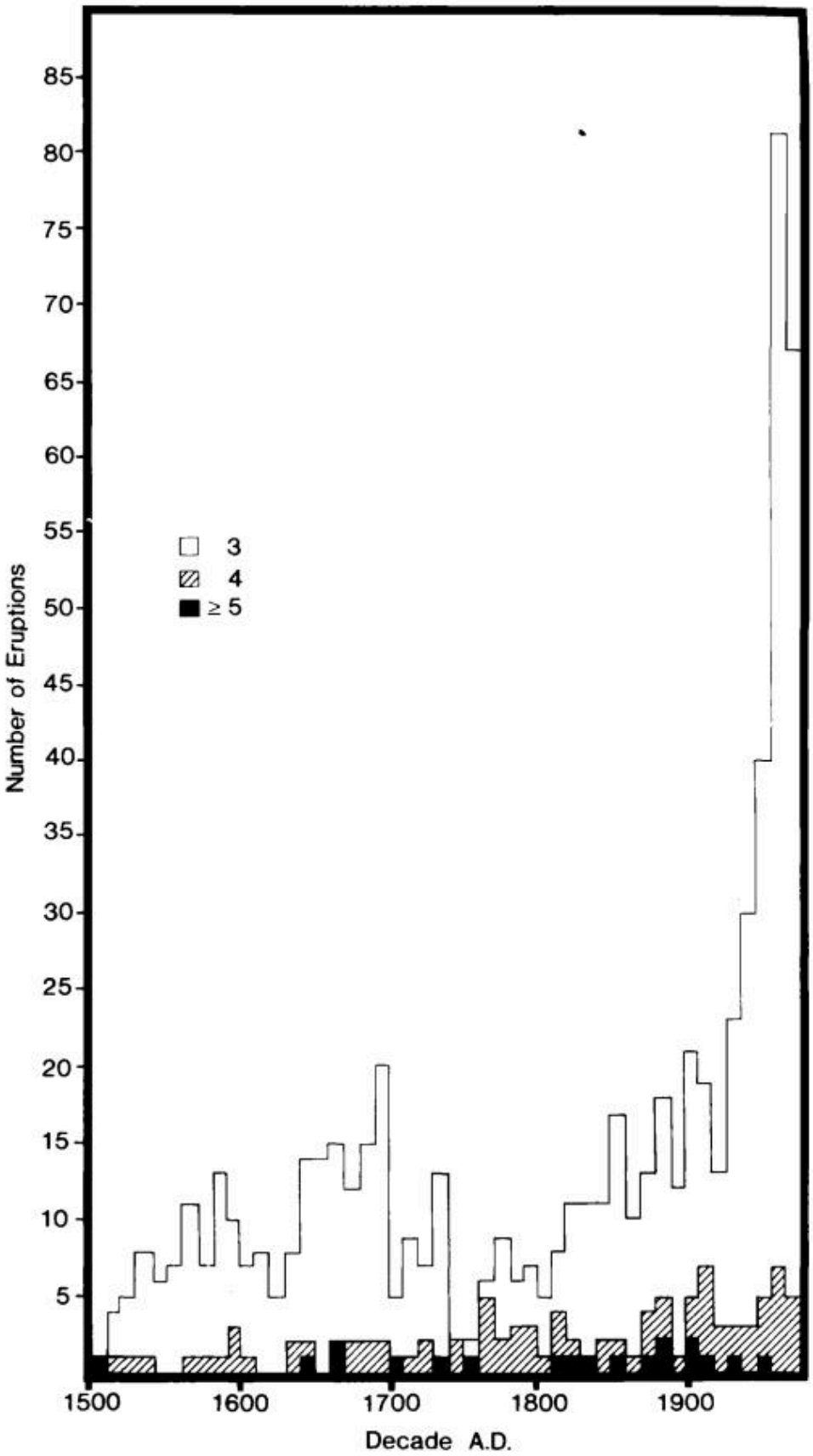

Figure 7.10: This bar chart displays the number of volcanic eruptions by Volcanic Explosivity Index (VEI) from 1500 to 1950 A.D., categorized into VEI 3 (white bars), VEI 4 (hatched bars), and VEI ≥5 (black bars). The data shows a sharp increase in the frequency of VEI 3 eruptions throughout the period, particularly after 1800, while the number of VEI ≥5 eruptions remains low and relatively stable, with only slight increases over time. (source: ref 256)

Attributing climate change to specific volcanic eruptions is challenging due to competing natural variability factors like solar radiation and oceanic oscillations. For instance, the massive Icelandic Laki eruption of June–August 1783 did not produce prompt apparent global cooling, likely because a strong El Niño event in 1782–1783 acted as an unknown moderating factor that diluted the volcanic signal. [269][204][46][71][1] Although large enough eruptions can poke through this variability to produce discernible effects in climatically sensitive regions like Europe, the need to treat each volcanic eruption on an individual basis remains critical. [269] Fumarolic activity had probably remained mild for at least tens of years, as historical accounts report that Indian people used to climb and perform offerings to Huaynaputina prior to AD 1600 with the aim of appeasing its activity. [240] The small amount of lithic fragments in the AD 1600 pumice-fall deposit indicates that the vent was already open in the amphitheater's floor prior to the eruption, allowing the plinian column to evolve quickly. [240] Without repeated experiences, the process whereby managers evolve measures of coping with disasters does not take place. [38] The National Hurricane Center confirmed this insight after the 2004 and 2005 hurricane seasons, noting that those who have 'never experienced a direct hit by a major hurricane' seem incapable of envisaging what one is like. [38] Furthermore, those who have experienced such events 'only remember the worst effects of a hurricane for about seven years.' Consequently, predictions that the risk of a significant event is substantial do not, historically, generate the collective will necessary for us to make investments in resiliency. This holds true even when science indicates quite clearly that the event is quite likely to happen eventually and that the consequences of being unprepared will be severe. [38] As Clive Hamilton observed, 'Sometimes facing up to the truth is just too hard. [38] When the facts are distressing it is easier to reframe or ignore them.' [38] Geological Survey national volcanic threat assessment demonstrates the utility of this kind of risk analysis by ranking volcanoes into five relative threat groupings based on a 24-factor schema. [270] This methodology accounts for the highly variable knowledge of eruptive histories of more than 160 active U.S. volcanoes, as well as the diversity of eruptive styles and geographic settings. [270] By prioritizing where to focus volcanic risk mitigation through research, monitoring, hazard assessment, and community engagement, the framework serves as an effective communication tool for engaging stakeholders and the public. [270] The adaptation of this threat assessment methodology by groups in Chile, New Zealand, Argentina, the Caribbean region, and Peru, along with its inclusion in the United Nations Office for Disaster Risk Reduction Global Assessment Report for Risk Reduction 2015, suggests the broad applicability of such structured risk management frameworks. [270]

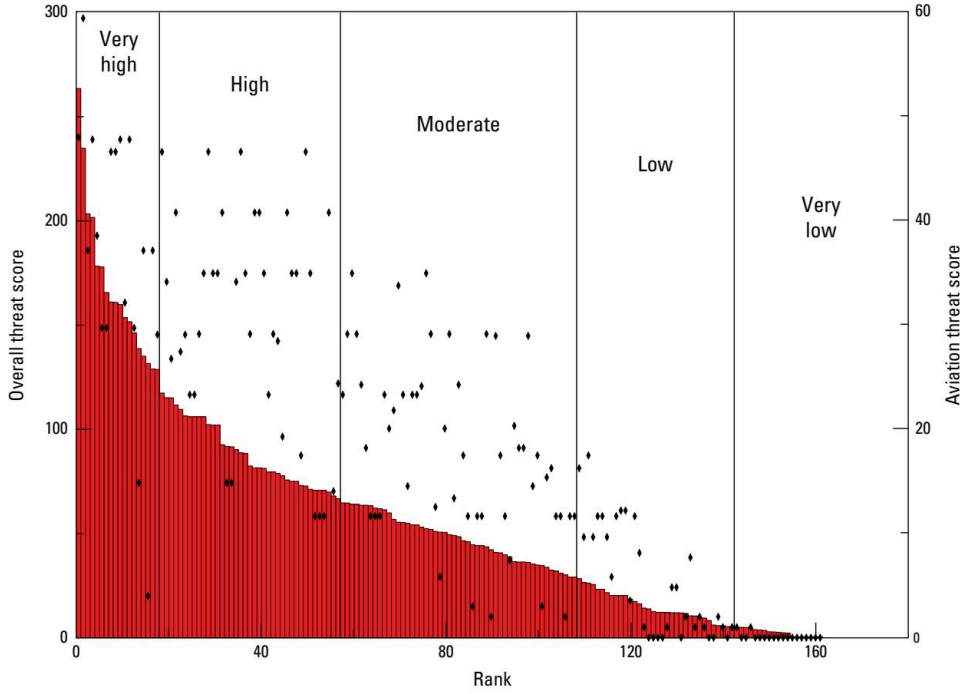

Figure 7.11: The figure displays a composite visualization of volcanic threat assessments for U.S. volcanoes, combining a ranked histogram of overall threat scores with scatter points for aviation threat scores. The left y-axis shows overall threat scores (0–300) plotted as a red histogram against rank (0–160), with vertical bands labeling threat categories: Very high, High, Moderate, Low, and Very low. Black diamond markers represent aviation threat scores (right y-axis, 0–60) plotted against the same rank order, showing a general decrease in both threat metrics with increasing rank. (source: ref 270)

Modeling extreme volcanic events remains difficult because the information needed to constrain the frequency of outliers in probability distributions is often lacking. The frequency data for past volcanism has significant shortcomings and is generally incomplete, as noted by Newhall and Self. [271][156][204] [272][273][241] While the decadal rate of all eruptions recorded in ice cores has remained approximately uniform for the last 1000 years, eruptive frequency estimates from other sources show a marked increase as they approach the present. [271] This apparent rise is largely attributed to the advent of satellite observations, which were able to catalogue smaller eruptions globally, rather than an actual increase in worldwide volcanism. [271] Extensive ice core samples reflect the occurrence of large eruptions but fail to capture the small ones. [271] Conversely, recent short-term observations accurately represent small, more frequent eruptions, but the repose times of the larger eruptions are beyond the length of the record. [271] Consequently, the relative frequencies of eruptions for the period 0–999 AD are much less than for the period 1000–2000 AD, leaving it unclear whether this reflects an actual lull in volcanism or a failure of the record to capture or preserve the events.

The geological record of Vesuvius reveals that prehistoric eruptions, specifically the Pomici di Base and Avellino Pumice events occurring 22,000 and 4,300 years ago respectively, were accompanied by debris avalanches that reached the coast. [76] This historical evidence suggests that future large-scale flank failures of volcanoes like Vesuvius raise implications for tsunami hazards associated with debris avalanches reaching the coast. Structural failure of the volcanic edifice could also occur, triggering landslides and potentially caldera formation, while mixing of ground water and magma within the conduit during the waning stages of an eruption could produce hydrovolcanic explosions. [76][270][256] The difficulty of reconciling purely statistical analyses of eruption frequency and clustering with what the geological record tells us about magma-reservoir processes means no one knows when Vesuvius will reawaken. [76] The 2018 update to the U.S. [270] This assessment framework underscores the need to monitor specific physical indicators, such as whether a volcano has produced a tsunami within the Holocene or has hydrothermal explosion potential due to extensive thermal features. [270]

8. There Is No Such Thing as Settled Science

Warming did occur, but the dominant driver was solar activity — not anthropogenic CO_2 — and the natural CO_2 budget plus low climate sensitivity make a CO_2-only attribution untenable.

8.1 Warming Happened but Who Did It

The twentieth century witnessed a pronounced warming trend, a fact that serves as the foundational premise for the dominant narrative attributing recent climate change primarily to anthropogenic carbon dioxide emissions. [231] In a pivotal study, Schurer et al. compared the expected signatures of high and low solar forcing against an ensemble of surface air temperature reconstructions for the past thousand years, carefully accounting for internal climate variability, volcanic eruptions, and uncertainties in both proxy data and model outputs. [274] Consequently, the mainstream interpretation holds that the warming observed in the Northern Hemisphere cannot be explained by solar cycles alone, setting the stage for a debate that centers on whether the current attribution models have adequately separated natural multi-decadal oscillations from anthropogenic signals or if they have inadvertently dismissed a more substantial solar contribution due to an underestimation of total solar irradiance variability and its potential amplification mechanisms. Their results demonstrate that while volcanic and greenhouse gas forcings contribute most to pre-twentieth-century climate variability, the contribution by solar forcing is modest. [274] Crucially, the study establishes that the 95% upper limit on the solar scaling factor rules out a solar contribution from the Maunder Minimum to present that is greater than about 0.15 K. This finding holds even when considering potential missing solar–ozone feedbacks, which would predominantly impact regional temperatures rather than enhancing the hemispheric mean response. [274] The authors conclude that for solar forcing to be a strong driver, the real-world climate sensitivity to it would have to be almost an order of magnitude smaller than in climate models, a scenario they consider highly unlikely. [274] Thus, the evidence shows that solar forcing is not a strong driver of large-scale Northern Hemispheric temperature variability over the past millennium, undermining the claim that solar activity alone accounts for the observed warming trend.

The global mean annual surface temperature increased 0.55°C from 1860 to 1990, a period coinciding with a steady rise in overall solar activity levels. [275] While standard climate models incorporating small total solar irradiance (TSI) changes of approximately 0.1% attribute recent warming primarily to anthropogenic greenhouse gases, this consensus view faces significant challenges from alternative reconstructions. [60] Temperature records derived from boreholes, such as the study by Huang et al., provide robust evidence for a 1.0–1.5 K difference between the Medieval Warm Period and the Little Ice Age, contradicting reconstructions that show minimal variation. [60] Consequently, some studies utilizing high solar variability estimates, which propose TSI changes of the order of 0.4%, argue that solar variability may have been the dominant cause of long-term warming since the 19th century. This perspective highlights the possibility that irradiance from the quiet Sun varies significantly in time, offering a natural explanation for the warming trend that does not rely solely on industrial CO_2 emissions. [60][30][1][45]

The unusual warming of the 20th century is mainly due to the coincidence of two highs in the 65-yr oscillation within the century, and an unusually high level of solar activity that reduced the mid-20th century cooling and increased the LTCW. [1] If we interpret the role of the interdecadal oscillation as a redistribution of heat from the lows to the highs of the oscillation, then this interpretation of MGW attribution assigns 10–20% of the 20th century temperature increase to GHGs, and 80–90% to solar activity. That 80–90% figure is the upper end of the solar-attribution estimates presented across this book — from the high-variability TSI reconstructions that make the Sun the dominant cause of the warming since the nineteenth century, up to this near-total attribution — and every one of them puts the Sun, not carbon dioxide, in the driver's seat. The MSM is a period of 70 years with above average solar activity, representing the longest such period in the 320-yr sunspot record. [1] That the Modern Maximum coincides with the biggest period of warming in 600 years should not be considered as unrelated coincidence. [1] A test of this interpretation is about to take place. [58] Extrapolation of the forcings indicates we have entered, for the first time since 1900, a period when low solar activity coincides with a low in the 65-yr oscillation. [1]

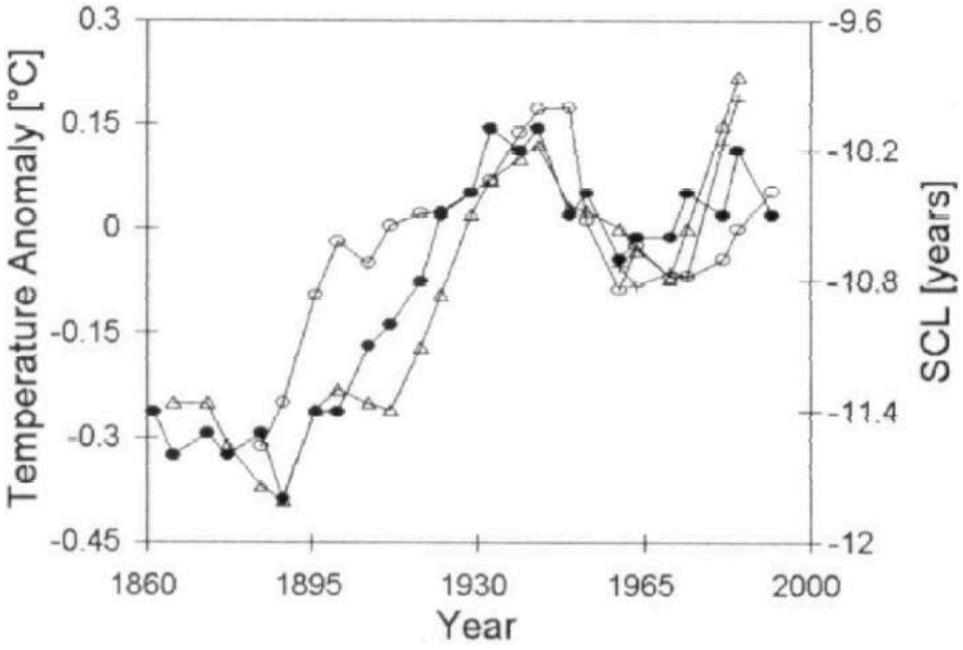

Figure 8.1: The chart displays temperature anomalies in degrees Celsius (left y-axis) and solar cycle length (SCL) in years (right y-axis) as functions of year from 1860 to 2000. Multiple time series, marked with different symbols, show temperature anomalies generally increasing from the late 19th century, with notable fluctuations, while SCL exhibits a decreasing trend over the same period, suggesting a potential inverse relationship between solar activity and global temperature anomalies. (source: ref 276)

The official consensus within climate science, as articulated by Working Group I of the Intergovernmental Panel on Climate Change (IPCC), maintains that solar activity exerts only a limited influence on terrestrial climate dynamics. [8] However, this consensus overlooks abundant empirical evidence suggesting that the Sun has had a large influence on climate over the Holocene period, with temperature changes between periods of low and high solar activity reaching the order of 1–2 K. Such large variations are inconsistent with the consensus and herald a real and solid connection between solar activity and Earth's climate, challenging the notion that solar effects are insignificant. [60]

The historical record provides a compelling counter-narrative to the idea that recent warming is an unprecedented anomaly driven solely by industrial emissions. [275] Specifically, the Wolf Minimum (c. Radiocarbon dating of pine tree rings, for instance, has identified a stationary climate oscillation of approximately 210 years that coincides with these grand minima, further supporting the link between solar variability and temperature shifts. [19] This historical precedent challenges the assumption that the twentieth-century warming trend is entirely novel. [87]

8.2 The Natural CO_2 Budget

The prevailing narrative of anthropogenic dominance often overlooks the fundamental sequence of events recorded in the deep past, where temperature changes clearly precede carbon dioxide fluctuations. [7] This temporal relationship is not a minor anomaly but a robust feature of the paleoclimate record; variations in CO_2 over the last 420 kyr broadly followed Antarctic temperature, typically by several centuries to a millennium. [7] The data establish that atmospheric CO_2 concentrations lag temperature increases by 800 ± 400 years during glacial terminations. For instance, at Termination III, a warming event that occurred over a 5000-yr period, the CO_2 increase occurred 800 ± 200 years after the Northern Hemisphere deglaciation. [277][7][278][279] The ice core data confirm that temperature leads CO_2, a fact that challenges the assumption that rising CO_2 is the sole or primary cause of recent warming. [279] The ocean acts as a vast reservoir, releasing gas as it warms, a process governed by Henry's law. [8] The lag observed in the ice cores is consistent with this view, where temperature changes drive the carbon cycle, not the other way around. [277] Thus, the natural CO_2 budget, shaped by solar forcing and oceanic response, offers a coherent explanation for the observed CO_2 increases without requiring an exclusive attribution to human activity.

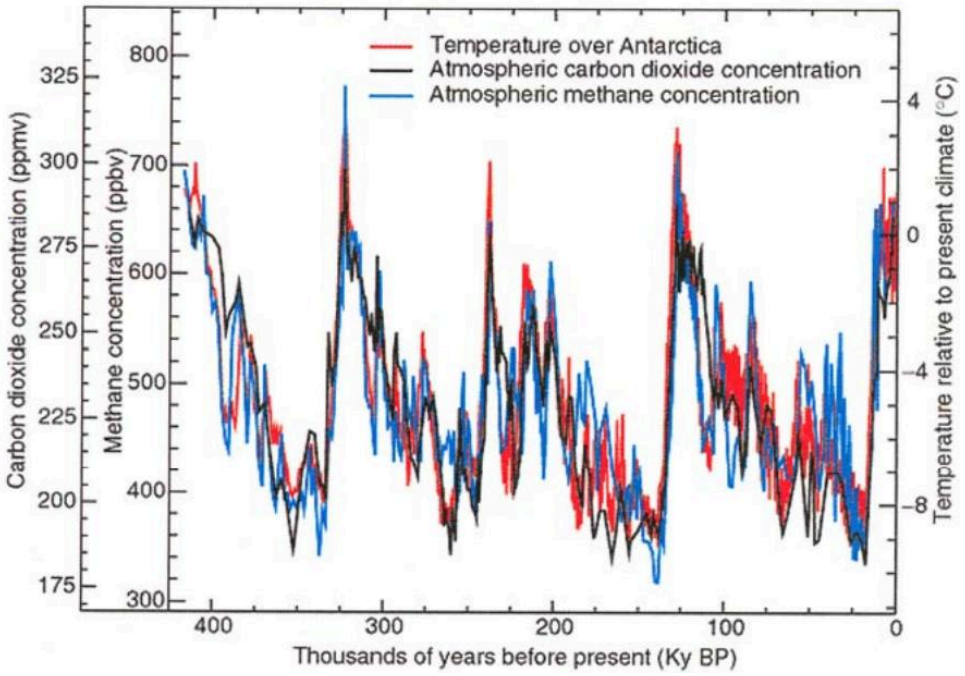

Figure 8.2: A line graph displays four hundred thousand years of proxy data from ice cores, showing temperature over Antarctica (red, right y-axis in °C relative to present climate), atmospheric carbon dioxide concentration (black, left y-axis in ppmv), and atmospheric methane concentration (blue, left y-axis in ppbv), all plotted against time in thousands of years before present (Ky BP). The data reveal strong correlations between temperature and greenhouse gas levels, with both CO_2 and CH_4 concentrations fluctuating in phase with temperature changes across multiple glacial-interglacial cycles. (source: ref 279)

The oceans store approximately 50 times more carbon dioxide than the atmosphere, yet this vast reservoir is not static; its capacity to hold gas is strictly temperature dependent. [279] The historical record confirms this dynamic: during glacial terminations, temperature changes precede carbon dioxide shifts by 400 to 1,000 years, indicating that terrestrial temperature drives atmospheric carbon dioxide levels rather than the reverse. [280] Consequently, the observed increase in carbon dioxide since the Little Ice Age is consistent with natural ocean warming driven by solar heating, which reduces solubility and triggers outgassing. While carbon isotopic ratios indicate a contribution from fossil fuel burning, this accounts for only 1 to 5 percent of the total increase, suggesting that the dominant driver of rising carbon dioxide is the thermal response of the oceans to natural climate cycles, not anthropogenic emissions. [281]

Modern observational studies suggest that atmospheric CO_2 changes lag global surface temperature changes by approximately 9 to 12 months. This temporal sequence is consistent with the mechanism where temperature controls the CO_2 level, as evidenced by MacRae who found that atmospheric CO_2 changes lag atmospheric temperature changes by about nine months. [1][278][50] Furthermore, Humlum et al. show that CO_2 increases consistently follow temperature increases by about 9 to 12 months, indicating that the correlation between cause and effect data proves there is no observable cause-effect relationship in the opposite direction. The lack of a statistically significant correlation between the rate of human carbon emissions and the rate of change of global surface temperature, even using time lags up to 20 years as found by Munshi, supports the view that temperature drives CO_2 rather than vice versa. [278] This aligns with the broader finding that CO_2 increases do not correlate with human CO_2 emissions but instead follow temperature increases, reinforcing the hypothesis that earth's temperature is driving atmospheric carbon dioxide levels. [278] Thus, the observed lag and correlation patterns indicate that natural processes, particularly ocean outgassing driven by surface temperature, play a dominant role in atmospheric CO_2 variations. However, this foundation appears unstable when scrutinizing the historical measurement series. For instance, Charles Keeling's acceptance of the French chemist Reiset's data as the most accurate from the late 19th century ignored a critical methodological flaw: Reiset used sulphuric acid to dry the air before analysis. [10] Because sulphuric acid absorbs part of the CO_2, the results are too low by about 20 ppm, a fact known since 1848 and tested quantitatively by the Belgian chemist W. [10] Spring in 1883. Consequently, the correct average in the end of the 19th century was 312 ppm, not the

294 ppm that fit Keeling's impression of pre-industrial levels. If the pre-industrial level was not 280 ppm, the argument that human CO_2 causes all the increase above that threshold loses its empirical grounding. [282] Beck's reconstruction from chemical data further supports this, showing levels that reached 440 ppm in 1820 and again in 1945, contradicting the low proxy ice-core values that have dominated the discourse. These findings suggest that natural fluctuations may have played a more significant role than currently acknowledged. [282][10][7] Consequently, the attribution of recent CO_2 rises exclusively to anthropogenic sources remains open to debate. However, ice-core data from Siegenthaler and Joos indicate that natural CO_2 increased by 17 ppm, or 6 percent, before 1900, when human emissions totaled only 5 ppm, contradicting the assumption of constant natural variability. Furthermore, Beck's reconstruction from chemical data shows the level reached 440 ppm in 1820 and again in 1945, suggesting that historical CO_2 levels were much higher than derived from ice cores alone. Jaworoski explains why ice-core data do not properly represent past atmospheric CO_2, concluding that nature produces 97 percent of atmospheric CO_2. [282] Analysis of ice core data through glacial and interglacial transitions consistently demonstrates an association between carbon dioxide and temperature, yet the climatic temperature always changed first, with carbon dioxide levels following after a measurable lag time of 400 to 1,000 years. [50] This sequence indicates that Earth's temperature drives atmospheric carbon dioxide levels rather than the reverse, a mechanism explained by the vast storage capacity of the oceans, which hold far more carbon dioxide than the atmosphere. [16] Because carbon dioxide is soluble in water and its solubility decreases as water temperature increases, the gentle natural warming of the world's oceans releases carbon dioxide into the atmosphere. [50] This physical process suggests that temperature-driven ocean outgassing is the main cause of the CO_2 increase since 1750, particularly as the oceans have warmed since the Little Ice Age. [278] The observed climate change is consistent with variations in albedo and associated ocean warming and cooling, supporting the view that this is merely a natural cycle evident in palaeoclimate data for most of the last 10,000 years. [281] At annual and 2-7 year time scales, the concentration of CO2 in the atmosphere is strongly driven by the ocean, and at longer time scales, greenhouse gas concentrations lag behind temperature. [281] Carbon isotopic ratios indicate that while there is a contribution from the burning of fossil fuels, it is of the order of 1-5 percent of the increase, implying that the warming of the oceans is a major contributor to the observed rise in CO2. [281] Furthermore, the Earth's atmosphere is fairly stable and resilient; carbon dioxide levels during the Ordovician period were approximately 5,000 ppm, yet these high levels did not throw the world into runaway global warming. If exceptionally high carbon dioxide levels did not cause runaway global warming in the past, it is reasonable to question why minimal levels of 387 ppm would do so in the future, reinforcing the conclusion that the available evidence indicates climate change is predominantly natural and occurs mostly in response to variations in solar heating of the oceans. Consequently, the attribution of recent warming primarily to anthropogenic emissions appears to be an oversimplification of a complex, naturally driven system. [50][281][280][279] [283][282]

8.3 The Surface Temperature Record Under a Magnifying Glass

The integrity of the global surface temperature record remains a focal point of contention, particularly regarding the influence of urbanization on land-based measurements. [94] This shift is particularly acute in regions like China, where rapid acceleration in urbanization has transformed most formerly rural stations into urbanized sites, suggesting that urbanization bias is a persistent problem for many station records. [139] Consequently, the reliance on homogenization algorithms to smooth through excess warming in cities may inadvertently smear warmer urban temperatures over large areas, potentially inflating the Global Surface Air Temperature (GSAT) estimates used in recent assessments.

The standard defense of global temperature datasets relies on statistical homogenization techniques, such as the Menne & Williams algorithm, which are designed to remove non-climatic biases from raw station records. [139] Proponents argue that these automated methods substantially reduce urbanization bias, thereby rendering the combined urban and rural data representative of true hemispheric trends. [94] However, this confidence is challenged by evidence suggesting that the algorithm performs poorly when a substantial fraction of neighboring stations share similar non-climatic biases. In such scenarios, the method can lead to "urban blending," a process where the urbanization bias of heavily urbanized stations is not removed but rather averaged with neighbors. [139] Consequently, if rural stations are few, they may have artificial urbanization bias introduced into their records, effectively aliasing the urban signal onto rural trends. Critics dispute homogenization methodologies, arguing they may inadvertently cause 'urban blending' that aliases urban bias onto rural stations. This implies that the homogenized Global Historical Climatology Network may retain significant systematic errors, particularly in regions where

siting biases are widespread, undermining the assumption that statistical adjustments fully correct for the urban heat island effect. [139][49][94]

The integrity of the terrestrial temperature record since 1900 faces scrutiny from urban heat-island effects, which may distort the apparent warming trend. [8] Analysis of 5x5 degree grid boxes by Jones and Moberg reveals that statistically significant warming trends are present in only 10–20% of available boxes, with most land-area warming concentrated near large cities and urban centers rather than being uniformly distributed. [284] This spatial correlation suggests that urbanization and land-use change, rather than greenhouse gases, drive the most pronounced local increases. [284] Further evidence indicates that standard adjustments for these non-climatic factors are insufficient. [8] Ross McKitrick and Patrick Michaels demonstrated a strong correlation between urbanization indicators and "urban adjusted" temperatures, concluding that fully correcting the surface temperature data for such extraneous factors reduces the estimated 1980–2002 global average temperature trend over land by about half. [8] Similarly, Jos de Laat and Ahilleas Maurellis found a statistically significant correlation between the spatial pattern of warming and industrial development, adding a large upward bias to the measured global warming trend. [8] The experience at the Urbana, Illinois site underscores this challenge, where a gradual warming of 0.9°C occurred as the university campus grew around the station from 1900 to 1983, followed by immediate cooling upon relocation to a rural setting. [8] These findings suggest that inadequate urban heat-island adjustments could account for up to half of apparent terrestrial warming since 1900. Consequently, the magnitude of anthropogenic warming may be substantially overstated if these localized biases are not fully accounted for. [284][8][285]

The integrity of the surface temperature record hinges on whether urbanization has introduced a measurable warming bias, a question that remains contentious despite widespread assertions to the contrary. [139] While some analyses suggest minimal impact, empirical comparisons between urban and rural stations reveal significant temperature differences that contradict claims of no statistically significant urbanization impact. This discrepancy is not merely theoretical; it manifests in concrete data from diverse global locations. [8][139][94] For instance, Ren et al. noted that annual urbanization-induced warming at Beijing and Wuhan stations accounted for about 65–80% of the overall warming in 1961–2000, demonstrating that local anthropogenic effects can dominate regional trends. [139] Similar nocturnal warming and daytime cooling patterns were observed in California's Central Valley by Christy et al., where increased irrigation suppressed daytime temperatures via evaporative cooling while warming nights through increased heat capacity. [8] These findings, echoed in studies across China, Europe, and even remote villages like Barrow, Alaska, confirm that urban heat-island effects are pervasive and often greatest at night and in higher latitudes during winter. [8] Consequently, the assertion that current surface air temperature records are free from urbanization-induced bias is undermined by numerous studies showing significant warming in urbanized areas, necessitating careful scrutiny of homogenization procedures that may inadvertently retain these artificial signals rather than removing them.

The construction of rural-only station composites serves as a critical methodological check, designed to avoid the potential artifacts introduced by homogenization procedures and thereby provide an alternative estimate of temperature trends. This approach is particularly relevant in regions with a high density of rural stations, where the distinction between raw and adjusted data can significantly influence the perceived magnitude of warming. [94][139] The underlying premise is that raw rural records may offer a more authentic representation of broader climatic shifts, especially when compared to homogenized datasets that incorporate both urban and rural observations. [94] This distinction is vital because the homogenization process, while intended to correct for non-climatic biases, can sometimes introduce its own set of uncertainties. [139] Consequently, the resulting rural-only composites suggest that the temperature trends derived from these unadjusted records might differ from those obtained using standard global datasets. This divergence highlights the importance of scrutinizing the data sources and processing methods used in climate studies, as the choice between raw rural data and homogenized global records can lead to different interpretations of historical temperature changes. [94]

The integrity of the surface temperature record, particularly in regions undergoing rapid development, remains a subject of rigorous scrutiny. [139] In China, for instance, the times of observation since 1953 appear to have been well regulated, yet this level of consistency does not seem to have been the case for earlier records. [139] While it is plausible that some of the net adjustments applied by Menne & Williams are a result of correcting for time of observation bias, the evidence suggests that such biases are quite modest for the Chinese network. [139] Tang & Ren attempted to partially account for time of observation bias by using a combination of maximum and minimum temperature records, yet their reconstruction was quite similar to the gridded mean average when using the non-homogenized dataset. [139] This similarity suggests that the net biases from changes in time of observation are quite modest for the Chinese network. [139] Still, this does not rule out the possibility that the relatively large pre-1950s

Menne & Williams adjustments may be correctly removing some other non-climatic biases, such as those introduced by station moves. On the other hand, when the number of fully rural stations in an area is low, as was the case pre-1951, homogenization algorithms such as the Easterling & Peterson 1995 algorithm used by Li et al. will lead to urban blending. [139] This process means that the urbanization bias will tend to be distributed amongst all stations, both urban and rural, to generate a uniform "homogenous" blend. [139] Indeed, the magnitude of the adjustments for the pre-1951 period is actually greatest for the fully rural subset, and the homogenization algorithm reduces the warmth of the mid-20th century warm period, effectively introducing a warming trend into the fully rural subset. This pattern is consistent with urban blending. [139] If the homogenization algorithm has indeed introduced urban blending, then this would have reduced the reliability of the station records, rather than improved it. [139] Consequently, homogenization adjustments in Chinese records pre-1951 are greatest for rural subsets, potentially introducing artificial warming trends via urban blending. This mechanism explains why Li et al. failed to identify much urbanization bias in their analysis, as the algorithm effectively masks the very signal it seeks to correct. [139] The implication is that the rural-only composites, often cited as cleaner proxies for natural variability, may themselves be contaminated by the statistical artifacts of homogenization. [139] When urban blending occurs, the distinction between rural and urban stations blurs, and the resulting composite inherits the urban heat island bias. [139] This does not negate the warming itself, but it does complicate the attribution of that warming to specific drivers. [286] The lesson from the Chinese records is that homogenization is not a neutral process; it can actively reshape the temperature trend, especially in periods with sparse rural coverage. [139]

8.4 TSI vs CO_2 the Connolly Soon Attribution

Central to this alternative view is the realization that the deep ocean carbon stores are so vast that carbon sinks can be considered unlimited in terms of anthropogenic emissions, a fact supported by large $\delta^{13}C$ excursions associated with the formation of large igneous provinces that formed over tens of thousands of years. [1] By recognizing that constant current emissions lead to a new equilibrium at 240 ppm above the present value, we see that the system is self-regulating through deep ocean carbon stores. [1] Thus, the focus shifts from panic over emissions to understanding the solar and natural cycle drivers that truly govern our climate, setting the stage for a more accurate assessment of future warming trends and the potential return of cooler conditions.

The historical temperature record for Greenland provides a critical test of anthropogenic forcing, as fluctuations over the past 500 years predate large CO_2 emissions and cannot be caused by them. Merged data from 1784 to 2005 reveal that the warmest period occurred in the pre-World War II era, specifically the 1930s and 1940s, before the massive global industrialization of the last 70 years and the emission of most greenhouse gases. [46][287][7][2][288] Furthermore, southern Greenland experienced a cooling of 1.29°C between 1958 and 2001, adding to the ice sheet's mass balance. These findings demonstrate that natural variability, rather than industrial emissions, drove these temperature shifts, ruling out CO_2 as the primary driver for the observed changes in the Greenland record. [8]

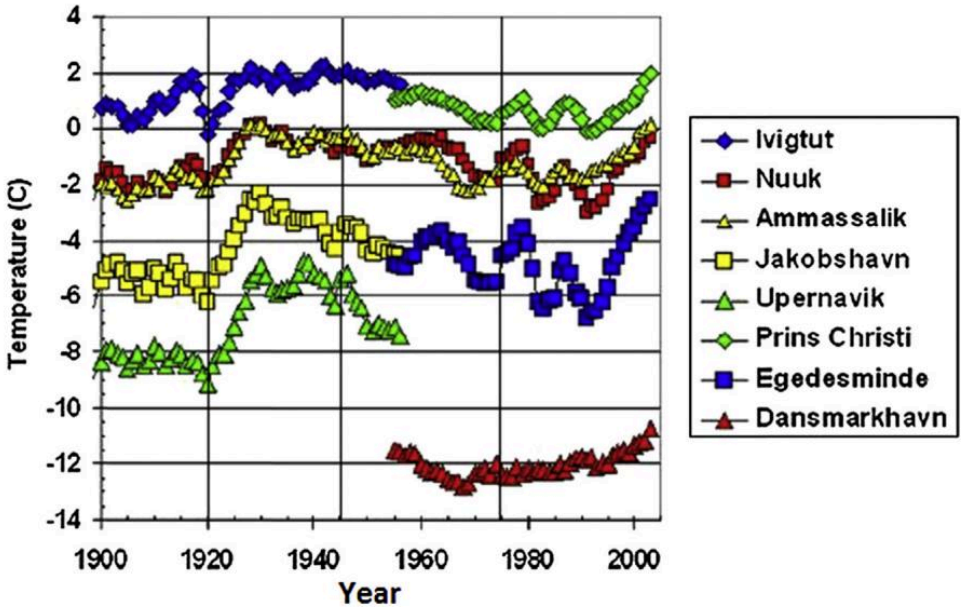

Figure 8.3: This line graph displays annual five-year average temperatures (°C) from 1900 to 2005 for eight Greenland weather stations: Ivigtut, Nuuk, Ammassalik, Jakobshavn, Upernavik, Prins Christi, Egedesminde, and Dansmarkhavn. The data shows that temperature trends vary significantly by location, with the 1995–2005 period exhibiting warming comparable to the 1920–1930 peak, but not surpassing it. (source: ref 8)

The mid-century cooling trend from 1945 to 1977, which occurred despite a significant post-1945 increase in CO_2 emissions, demonstrates that rising greenhouse gases were not the sole determinant of surface temperatures during that era. This period of cooling, juxtaposed against increasing anthropogenic forcing, challenges the assumption that CO_2 dominates short-term climate variability. [8] Instead, it suggests that natural factors, such as solar activity and internal climatic oscillations, played a substantial role in modulating global temperatures. [1] The coincidence of this cooling with specific phases of the ~65-year oscillation and solar cycles indicates that these natural drivers can counteract greenhouse warming on decadal timescales. [1] Consequently, the temperature record from 1945 to 1977 provides critical evidence that the climate system's response to forcing is more complex than simple CO_2-driven warming, highlighting the need to account for natural variability in attribution studies.

The attribution debate hinges on whether solar variability or greenhouse gases drove the twentieth-century warming. [231] While standard models assign a minor role to the Sun, alternative analyses suggest a much larger solar contribution. [230]

The discrepancy between predicted and observed temperature changes suggests that the IPCC's central value for doubling sensitivity, (S = 3.0 C), is far too large. [289]

The attribution debate hinges on which forcing best explains the observed warming. [1] The unusual warming of the 20th century is mainly due to the coincidence of two highs in the 65-yr oscillation and an unusually high level of solar activity that reduced mid-century cooling. [1] If this interpretation holds, the overwhelming share of the modern temperature increase belongs to the Sun rather than to greenhouse gases — the quantitative split was set out at the opening of this chapter. [1] This apparent success demonstrates that the models rely on several adjustable parameters, chosen specifically to produce agreement with the observed global average surface temperature, rather than robust physical constraints. The uncertainty in climate sensitivity, defined as the temperature increase produced by a doubling of greenhouse gas forcing, is a factor of three or larger, yet the IPCC presents a narrow range of 1.5 to 4.5 degrees Celsius. [290][7][1][289][45] Furthermore, the forcing effects from aerosols are highly uncertain, by at least 200% for the cloud-reflective effect, which is used in the construction of the attribution graphs. By tweaking these parameters, the models can match the "predicted" warming, but this fine-tuning obscures the fact that the projections fail to catch the actual temperature variations and cyclicities of the past 100 years. [7] The reliance on such adjustable inputs suggests that the attribution of warming to anthropogenic causes is not unequivocally tied to physical evidence, but rather to model assumptions that can be scaled to fit the data. [1]

The synthesis of solar attribution rests on the deep-time consistency between solar modulation and terrestrial climate, a relationship that extends far beyond the instrumental era. [60] John Eddy's early observations of the correlation between solar activity and European climate over the previous millennium further anchor this long-term trend. [60] This alignment suggests that the Sun's influence on climate is not a short-term anomaly but a persistent driver operating on decadal to millennial timescales. [60] It challenges the notion that recent warming can be attributed solely to anthropogenic factors, instead pointing to a natural cycle that has governed Earth's climate for centuries. [1]

8.5 Natural Cycles as Confounders Scafetta AMO PDO

A compelling example of such deterministic forcing is found in the Barents Sea, where long-term temperature records reveal clear periodicities linked to lunar mechanics. [291] If similar cycles operate globally, they could account for a substantial portion of the observed warming, thereby undermining the assumption that CO_2 is the primary driver. [286] Wavelet analysis of Arctic ice extent data reveals dominant cycles of approximately 18 and 74 years, mirroring patterns found in polar motion and North Atlantic water records. [292] Specifically, this 74-year cycle associated with polar position variations correlates with cold Arctic water outflow, indicating that lunar gravity modulates the release of cold water from the Arctic Ocean into the Greenland Sea. The phase delay between the polar-position cycle and the Greenland ice extent is estimated at about 18.5 years, representing a significant lag in the circulation of Arctic water. [293][292] This delay supports the view that the Arctic system does not respond instantaneously to forcing but rather integrates signals over decades. [84]

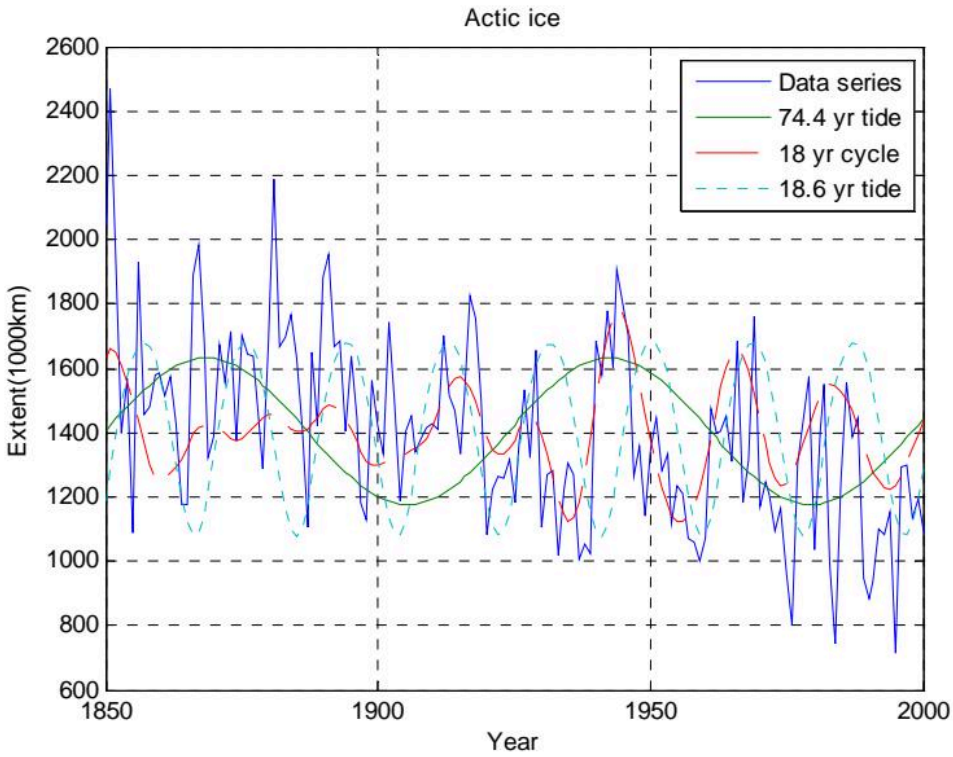

Figure 8.4: The graph plots Arctic ice extent (in 1000 km²) from 1850 to 2000, showing the observed data series alongside three modeled tidal cycles: a 74.4-year harmonic lunar nodal tide (green), an 18-year wavelet cycle (red), and the astronomical 18.6-year lunar nodal tide (dashed cyan). The data series exhibits significant variability, with the 74.4-year and 18.6-year cycles showing similar long-term oscillations, while the 18-year cycle appears to track shorter-term fluctuations, suggesting a potential influence of lunar tidal forces on Arctic ice variability. (source: ref 292)

The systems dynamics of North arctic cod operate as a non-linear, time-varying process dependent on ecology and landings systems, revealing a dynamic process closely correlated to temperature cycles of $3 \times 18.6 = 55.8$ years, 18.6 years, and $18.6 / 3 = 6.2$ years. [294] These temperature cycles are related to changes in the earth nutation and thus expected to be deterministic, with the 6.2 year cycle influencing

cod recruitment, growth rate, and landings, while the 18.6 and 55.8 year cycles influence growth rate and maximum biomass. [294] This deterministic structure suggests that a control strategy can manage the dynamics introduced by these temperature cycles, opening the door for simplified dynamic modelling and forecasting of future biomass. [294] Consequently, deterministic cycles allow prediction of long-term temperature fluctuations using Multi-Layer Feedforward Networks, which appears to support the view that Arctic temperature and biomass fluctuations follow predictable patterns rather than random noise. The climatological baseline, such as the Roemmich-Gilson climatology, treats the ocean as an Eulerian field, averaging measurements at fixed geographic locations over time. [295] However, ocean temperature is fundamentally a Lagrangian property, characteristic of specific water masses that move, mix, and transform as they are advected by currents. A water mass at 30° N, 150° W in January 2005 and another at the same coordinates in January 2018 are not the same physical entity; they possess different histories, source regions, and thermodynamic states. [295] Averaging their temperatures produces a statistical artifact rather than a meaningful physical baseline. [295] This Eulerian-Lagrangian mismatch is compounded by the temporal arbitrariness of the chosen averaging period. [295] The baseline is derived from smoothing measurements over the 2004–2018 period, a 15-year window that is physically arbitrary. [295] Major ocean processes, including mesoscale eddies, seasonal convection cycles, the El Niño-Southern Oscillation, the Pacific Decadal Oscillation, and Atlantic Multidecadal Variability, operate on timescales incommensurate with this averaging period. [295] Consequently, the resulting climatology reflects the specific dynamical state of the ocean during 2004–2018, including whatever phase each oscillatory process occupied, rather than any physically meaningful equilibrium state. Furthermore, changing float density and persistent spatial sampling gaps in polar domains introduce systematic biases, particularly when constructing climatological reference states.

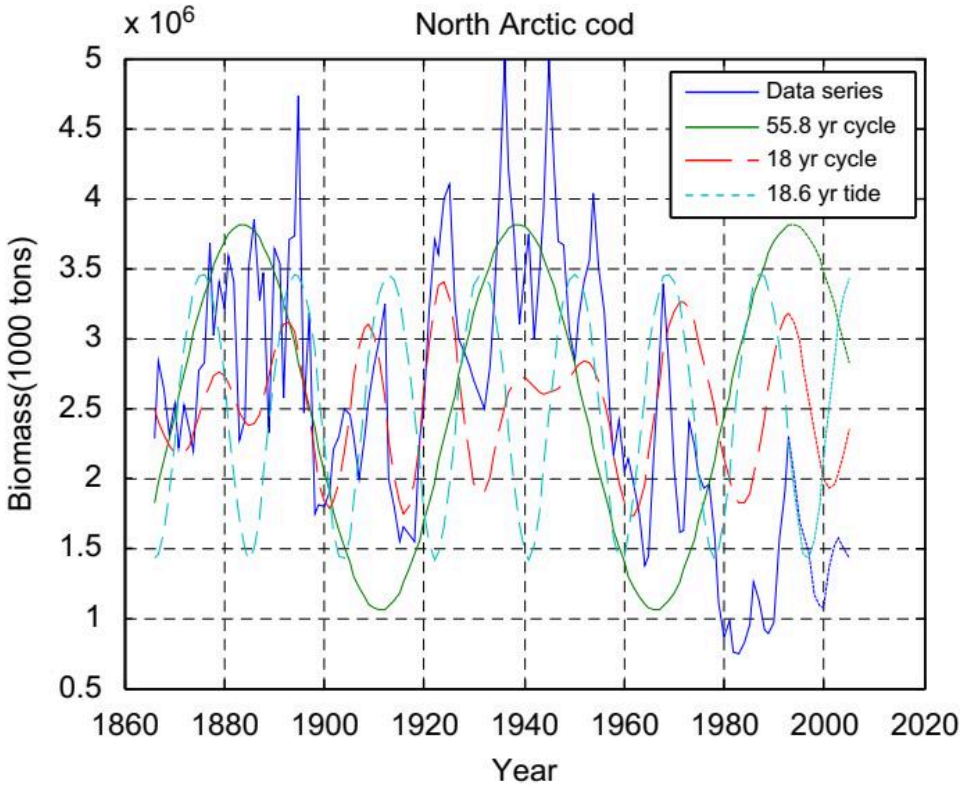

Figure 8.5: The figure displays the biomass of Northeast Arctic cod (in 1000-ton units) from 1866 to 2005 as a blue line, alongside three modeled cycles: a 55.8-year cycle (green), an 18-year wavelet cycle (red), and an 18.6-year tide cycle (cyan). The 55.8-year and 18.6-year cycles are scaled to align with the biomass data, illustrating their phase relationships to the observed fluctuations. The plot reveals that the biomass time series exhibits periodic oscillations that correspond closely to the superharmonic 55.8-year cycle and the astronomic 18.6-year tide cycle, with the 18-year wavelet cycle also showing a similar but less dominant periodicity. (source: ref 296)

The reliability of the Earth Energy Imbalance (EEI) assessment is called into question by the physical validity of the underlying Argo-float-based estimates of global Ocean Heat Content (OHC). [295] Rather than canceling out globally, these displacements are governed by local, non-stationary processes such as eddies, fronts, and turbulent shear, which introduce incoherent regional errors into Eulerian gridded fields. [295] When these errors accumulate, they create a time-dependent methodological bias in OHC trends, particularly when combined with interannual circulation variability like ENSO or PDO shifts. [295] A rough scaling suggests this effect could shift global EEI estimates by on the order of 0.02–0.1 W m^{-2}, a range comparable to or exceeding some published ensemble spreads that do not account for this foundational data-assignment flaw. [295] Furthermore, similar artifacts arise from how the reference climatology is constructed, where temperature profiles measured at different times during each month are pooled together and statistically fitted. Consequently, the confidence in EEI trends derived from these datasets is undermined by these unresolved methodological uncertainties. This uncertainty is not merely theoretical; it is embedded in the very metrics used to quantify the planet's energy state. [295] When these errors are synthesized, the resulting uncertainty is far larger than officially reported. [295] Consequently, the apparent energy accumulation driving the warming narrative may be an artifact of interpolation in unsampled volumes and framework discrepancies rather than a robust physical signal.

9. What Can We Do? Preparation for the Next Minimum

Take the Dalton and Maunder baselines as the operating analogue; every preparedness recommendation here improves resilience to extreme weather of any kind, even if the Grand Solar Minimum forecasts are wrong.

9.1 The Historical Baseline What Cold Periods Look Like

The historical record confirms that these epochs were not merely mild winters but extended periods of significant global cooling that triggered widespread famine, epidemic disease, and profound agricultural failure. [215] The evidence demonstrates that the primary threat was not just the cold itself, but the cascading failures in food production and public health that followed. [297] As noted in analyses of past solar minima, humanity has faced this danger before, and the manner in which we survived—through adaptation in housing, travel, and agriculture—offers a template for future preparedness. [280] The conditions of a small ice age constrain agricultural production, leading to famines that require long-term food storage and alternative heat sources to mitigate the massive power outages caused by ice and snow storms. [280] Therefore, understanding the specific impacts recorded in these historical texts is essential for developing a robust plan that addresses the real-world consequences of reduced solar activity, ensuring that our infrastructure and individual households are resilient enough to withstand the severe difficulties of a renewed Little Ice Age. Observers at St. The temperature at Fort Reliance, located 400 miles southeast of Fort Yukon, reached −69° F (−56° C), a figure that confirms the extreme thermal lows experienced in the region. [39] Natives reported that no winter of such severity had ever been known by them, highlighting the unprecedented nature of the event. [39] The consequences were dire: migrating birds arrived eight to ten days late, and the natives narrowly escaped starvation, being compelled in some cases to eat their dogs and the tanned sealskin covers of their boats. [39]

In the Gulf of Alaska and Yukon, oral accounts merge discussions of extreme cold with descriptions of surging glaciers, such as the Lowell and Malaspina, during the 19th century. These narratives, recorded by ethnographers like John Swanton and Frederica de Laguna, depict glaciers as sentient entities that respond to human behavior with surges or floods. [298]

The historical record of the late Little Ice Age reveals that climatic stress often compounded with other societal shocks, creating devastating feedback loops for vulnerable populations. [42] In northwestern North America, the convergence of environmental hardship and biological catastrophe proved particularly lethal for indigenous communities. [42] The mid-19th century smallpox epidemic, for instance, caused breaks in cultural memory and massive loss of life, forcing survivors to migrate to settlements like Guseix or Neskataheen. [38] This historical baseline establishes that cold periods do not merely lower temperatures; they destabilize the ecological and social foundations upon which human survival depends. [42] For instance, the Kaskawulsh Glacier advanced between 1405/1430 and 1440/1625, leaving spruce logs in its end moraine. [298] In most glacierized regions, the positions of glacier termini have been observed only sporadically for less than a century, meaning that although dominant recession is commonly inferred, data are generally inadequate to construct long and detailed time series. [298] Because minor fluctuations encompassing only a few years may point to important brief climatic reversals, these discontinuous records provide limited information, other than generalized long-term trends. [298] Most data from North America represent sporadic observations of this type, mainly confined to the last hundred years, with the earliest useful observations of Alaskan glacier termini made in the late 18th century, but repetitive surveys of selected glaciers did not begin until the 1930s. [298] By contrast, glacier observations in the European Alps extend back to the early part of the Little Ice Age, where some of the largest, most-accessible glaciers have been observed at frequent intervals since the 17th or 18th centuries. In a few cases, fluctuations of glacier termini during the past 2 centuries have been reconstructed in considerable detail using a combination of written descriptions, drawings, paintings, maps, and photographs. [298] For this reason, and because the Alps lie relatively close to Greenland where the long ice-core acidity record has been obtained, special attention is directed toward the fluctuations of these glaciers. Curves depicting the variations of glaciers in Greenland, Scandinavia, and Iceland commonly contain many fewer control

points than the best Alpine examples and are therefore judged less reliable. [298] In these areas, historical observations have been supplemented by lichenometric dating of recent glacier variations. [298]

9.2 Grid and Energy Resilience

While terrestrial weather and human errors already account for $75-180bn annually in economic costs from power outages, the potential impact of geomagnetic storms represents a catastrophic risk to the infrastructure's core components. [299] These storms are severe disturbances caused by solar storms in the upper layers of our atmosphere that induce currents in long conductors on the Earth's surface, such as power lines. [299] The resulting geomagnetically induced currents can overload the electric grid system to trigger voltage collapse, or worse, damage a significant number of expensive extra-high voltage transformers. [299] This specific mechanism suggests that massive solar storms can severely damage electrical grid components via geomagnetically induced currents. The economic costs of such an event would be catastrophic, particularly because large transformer repairs and replacements occur on the timescale of weeks to months. [299][300][301] Therefore, understanding the likelihood of extreme geomagnetic storms and the specific vulnerabilities of the North American power grid is essential for assessing the regions at highest risk from this complex natural hazard. The implications for the insurance industry and society generally highlight that preparedness must address not just the frequency of outages, but the duration and severity of those caused by the physical destruction of key infrastructure. [299]

The vulnerability of the North American electric grid to geomagnetic storms reveals a critical fragility in modern infrastructure. [299] Severe disturbances caused by solar storms induce currents in long conductors, such as power lines, which can overload the system and damage expensive extra-high voltage transformers. [299] Consequently, the recovery from widespread solar storm damage may take months or years, potentially resulting in long-term widespread blackouts and chronic supply shortages. This prolonged disruption underscores the necessity for robust grid resilience strategies, including the establishment of a national electrical power grid control center to monitor transformers nationwide. [299] [280][302][303] The ability to balance electrical loads from region to region is essential to spare at-risk transformers from destruction during intense geomagnetic storms. [302]

The 2008 Chinese winter storm demonstrates how extreme weather can paralyze transport, causing critical fuel shortages for power plants. Heavy snow and sleet halted coal shipments, leaving reserves at emergency levels sufficient for only eight days of generation. [51][46][50][39][81] This disruption triggered cascading blackouts affecting over thirty million people and created acute water shortages, as city systems require electricity to operate. [51] To prevent similar failures, adequate supplies of fuel, including coal, fuel oil, and LPG, must be stockpiled at electrical generation power plants by September 15 each year. [51] This preparation often necessitates constructing additional storage facilities. [304] Furthermore, the 2008 crisis suggests that extreme winter weather can paralyze transport, causing critical fuel shortages for power plants. Without robust fuel reserves and hardened transmission lines, the electrical grid remains vulnerable to the compounding effects of cold, snow, and logistical collapse. [51][46][50][39][81]

Extreme cold exposes critical vulnerabilities in residential heating systems, particularly when power outages coincide with sub-zero temperatures. [51] Consequently, distributed-generation and microgrid systems offer a vital redundancy, ensuring that local power can keep heating systems operational even if the central grid fails.

The vulnerability of modern infrastructure to electrical failure is starkly illustrated by the cascading impacts on essential services. [305] In urban areas with electrically dependent water infrastructure, electrical outages cause cascading failures in municipal water systems that rely on electricity, a reality that suggests the critical interdependence of these utilities. When the power grid fails, water in many homes would dry up after a few days because municipal water pumps are electric, leading to inoperative sewer systems that spill raw sewerage into rivers and lakes. [305] This dependency suggests that life without electricity for months or years is a major disaster, as the transportation system would be thrown into gridlock and gasoline stations would be unable to pump fuel. [50] The restoration of such systems is slow because most EHV transformers are large, costly items with a manufacture lead-time of a year or more, meaning a massive blackout could extend through many months. [50] Consequently, the threat of a master reset reveals that our technological world is vulnerable, requiring robust preparedness to prevent the loss of essential means of response and recovery during extreme weather events.

The structural integrity of long-distance power transmission systems is inherently compromised by the physics of electrical resistance and current flow. [299] As distance increases, so does the total resistance along each transmission line, while the current carried by the line also increases with distance, meaning the total risk rises with the total path length. [299] Because higher voltage lines offer less resistance, larger currents flow relative to lower voltage lines under identical surface electric fields. [299] Consequently,

grids with low reserve capacity and long transmission lines appear to be significantly more susceptible to equipment damage and widespread blackouts during extreme geomagnetic events. This heightened susceptibility suggests that infrastructure planning must account for these cumulative risks to mitigate potential cascading failures. [305][299][299]

The vulnerability of long-distance transmission lines underscores the need for localized power generation. [306] When high-voltage transformers fail, replacement lead times can stretch from five to sixteen months, leaving regions without power for extended periods. [299] In such scenarios, the modern reliance on electricity for heating means that homes in cold environments will slowly lose heat and become unlivable without power, underscoring the urgent need for backup heat sources that do not depend on the grid. [51] However, the scale of modern energy dependence necessitates a proactive approach to fuel security and backup systems. By integrating lessons from extreme cold weather survival in places like Antarctica and northern Minnesota, societies can better prepare for the significant difficulties, including famines and epidemics, that accompany global cooling. [280] The emphasis on long-term food storage and alternative heating methods reflects a broader strategy of resilience that acknowledges the potential for prolonged periods of severe weather. [50] Ultimately, the ability to withstand these conditions depends on the robustness of energy infrastructure and the preparedness of individuals to adapt to a colder future.

9.3 Food Security and Agriculture

Analysis of extreme impact events suggests that a massive asteroid or comet strike would produce a global catastrophe, where unfavorable weather conditions and acid rain would severely retard food production, processing, and distribution. The infrastructure required to sustain modern populations would take a significant hit, with broken transportation lines inhibiting the movement of grains from processing centers to population hubs. [307][46][280][82][70] This damage to government, finance, communications, and energy systems would place recovery efforts into shambles, leading to starvation and famines in the general population. [307] A weakened population resulting from such starvation becomes vulnerable to disease, epidemics, and plagues, compounding the initial disaster. [253] The Plan de Preparación para el Gran Mínimo Solar highlights that a Grand Solar Minimum produces an era of great difficulties, including significant global cooling, great famines, and great epidemics. [280] Just as humanity survived the last such episode approximately 300 years ago through adaptation, we must prepare for the constraints on agricultural production that a small ice age imposes. [280] The conditions of a small ice age will constrain agricultural production, leading to famines, and necessitating preparation for long-term food storage. [51] Furthermore, great ice and snow storms produce massive cuts in electricity, making alternative heat sources essential. By studying survival methods in extremely cold climates like Fairbanks, Alaska, International Falls, Minnesota, and Antarctica, we can adapt our clothing, travel, and home designs. [280] This adaptation is crucial because the inability to quickly recover from damaged infrastructure leads to widespread suffering. [304] Therefore, understanding these global catastrophic risk scenarios establishes the necessity for robust, decentralized food and energy systems that can withstand both sudden impacts and prolonged climatic shifts. The "Genesis Strategy," as termed by Schneider, proposes building reserves during periods of abundance to survive subsequent famines, a concept echoed by Maher and Baum in the context of global catastrophes. [308] Existing public and private reserves, ranging from FDR's grain reserve to household supplies maintained by groups like the Church of Latter Day Saints, could theoretically support populations for four to seven months. [308] However, this approach suggests that food stockpiles are expensive to pre-catastrophe populations and can actively worsen pre-catastrophe food security by diverting resources from immediate consumption, particularly when built up rapidly in a world where hundreds of millions already face hunger. Furthermore, the sheer scale of potential disruptions, such as volcanic winters lasting years or decades, suggests that stockpiles are at most a partial solution, as it may be infeasible to produce reserves sufficient to feed the global population for such extended periods. Consequently, reliance on stockpiling alone appears insufficient to mitigate long-term risks, suggesting that complementary strategies are likely necessary. [308][77]

The historical record of the 1810s, identified as probably the coldest period in the past five centuries, illustrates how sustained cooling from volcanic eruptions like Tambora and the 1809 Unknown devastated human agriculture and food supply. [77] To mitigate these risks, the Plan de Preparación para el Gran Mínimo Solar emphasizes adaptation strategies observed in extreme cold regions like Fairbanks, Alaska, and the Antarctic. [280] These methods include preparing for long-term food storage and developing alternative heat sources, recognizing that severe cold constrains agricultural production and leads to famine. [280] By studying how individuals survived the last Little Ice Age through changes in clothing, travel, and home design, we can better prepare for the significant difficulties and epidemics associated with future grand solar minima. [280] The primary expense lies not in immediate procurement but in the

research, development, and deployment of alternative food practices that can function when sunlight is blocked. [308] Consequently, food stockpiles should serve only as a temporary stopgap measure while this alternative production infrastructure is scaled up to meet demand. Household grain storage — covered in the preparedness sections of this chapter — rules out reliance on grocery stores, which are insufficient and will be quickly exhausted during large impact events where basic infrastructure is destroyed. [304] This method suggests a viable pathway for extending the shelf life of potatoes and beets by destroying insects and microorganisms while simultaneously preventing sprouting. [215] Furthermore, repeated studies indicate that irradiation cannot mask off-flavors or the smell of spoiled foods, ensuring that safety improvements do not compromise quality. Consequently, resilience requires local self-sufficiency in food, meaning that regions must develop their own capacity for production and distribution. The available options—food stockpiles, traditional agriculture, and foods produced from alternative energy sources—each carry distinct advantages and disadvantages. [308] Stockpiles are versatile but expensive, while agriculture is efficient but less viable in severe catastrophe scenarios. [308] Alternative foods, such as those derived from biomass or fossil fuels, are inexpensive pre-catastrophe but require significant scaling post-catastrophe and may face issues of social acceptability. [308] Therefore, the optimal portfolio typically includes some of each option, adjusted for local constraints. This approach ensures that food supply resilience is integrated into broader risk reduction strategies without attempting to maximize resilience at the expense of other important objectives, including catastrophe prevention. [308] By recognizing that food supply resilience requires not just the food itself but also the accompanying systems of production and distribution, planners can design more robust and adaptable food systems. [308] Ultimately, the goal is to create a flexible and resilient food system that can withstand the shocks of a changing climate, regardless of the specific mechanisms driving that change.

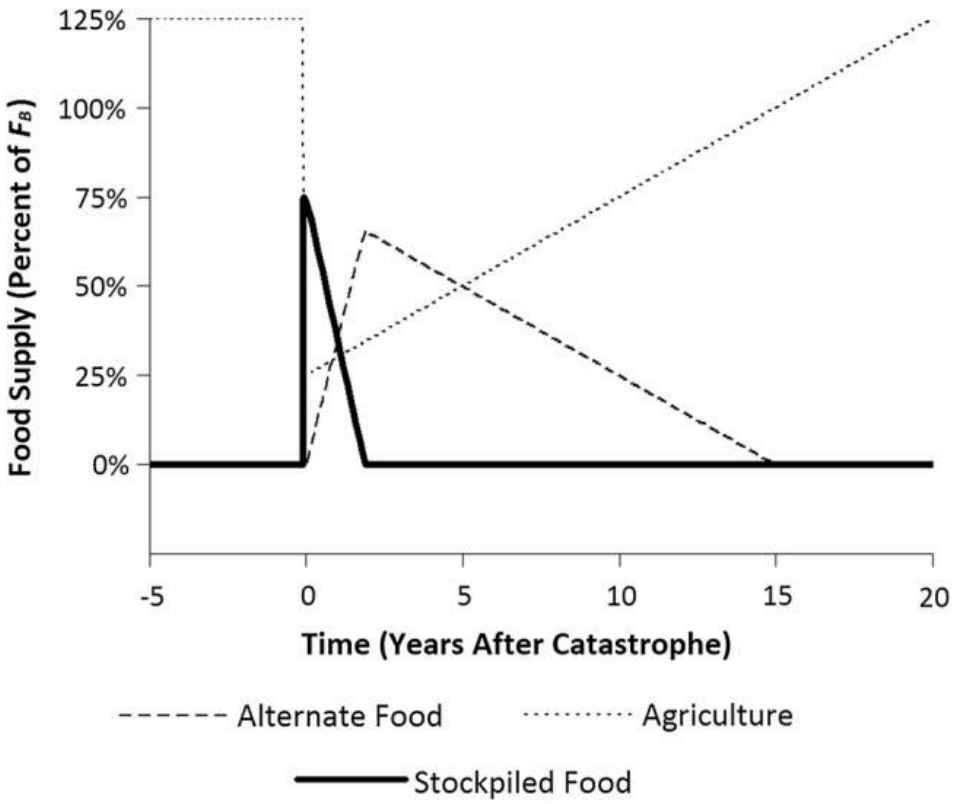

Figure 9.1: The figure displays a line graph showing the percentage of food supply (F_a) over time (years after a catastrophe), illustrating the contributions of stockpiled food, agriculture, and alternative food. Stockpiled food provides 100% of the supply at year 0, then drops to 0% by year 3. Agriculture begins at 0% and increases linearly, surpassing stockpiled food around year 5. Alternative food starts at 0% and rises sharply, exceeding agriculture by year 10. The graph demonstrates the transition from reliance on stored food to sustained production from agriculture and alternative sources in a post-catastrophe scenario. (source: ref 308)

9.4 Water Sanitation and the Built Environment

In regions susceptible to severe winter conditions, maintaining the flow of water through exterior pipe runs is critical for household survival, yet standard insulation alone is often insufficient against temperatures that plunge well below freezing. [51] Evidence from past winter disasters demonstrates that this electric protection fails completely if electricity is lost for several hours during extreme cold, leaving pipes to freeze solid and potentially burst. The consequences of such a failure extend beyond mere discomfort; without water, sanitation systems cease to function, and the inability to flush toilets or manage human waste becomes a severe health hazard. [51][215][306] Furthermore, the loss of power can cause fuel oil to coagulate into a substance resembling Jell-O, rendering furnaces inoperable even after electricity is restored, as seen in documented cases where a one-hour blackout turned into a desperate struggle for warmth. Therefore, any comprehensive preparedness strategy must account for the possibility that electric pipe protection will not suffice, necessitating backup plans for water storage, waste management, and alternative heating sources that do not rely on the grid. To mitigate this, shoveling snow or placing mulch over underground pipe runs can reduce freezing threats, leveraging the insulating properties of fresh snow, which is approximately equal to a six-inch-layer of fiberglass insulation with an R-value of R-19. This simple intervention supports resilience by preventing the clogging of buried fuel oil lines and the shifting of house foundations during Little Ice Age conditions. [51]

The insulation properties of snow are critical for understanding heat retention in extreme cold. [51] Ten inches of fresh fluffy snow provides insulation equivalent to a six-inch layer of fiberglass (R-19). This demonstrates that natural snow cover can significantly mitigate heat loss from buildings, provided the snow remains fresh and contains about 7 percent water. [51] However, historical accounts from severe cold periods reveal that even with thick stone walls, small windows, and constant fires, indoor temperatures could drop so low that ice formed on interior walls and bed-places, requiring daily removal with a hatchet. In modern contexts, a brief power outage during extreme cold can cause fuel oil to coagulate, rendering furnaces useless and turning a minor inconvenience into a life-threatening struggle. [215] Therefore, while snow offers substantial thermal resistance, reliable backup heating systems and robust building envelopes remain essential for survival during prolonged freezing events, ensuring that internal heat is retained when external conditions become hostile. Consequently, households must prepare manual filtration systems and approaches to treat contaminated tap water or surface ground water. Alternatively, filtering large contaminants using bleached cotton cheese cloth and treating the water with liquid bleach can kill dangerous bacteria. [306] Storing several bottles of bleach and a roll of cheesecloth ensures that individuals can disinfect water using 1/4 teaspoon of regular household bleach per gallon, allowing the mixture to sit for 30 minutes before drinking. [306] In such emergencies, boiling water may be impossible if electricity is unavailable, making chemical disinfection a critical survival skill. [306] The available evidence demonstrates that non-scented household bleach can disinfect water by killing dangerous bacteria. This method relies on standard liquid bleach containing between 5 percent and 6 percent chlorine, applied at precise dosages—such as one-quarter teaspoon per gallon—to ensure safety without introducing harmful additives like perfumes or dyes. [306] By storing several bottles of this bleach alongside filtration materials like bleached cotton cheese cloth, individuals can effectively treat contaminated tap water, rainwater, or water from rivers and lakes. [306] Consequently, disaster preparedness plans for prolonged loss of clean water and electricity suggest that manual filtration systems and sanitation systems are recommended for long-term survival without utilities. This approach is consistent with the observation that while vast quantities of water may remain available during a disaster, they are often highly polluted, necessitating independent purification methods such as slow sand filtration or ceramic filters to prevent disease. [304] By integrating these manual systems with grain storage and processing capabilities, individuals can mitigate the risks associated with the destruction of basic infrastructure. [304] Therefore, the implementation of manual water purification and sanitation protocols serves as a critical buffer, ensuring that households maintain hygiene and health even when the broader societal framework fails.

9.5 Household and Regional Preparedness

The threat landscape is not merely theoretical; it encompasses both the catastrophic disruption of a massive solar storm and the prolonged climatic cooling of a Little Ice Age scenario, both of which demand specific, pre-planned responses to mitigate human suffering. [280] The reactive component focuses on the critical window before and immediately after a major solar storm, emphasizing steps such as stockpiling batteries, filling vehicles with gasoline or diesel, securing alternative cooking fuels like charcoal or propane, and ensuring a ninety-day supply of prescription medications. [50] These immediate actions are designed to maintain basic functionality during the acute phase of infrastructure failure. [306] Ultimately,

the goal is to alleviate the misery and hardship that may be encountered, transforming the abstract threat of solar variability into a manageable set of logistical challenges that can be addressed through deliberate, informed action.

Immediate reactive preparations for an imminent major solar storm or electrical blackout establish the necessity of stocking batteries, fuel, cash, water, non-perishable food, and prescription medications. These measures are likely to mitigate the immediate risks associated with prolonged power outages. [50] [280][304] Consequently, individuals may find themselves better prepared to handle the ensuing logistical challenges. Similarly, obtaining a long-term food supply becomes a primary challenge once grocery stores are exhausted, establishing raw grains like corn, wheat, and soybeans as among the most storable bulk food sources for sustaining populations through extended crises. [215] One ton of grain can supply roughly one person's needs for three years, suggesting that, in principle, U.S. grain output could feed its population if protected from damage. [306] Individuals and families are advised to purchase and store grain supplies prior to an impact event, utilizing farm cooperatives and Feed & Grain stores for bulk shipments. [304] Whole corn kernels are recommended over cracked corn to extend shelf life and facilitate cleaning before processing, ensuring that households maintain a reliable caloric intake when traditional supply chains fail. [306]

The Solar Grand Minima Preparedness Plan establishes that individual survival during a Little Ice Age depends on adapting to severe cold, long-term food storage, and alternative heat sources. Historical precedents from Fairbanks, International Falls, and Antarctica demonstrate that adaptation requires changes in clothing, travel, and home design to withstand significant global cooling and famine. [280] At the individual level, preparations must include water storage, treatment, sanitation, and security measures to survive months or years without grid support. [50]

The Plan de Preparación para el Gran Mínimo Solar emphasizes that survival during a small ice age depends on adaptation, drawing lessons from communities in Fairbanks, International Falls, and Antarctica. [280] While government strategies address agriculture and energy, individual resilience requires long-term food storage to counter agricultural constraints and alternative heat sources for massive power outages caused by ice storms. [50] The emphasis on adaptation underscores that personal readiness is not merely optional but essential for navigating the severe climatic difficulties associated with a grand solar minimum. [280]

For households preparing for extended disruptions, securing a durable food supply is paramount, as grocery stores will be quickly exhausted in any large-scale disaster scenario. [51] The most viable long-term food source capable of sustaining individuals is raw grains, particularly corn, which is abundant in the United States and serves as a natural choice for storage due to its high caloric density. [304] This approach eliminates the need for constant food rotation, allowing families to maintain a stable reserve of basic staples like rice, beans, and wheat in metalized bags within Superpails. [51]

Surviving a prolonged solar minimum requires adapting to severe cold and agricultural constraints, much like the historical precedents of the Dalton and Maunder eras. [297] This necessitates a reevaluation of food preservation techniques that can withstand long-term storage without relying on continuous refrigeration or complex supply chains. [51] Furthermore, this approach supports the broader argument that every preparedness action, from building-envelope retrofits to indoor-agriculture scaling, enhances resilience to extreme weather of any kind, regardless of the ultimate climate driver. Ultimately, the adoption of irradiation and other preservation technologies is consistent with the goal of closing the resilience gap that government action cannot fill in time, ensuring that communities are equipped to handle the sustained sub-zero conditions predicted by solar minimum forecasts.

9.6 The Precautionary Closing Argument

The precautionary principle, introduced at the outset of this inquiry, demands that we act on the potential for severe disruption even when probabilities are uncertain. [28] Therefore, the recommendations here are not speculative hedging but essential upgrades to our collective immune system. Thus, every step taken to improve resilience—whether it is installing current-blocking capacitors on the grid or storing water and food at the household level—serves as a buffer against the unknown.

Remember where this book began: on the ice of the Thames, in the winters when the river froze solid for two months and Londoners walked upon it; when John Evelyn swore no man alive had known England so cold; when an army marched across a frozen sea. That world was not a fable, and it was not long ago. It was simply the last time the Sun went quiet — and the people it caught hardest were the ones who had forgotten that cold was possible. The quiet Sun is returning on its own schedule, indifferent to our committees and our forecasts. The goal is not to fear the cold, but to respect it, and to build a society that can withstand it. [51] The time for debate is over; the time for preparation is now. [46]

References

1. Vinós, J. (2022). Climate of the Past, Present and Future.

2. Ljungqvist, F.C. (2010). A new reconstruction of temperature variability in the extra-tropical northern hemisphere during the last two millennia. https://doi.org/10.1111/j.1468-0459.2010.00399.x

3. Diaz, H.F., et al. (2011). Spatial and Temporal Characteristics of Climate in Medieval Times Revisited. https://doi.org/10.1175/bams-d-10-05003.1

4. Mackay, H., et al. (2022). The 852/3 CE Mount Churchill eruption: examining the potential climatic and societal impacts and the timing of the Me…. https://doi.org/10.5194/cp-2021-170

5. Hyland, K. (1998). Hedging in Scientific Research Articles. https://doi.org/10.1075/pbns.54

6. Tardif, R., et al. (2019). Last Millennium Reanalysis with an expanded proxy database and seasonal proxy modeling. https://doi.org/10.5194/cp-15-1251-2019

7. Heiss, K.P. (2007). Global Warming – Global Winter - What sayeth the Data: Open Questions and New Theories.

8. EASTERBROOK, D.J. (2011). Evidence-Based Climate Science. https://doi.org/10.1016/c2010-0-67154-9

9. Berry (2023). Edwin X Berry. https://doi.org/10.53234/scc2023xx/xx

10. Beck, E.G. (2008). Evidence of Variability of Atmospheric CO2 Concentration During the 20th Century.

11. Valentina, V.I.Z. (2023). Links of Terrestrial Volcanic Eruptions to Solar Activity and Solar Magnetic Field.

12. Kakad, B., et al. (2019). Diminishing activity of recent solar cycles (22–24) and their impact on geospace. https://doi.org/10.1051/swsc/2018048

13. Cameron, R.H., Jiang, J., & Schüssler, M. (2016). Solar Cycle 25: Another Moderate Cycle?. https://doi.org/10.3847/2041-8205/823/2/l22

14. Zharkova, V. (2020). Modern Grand Solar Minimum will lead to terrestrial cooling. https://doi.org/10.1080/23328940.2020.1796243

15. Zharkova, V.V., et al. (2023). Periodicities of solar activity and solar radiation derived from observations and their links with the terrestrial en…. https://doi.org/10.48550/arxiv.2301.07480

16. Abdussamatov, H. (2016). The New Little Ice Age Has Started. https://doi.org/10.1016/b978-0-12-804588-6.00017-3

17. Abdussamatov, H.I. (2010). The Additional Criterion for the Determination of the Time of Minimum of a Solar Cycle. https://doi.org/10.4236/jemaa.2010.23019

18. Jager, C.D. (2012). Solar Forcing of Climate. https://doi.org/10.1007/978-94-007-4327-4_9

19. Yndestad, H. (2020). The Kola Temperature variability.

20. Krivova, N.A., Vieira, L.E.A., & Solanki, S.K. (2010). Reconstruction of solar spectral irradiance since the Maunder minimum. https://doi.org/10.1029/2010ja015431

21. Sharp, G.J. (2013). Are Uranus & Neptune Responsible for Solar Grand Minima and Solar Cycle Modulation?. https://doi.org/10.4236/ijaa.2013.33031

22. Lightfoot, H.D., & Ratzer, G. (2022). The Sun Versus CO2 as the Cause of Climate Change Projected to 2050. https://doi.org/10.29169/1927-5129.2022.18.03

23. Herrera, V.V., Soon, W., & Legates, D. (2021). Does Machine Learning reconstruct missing sunspots and forecast a new solar minimum?. https://doi.org/10.1016/j.asr.2021.03.023

24. Ruzmaikin, A., & Feynman, J. (2015). The Earth's climate at minima of Centennial Gleissberg Cycles. https://doi.org/10.1016/j.asr.2015.07.010

25. White, S., et al. (2022). The 1600 CE Huaynaputina eruption as a possible trigger for persistent cooling in the North Atlantic region. https://doi.org/10.5194/cp-18-739-2022

26. Moreno-Chamarro, E., et al. (2016). An abrupt weakening of the subpolar gyre as trigger of Little Ice Age-type episodes. https://doi.org/10.1007/s00382-016-3106-7

27. Dai, Z., et al. (2022). Atlantic Multidecadal Variability Response to External Forcing during the Past Two Millennia. https://doi.org/10.1175/jcli-d-21-0986.1

28. Jehn, F.U., et al. (2022). Focus of the IPCC Assessment Reports Has Shifted to Lower Temperatures. https://doi.org/10.1029/2022ef002876

29. Usoskin, I.G., et al. (2015). The Maunder minimum (1645–1715) was indeed a grand minimum: A reassessment of multiple datasets. https://doi.org/10.1051/0004-6361/201526652

30. Lean, J., Beer, J., & Bradley, R. (2007). Reconstruction of solar irradiance since 1610 Implications for climate change.

31. Stuiver, M., Grootes, P.M., & Braziunas, T.F. (1995). The GISP2 δ18O Climate Record of the Past 16,500 Years and the Role of the Sun, Ocean, and Volcanoes. https://doi.org/10.1006/qres.1995.1079

32. Heikkilä, U., Beer, J., & Feichter, J. (2008). Modeling cosmogenic radionuclides 10 Be and 7 Be during the Maunder Minimum using the ECHAM5-HAM General Circulation …. https://doi.org/10.5194/acp-8-2797-2008

33. Field, C.V., Schmidt, G.A., & Shindell, D.T. (2009). Interpreting 10Be changes during the Maunder Minimum. https://doi.org/10.1029/2008jd010578

34. Zolotova, N., & Vokhmyanin, M. (2025). Long-Lived Sunspots in Historical Records: A Case Study Analysis from 1660 to 1676. https://doi.org/10.1007/s11207-025-02432-0

35. V.V, Z., & ShepherdS., J. (2020). Erratum - baseline magnetic field oscillations: possible SIM effects on solar irradiance and temperature at Earth.

36. Scherer, K., & Fichtner, H. (2003). Constraints on the heliospheric magnetic field variation during the Maunder Minimum from cosmic ray modulation modelling. https://doi.org/10.1051/0004-6361:20034636

37. Eddy, J.A. (1976). The Maunder Minimum. https://doi.org/10.1126/science.192.4245.1189

38. Parker, G. (2017). Global Crisis.

39. Marusek, J. (2014). A Chronological Listing of Early Weather Events.

40. Huhtamaa, H., & Helama, S. (2017). Distant impact: tropical volcanic eruptions and climate-driven agricultural crises in seventeenth-century Ostrobothni…. https://doi.org/10.1016/j.jhg.2017.05.011

41. Parker's, G. (2017). Global Crisis: War, Climate Change and Catastrophe in the Seventeenth Century.

42. Degroot, D. (2018). Climate change and society in the 15th to 18th centuries. https://doi.org/10.1002/wcc.518

43. Usoskin, I.G. (2017). A history of solar activity over millennia. https://doi.org/10.1007/s41116-017-0006-9

44. Augustson, K., et al. (2015). Grand Minima and Equatorward Propagation in a Cycling Stellar Convective Dynamo. https://doi.org/10.1088/0004-637x/809/2/149

45. Rind, D., et al. (2004). The Relative Importance of Solar and Anthropogenic Forcing of Climate Change between the Maunder Minimum and the Present. https://doi.org/10.1175/1520-0442(2004)017%3C0906:triosa%3E2.0.co;2

46. Casey, J.L. (2016). Dark Winter: How the Sun Is Causing a 30-Year Cold Spell.

47. Lightfoot, H.D., & Ratzer, G. (2025). Significant Errors Identified in the IPCC Reports. https://doi.org/10.29169/1927-5129.2025.21.18

48. Shanmugam, G. (1864). 200 Years of Fossil Fuels and Climate Change (1900-2100). https://doi.org/10.1080/14786446408643701

49. Schiermeier, Q. (2013). IPCC: The climate chairman. https://doi.org/10.1038/501303a

50. Marusek, J. (2010). The Sun is Undergoing a State Change.

51. James, P. (2004). Plan, Plan, Plan. https://doi.org/10.1007/978-1-4615-0473-3_1

52. Steinhilber, F., et al. (2012). 9,400 Years of Cosmic Radiation and Solar Activity from Ice Cores and Tree Rings. https://doi.org/10.1073/pnas.1118965109

53. Baroni, M., et al. (2011). Volcanic and solar activity, and atmospheric circulation influences on cosmogenic 10Be fallout at Vostok and Concordi…. https://doi.org/10.1016/j.gca.2011.09.002

54. Sturevik-Storm, A., et al. (2014). 10Be climate fingerprints during the Eemian in the NEEM ice core, Greenland. https://doi.org/10.1038/srep06408

55. Vonmoos, M., Beer, J., & Muscheler, R. (2006). Large variations in Holocene solar activity: Constraints from 10Be in the Greenland Ice Core Project ice core. https://doi.org/10.1029/2005ja011500

56. Duhau, S., & Jager, C.D. (2008). The Solar Dynamo and Its Phase Transitions during the Last Millennium. https://doi.org/10.1007/s11207-008-9212-x

57. Willenbring, J.K., & Blanckenburg, F.V. (2010). Meteoric cosmogenic Beryllium-10 adsorbed to river sediment and soil: Applications for Earth-surface dynamics. https://doi.org/10.1016/j.earscirev.2009.10.008

58. Clette, F., et al. (2014). Revisiting the Sunspot Number. https://doi.org/10.1007/s11214-014-0074-2

59. Pedro, J.B., et al. (2011). High-resolution records of the beryllium-10 solar activity proxy in ice from Law Dome, East Antarctica: measurement, …. https://doi.org/10.5194/cp-7-707-2011

60. Svensmark, H. (2019). The Sun's Role in Climate Change.

61. Solanki, S.K., et al. (2004). Unusual activity of the Sun during recent decades compared to the previous 11,000 years. https://doi.org/10.1038/nature02995

62. Fairbridge, R.W., & Shirley, J.H. (1987). Prolonged minima and the 179-yr cycle of the solar inertial motion. https://doi.org/10.1007/bf00148211

63. Delaygue, G., & Bard, E. (2011). An Antarctic view of Beryllium-10 and solar activity for the past millennium. https://doi.org/10.1007/s00382-010-0795-1

64. Dee, M., et al. (2025). Radiocarbon evidence over the apparent grand solar minimum around 400 BCE. https://doi.org/10.1017/rdc.2024.132

65. Pearson, C.L., et al. (2021). Dendrochronology and Radiocarbon Dating. https://doi.org/10.1017/rdc.2021.97

66. Charvátová, I. (2000). Can Origin of the 2400-Year Cycle of Solar Activity Be Caused by Solar Inertial Motion?. https://doi.org/10.1007/s00585-000-0399-x

67. Heaton, T.J., et al. (2024). Extreme solar storms and the quest for exact dating with radiocarbon. https://doi.org/10.1038/s41586-024-07679-4

68. Kataoka, R., & Nakano, S. (2021). Auroral zone over the last 3000 years. https://doi.org/10.1051/swsc/2021030

69. Silverman, S.M., & Hayakawa, H. (2021). The Dalton Minimum and John Dalton's Auroral Observations. https://doi.org/10.1051/swsc/2020082

70. Rampino, M.R., et al. (2002). Volcanic Winters.

71. Langmann, B. (2015). On the Role of Climate Forcing by Volcanic Sulphate and Volcanic Ash.

72. Raible, C.C., et al. (2016). Tambora 1815 as a test case for high impact volcanic eruptions: Earth system effects. https://doi.org/10.1002/wcc.407

73. Briffa, K.R., et al. (1998). Influence of volcanic eruptions on Northern Hemisphere summer temperature over the past 600 years. https://doi.org/10.1038/30943

74. Stothers, R.B. (1984). The great Tambora eruption in 1815 and its aftermath. https://doi.org/10.1016/0198-0254(84)93639-2

75. D'Arrigo, R., Wilson, R., & Tudhope, A. (2008). The impact of volcanic forcing on tropical temperatures during the past four centuries. https://doi.org/10.1038/ngeo393

76. Oppenheimer, C. (2011). Eruptions that Shook the World. https://doi.org/10.1017/cbo9780511978012

77. Wood, G.D. (2019). X Contents.

78. Mactaggart, M. (2002). Blast from the past. https://doi.org/10.1093/combul/44.2.20

79. Anet, J.G., et al. (2014). Impact of solar versus volcanic activity variations on tropospheric temperatures and precipitation during the Dalton …. https://doi.org/10.5194/cp-10-921-2014

80. Schmutz, W.K. (2021). Changes in the Total Solar Irradiance and climatic effects. https://doi.org/10.1051/swsc/2021016

81. Sigg, E. (2011). New England. https://doi.org/10.1017/cbo9780511973673.003

82. Marusek, J. (2009). EPA Comments.

83. O'Reilly, J. (2017). Just Over the Horizon. https://doi.org/10.1016/b978-0-12-803863-5.00014-5

84. Slawinska, J., & Robock, A. (2018). Impact of Volcanic Eruptions on Decadal to Centennial Fluctuations of Arctic Sea Ice Extent during the Last Millenniu…. https://doi.org/10.1175/jcli-d-16-0498.1

85. Preiser-Kapeller, J. (2024). The Medieval Climate Anomaly, the Oort Minimum, and Socio-Political Dynamics in the Eastern Mediterranean and the Byz…. https://doi.org/10.1163/9789004689350_017

86. Kushnir, Y., & Stein, M. (2019). Medieval Climate in the Eastern Mediterranean: Instability and Evidence of Solar Forcing. https://doi.org/10.3390/atmos10010029

87. Consortium, P. (2013). Continental-scale temperature variability during the past two millennia. https://doi.org/10.1038/ngeo1797

88. Xing, P., et al. (2016). The Extratropical Northern Hemisphere Temperature Reconstruction during the Last Millennium Based on a Novel Method. https://doi.org/10.1371/journal.pone.0146776

89. Martin-Puertas, C., et al. (2012). Regional atmospheric circulation shifts induced by a grand solar minimum. https://doi.org/10.1038/ngeo1460

90. Izdebski, A., Mordechai, L., & White, S. (2018). The Social Burden of Resilience: A Historical Perspective. https://doi.org/10.1007/s10745-018-0002-2

91. Chiodo, G., et al. (2016). The impact of a future solar minimum on climate change projections in the Northern Hemisphere. https://doi.org/10.1088/1748-9326/11/3/034015

92. Maycock, A.C., et al. (2015). Possible impacts of a future grand solar minimum on climate: Stratospheric and global circulation changes. https://doi.org/10.1002/2014jd022022

93. Scafetta, N., & Willson, R.C. (2014). ACRIM total solar irradiance satellite composite validation versus TSI proxy models. https://doi.org/10.1007/s10509-013-1775-9

94. Choudhury, P.K., & El-Nasr, M.A. (2021). Invited reviews. https://doi.org/10.1080/09205071.2014.937931

95. Marsh, N.D., & Svensmark, H. (2000). Low Cloud Properties Influenced by Cosmic Rays. https://doi.org/10.1103/physrevlett.85.5004

96. Svensmark, H., & Friis-Christensen, E. (1997). Variation of cosmic ray flux and global cloud coverage—a missing link in solar-climate relationships. https://doi.org/10.1016/s1364-6826(97)00001-1

97. Porter, S.C. (1986). Pattern and Forcing of Northern Hemisphere Glacier Variations During the Last Millennium. https://doi.org/10.1016/0033-5894(86)90082-7

98. McConnell, J.R., et al. (2020). Extreme climate after massive eruption of Alaska's Okmok volcano in 43 BCE and effects on the late Roman Republic and…. https://doi.org/10.1073/pnas.2002722117/-/dcsupplemental

99. Nemeth, K., Cronin, S.J., & White, J.D. (2007). Kuwae Caldera and Climate Confusion. https://doi.org/10.2174/1874629007010100 07

100. Palmer, A.S., et al. (2001). High-precision dating of volcanic events (A.D. 1301–1995) using ice cores from Law Dome, Antarctica. https://doi.org/10.1029/2001jd000330

101. Plummer, C.T., et al. (2012). An independently dated 2000-yr volcanic record from Law Dome, East Antarctica, including a new perspective on the dat…. https://doi.org/10.5194/cp-8-1929-2012

102. Maunder, E.W. (1894). A Prolonged Sunspot Minimum. https://doi.org/10.1038/scientificamerican09011894-15569bsupp

103. Hayakawa, H., et al. (2021). Daniel Mögling's Sunspot Observations in 1626–1629: A Manuscript Reference for the Solar Activity before the Maunder …. https://doi.org/10.3847/1538-4357/abdd34

104. Usoskin, I.G. (2023). A history of solar activity over millennia. https://doi.org/10.1007/s41116-023-00036-z

105. Zolotova, N.V., & Ponyavin, D.I. (2016). How Deep Was the Maunder Minimum?. https://doi.org/10.1007/s11207-016-0908-z

106. Usoskin, I.G. (2013). A History of Solar Activity over Millennia. https://doi.org/10.12942/lrsp-2013-1

107. Vaquero, J., & Trigo, R. (2015). Redefining the limit dates for the Maunder Minimum. https://doi.org/10.1016/j.newast.2014.06.002

108. Svalgaard, L., & Schatten, K.H. (2016). Reconstruction of the Sunspot Group Number: The Backbone Method. https://doi.org/10.1007/s11207-015-0815-8

109. Svalgaard, L. (2021). Several Populations of Sunspot Group Numbers – Resolving a Conundrum. https://doi.org/10.5194/egusphere-egu21-282

110. Svalgaard, L. (2013). Solar activity – past, present, future. https://doi.org/10.1051/swsc/2013046

111. Biswas, A., et al. (2023). Long-Term Modulation of Solar Cycles. https://doi.org/10.1007/s11214-023-00968-w

112. Shapiro, A.V., et al. (2020). Solar-cycle irradiance variations over the last four billion years. https://doi.org/10.1051/0004-6361/201937128

113. Potgieter, M. (2013). Solar Modulation of Cosmic Rays. https://doi.org/10.12942/lrsp-2013-3

114. McDonald, F.B., Webber, W.R., & Reames, D.V. (2010). Unusual time histories of galactic and anomalous cosmic rays at 1 AU over the deep solar minimum of cycle 23/24. https://doi.org/10.1029/2010gl044218

115. Vecchio, A., et al. (2019). Solar activity cycles and grand minima occurrence. https://doi.org/10.1393/ncc/i2019-19015-0

116. Cameron, R.H., & Schüssler, M. (2017). Understanding Solar Cycle Variability. https://doi.org/10.3847/1538-4357/aa767a

117. Scafetta, N. (2012). Multi-scale harmonic model for solar and climate cyclical variation throughout the Holocene based on Jupiter–Saturn t…. https://doi.org/10.1016/j.jastp.2012.02.016

118. Jasinski, J.M., & Velli, M. (2025). The Sun Reversed Its Decades-long Weakening Trend in 2008. https://doi.org/10.3847/2041-8213/adf3a6

119. Stefani, F., et al. (2020). Schwabe, Gleissberg, Suess-de Vries: Towards a consistent model of planetary synchronization of solar cycles. https://doi.org/10.22364/mhd.56.2-3.18

120. Popova, E., Zharkova, V., & Zharkov, S. (2013). Probing latitudinal variations of the solar magnetic field in cycles 21–23 by Parker's Two-Layer Dynamo Model with me…. https://doi.org/10.5194/angeo-31-2023-2013

121. McIntosh, S.W., et al. (2022). Uniting the Sun's Hale magnetic cycle and "extended solar cycle" paradigms. https://doi.org/10.3389/fspas.2022.923049

122. Hathaway, D.H. (2015). The Solar Cycle. https://doi.org/10.1007/lrsp-2015-4

123. Petrovay, K. (2020). Solar cycle prediction. https://doi.org/10.1007/s41116-020-0022-z

124. Obridko, V.N., Shibalova, A.S., & Sokoloff, D.D. (2023). The extended solar cycle and asymmetry of the large-scale magnetic field. https://doi.org/10.1093/mnras/stad1515

125. Norton, A., et al. (2023). Solar Cycle Observations. https://doi.org/10.1007/s11214-023-01008-3

126. Leussu, R., et al. (2016). Properties of sunspot cycles and hemispheric wings since the 19th century. https://doi.org/10.1051/0004-6361/201628335

127. Petrie, G.J.D. (2015). Solar Magnetism in the Polar Regions. https://doi.org/10.1007/lrsp-2015-5

128. Demetrescu, C., & Dobrica, V. (2008). Signature of Hale and Gleissberg solar cycles in the geomagnetic activity. https://doi.org/10.1029/2007ja012570

129. Berdyugina, S.V., & Usoskin, I.G. (2003). Active longitudes in sunspot activity: Century scale persistence. https://doi.org/10.1051/0004-6361:20030748

130. Svalgaard, L., & Kamide, Y. (2012). Asymmetric Solar Polar Field Reversals. https://doi.org/10.1088/0004-637x/763/1/23

131. Zhang, L., Mursula, K., & Usoskin, I. (2013). Consistent long-term variation in the hemispheric asymmetry of solar rotation. https://doi.org/10.1051/0004-6361/201220693

132. Zolotova, N.V., & Ponyavin, D.I. (2007). Was the unusual solar cycle at the end of the XVIII century a result of phase asynchronization?. https://doi.org/10.1051/0004-6361:20077681

133. Vecchio, A., et al. (2017). Connection between solar activity cycles and grand minima generation. https://doi.org/10.1051/0004-6361/201629758

134. Charbonneau, P. (2001). Multiperiodicity, Chaos, and Intermittency in a Reduced Model of the Solar Cycle. https://doi.org/10.1023/a:1010387509792

135. Svalgaard, L., Cagnotti, M., & Cortesi, S. (2017). The Effect of Sunspot Weighting. https://doi.org/10.1007/s11207-016-1024-9

136. Svalgaard, L. (2016). A Recount of Sunspot Groups on Staudach's Drawings. https://doi.org/10.1007/s11207-016-1023-x

137. Clette, F., et al. (2023). Recalibration of the Sunspot-Number: Status Report. https://doi.org/10.1007/s11207-023-02136-3

138. Wu, C.J., et al. (2018). Solar total and spectral irradiance reconstruction over the last 9000 years. https://doi.org/10.1051/0004-6361/201832956

139. Soon, W., Connolly, R., & Connolly, M. (2015). Re-evaluating the role of solar variability on Northern Hemisphere temperature trends since the 19th century. https://doi.org/10.1016/j.earscirev.2015.08.010

140. Kopp, G. (2025). Solar irradiance measurements. https://doi.org/10.1007/s41116-025-00040-5

141. Butler, J.J., et al. (2008). Sources of Differences in On-Orbital Total Solar Irradiance Measurements and Description of a Proposed Laboratory Int.... https://doi.org/10.6028/jres.113.014

142. Finsterle, W., et al. (2021). The total solar irradiance during the recent solar minimum period measured by SOHO/VIRGO. https://doi.org/10.1038/s41598-021-87108-y

143. Chatzistergos, T., Krivova, N.A., & Yeo, K.L. (2023). Long-term changes in solar activity and irradiance. https://doi.org/10.1016/j.jastp.2023.106150

144. Abdussamatov, H.I. (2012). Bicentennial Decrease of the Total Solar Irradiance Leads to Unbalanced Thermal Budget of the Earth and the Little Ic.... https://doi.org/10.5539/apr.v4n1p178

145. Liu, L., et al. (2011). Solar activity effects of the ionosphere: A brief review. https://doi.org/10.1007/s11434-010-4226-9

146. Jurdana-Šepić, R., et al. (2011). A relationship between the solar rotation and activity in the period 1998–2006 analysed by tracing small bright coron.... https://doi.org/10.1051/0004-6361/201014357

147. Usoskin, I.G., Solanki, S.K., & Kovaltsov, G.A. (2007). Grand Minima and Maxima of Solar Activity: New Observational Constraints. https://doi.org/10.1051/0004-6361:20077704

148. Cnossen, I., & Matzka, J. (2016). Changes in solar quiet magnetic variations since the Maunder Minimum: A comparison of historical observations and mod.... https://doi.org/10.1002/2016ja023211

149. Jian, L., Russell, C., & Luhmann, J. (2012). Comparing Solar Minimum 23/24 with Historical Solar Wind Records at 1 AU. https://doi.org/10.1007/s11207-011-9737-2

150. Zharkova, V.V., et al. (2015). Heartbeat of the Sun from Principal Component Analysis and prediction of solar activity on a millenium timescale. https://doi.org/10.1038/srep15689

151. Zharkova, V., et al. (2018). Reply to comment on the paper " on a role of quadruple component of magnetic field in defining solar activity in gran.... https://doi.org/10.1016/j.jastp.2017.09.019

152. Shepherd, S.J., Zharkov, S.I., & Zharkova, V.V. (2014). Prediction of Solar Activity from Solar Background Magnetic Field Variations in Cycles 21-23. https://doi.org/10.1088/0004-637x/795/1/46

153. Zharkova, V.V., Shepherd, S.J., & Zharkov, S.I. (2012). Principal component analysis of background and sunspot magnetic field variations during solar cycles 21-23. https://doi.org/10.1111/j.1365-2966.2012.21436.x

154. Scherrer, P.H., et al. (1977). The mean magnetic field of the Sun: Observations at Stanford. https://doi.org/10.1007/bf00159925

155. Ambastha, A. (2020). Solar Magnetic Field and Activity Cycles. https://doi.org/10.1201/9781003005674-4

156. Vasilieva, & Zharkova (2022). Terrestrial volcanic eruptions and their possible links with solar activity.

157. Zharkova, V.V., et al. (2019). RETRACTED ARTICLE: Oscillations of the baseline of solar magnetic field and solar irradiance on a millennial timescale. https://doi.org/10.1038/s41598-019-45584-3

158. Lockwood, M. (2003). Twenty-three cycles of changing open solar magnetic flux. https://doi.org/10.1029/2002ja009431

159. Obridko, V.N., et al. (2021). Solar large-scale magnetic field and cycle patterns in solar dynamo. https://doi.org/10.1093/mnras/stab1062

160. Zharkova, V.V., et al. (2023). Comparison of solar activity proxies: eigenvectors versus averaged sunspot numbers. https://doi.org/10.1093/mnras/stad1001

161. Zharkova, V.V., et al. (2017). Reinforcing a Double Dynamo Model with Solar-Terrestrial Activity in the Past Three Millennia. https://doi.org/10.1017/s1743921317010912

162. Zharkova, V. (2021). Millennial Oscillations of Solar Irradiance and Magnetic Field in 600–2600. https://doi.org/10.5772/intechopen.96450

163. Popova, E., et al. (2018). On a role of quadruple component of magnetic field in defining solar activity in grand cycles. https://doi.org/10.1016/j.jastp.2017.05.006

164. McIntosh, S.W., & Leamon, R.J. (2015). Deciphering solar magnetic activity: on grand minima in solar activity. https://doi.org/10.3389/fspas.2015.00002

165. Muscheler, R., et al. (2007). Solar activity during the last 1000 yr inferred from radionuclide records. https://doi.org/10.1016/j.quascirev.2006.07.012

166. Beer, J., Tobias, S., & Weiss, N. (1998). An Active Sun Throughout the Maunder Minimum. https://doi.org/10.1023/a:1005026001784

167. Owens, M.J., Usoskin, I., & Lockwood, M. (2012). Heliospheric modulation of galactic cosmic rays during grand solar minima: Past and future variations. https://doi.org/10.1029/2012gl053151

168. Brandenburg, A., & Spiegel, E. (2008). Modeling a Maunder minimum. https://doi.org/10.1002/asna.200810973

169. Zharkova, P.V. (2020). Solar Activity, Solar Irradiance and Earth's Temperature.

170. VASILIEVA, I., & ZHARKOVA, V.V. (2022). Terrestrial Volcanic Eruptions and Their Possible Links with Solar Activity.

171. Rahmanifard, F., et al. (2022). Evidence From Galactic Cosmic Rays That the Sun Has Likely Entered a Secular Minimum in Solar Activity. https://doi.org/10.1029/2021sw002796

172. Abreu, J.A., et al. (2008). For how long will the current grand maximum of solar activity persist?. https://doi.org/10.1029/2008gl035442

173. Brajša, R., et al. (2009). On solar cycle predictions and reconstructions. https://doi.org/10.1051/0004-6361:200810862

174. Jiang, J., Chatterjee, P., & Choudhuri, A.R. (2007). Solar activity forecast with a dynamo model. https://doi.org/10.1111/j.1365-2966.2007.12267.x

175. McIntosh, S.W., et al. (2020). Overlapping Magnetic Activity Cycles and the Sunspot Number: Forecasting Sunspot Cycle 25 Amplitude. https://doi.org/10.1007/s11207-020-01723-y

176. Mörner, N.A. (2015). The Approaching New Grand Solar Minimum and Little Ice Age Climate Conditions. https://doi.org/10.4236/ns.2015.711052

177. Lockwood, M. (2009). Solar change and climate: an update in the light of the current exceptional solar minimum. https://doi.org/10.1098/rspa.2009.0519

178. Karak, B.B. (2010). Importance of Meridional Circulation in Flux Transport Dynamo: The Possibility of a Maunder-Like Grand Minimum. https://doi.org/10.1088/0004-637x/724/2/1021

179. Nandy, D., et al. (2021). Solar evolution and extrema: current state of understanding of long-term solar variability and its planetary impacts. https://doi.org/10.1186/s40645-021-00430-x

180. Sokoloff, D., et al. (2009). Sunspot cycles and Grand Minima. https://doi.org/10.1017/s1743921309992511

181. Inceoglu, F., Arlt, R., & Rempel, M. (2018). The Nature of Grand Minima and Maxima from Fully Nonlinear Flux Transport Dynamos. https://doi.org/10.3847/1538-4357/aa8d68

182. Zaqarashvili, T.V., et al. (2015). Long-Term Variation in the Sun's Activity Caused by Magnetic Rossby Waves in the Tachocline. https://doi.org/10.1088/2041-8205/805/2/l14

183. Cionco, R.G., & Soon, W. (2015). A phenomenological study of the timing of solar activity minima of the last millennium through a physical modeling of.... https://doi.org/10.1016/j.newast.2014.07.001

184. Siversky, T.V., & Zharkova, V.V. (2009). Stationary and impulsive injection of electron beams in converging magnetic field. https://doi.org/10.1051/0004-6361/200912341

185. Zharkova, V.V., et al. (2011). Recent Advances in Understanding Particle Acceleration Processes in Solar Flares. https://doi.org/10.1007/s11214-011-9803-y

186. Zharkova, V. (2012). Electron and Proton Kinetics and Dynamics in Flaring Atmospheres.

187. Matthews, S.A., Zharkov, S., & Zharkova, V.V. (2011). Anatomy of a Solar Flare: Measurements of the 2006 December 14 X-Class Flare with Gong,hinode, Andrhessi. https://doi.org/10.1088/0004-637x/739/2/71

188. Perminov, A., & Kuznetsov, E. (2020). The orbital evolution of the Sun–Jupiter–Saturn–Uranus–Neptune system on long time scales. https://doi.org/10.1007/s10509-020-03855-w

189. Perminov, A.S., & Kuznetsov, E.D. (2018). Orbital Evolution of the Sun–Jupiter–Saturn–Uranus–Neptune Four-Planet System on Long-Time Scales. https://doi.org/10.1134/s0038094618010070

190. Perminov, A.S., & Kuznetsov, E.D. (2019). The Implementation of Hori–Deprit Method to the Construction Averaged Planetary Motion Theory by Means of Computer Al…. https://doi.org/10.1007/s11786-019-00441-4

191. Jeans., J.H. (1925). A Theory of Stellar Evolution. https://doi.org/10.1093/mnras/85.9.914

192. Gustavo (2012). Cionco-Compagnucci-R-man-fig.captions-R. https://doi.org/10.1016/j.asr.2012.07.013

193. Vasilyev, V., et al. (2024). Sun-like stars produce superflares roughly once per century. https://doi.org/10.1126/science.adl5441

194. Hudson, H.S. (2021). Carrington Events. https://doi.org/10.1146/annurev-astro-112420-023324

195. Cionco, R.G., & Pavlov, D.A. (2018). Solar barycentric dynamics from a new solar-planetary ephemeris. https://doi.org/10.1051/0004-6361/201732349

196. Nielsen, M.L., & Kjeldsen, H. (2011). Is Cycle 24 the Beginning of a Dalton-Like Minimum?. https://doi.org/10.1007/s11207-011-9733-6

197. Cionco, R.G., & Compagnucci, R.H. (2011). A new imminent grand minimum?. https://doi.org/10.1017/s1743921312005169

198. Scafetta, N. (2013). Solar and Planetary Oscillation Control on Climate Change: Hind-Cast, Forecast and a Comparison with the Cmip5 Gcms. https://doi.org/10.1260/0958-305x.24.3-4.455

199. Usoskin, I.G., Solanki, S.K., & Kovaltsov, G.A. (2011). Grand minima of solar activity during the last millennia. https://doi.org/10.1017/s174392131200511x

200. Usoskin, I.G., Solanki, S.K., & Kovaltsov, G.A. (2007). Grand minima and maxima of solar activity: new observational constraints. https://doi.org/10.1051/0004-6361:20077704

201. Inceoglu, F., et al. (2015). Grand solar minima and maxima deduced from10Be and14C: magnetic dynamo configuration and polarity reversal. https://doi.org/10.1051/0004-6361/201424212

202. Shaviv, N.J. (2003). The spiral structure of the Milky Way, cosmic rays, and ice age epochs on Earth. https://doi.org/10.1016/s1384-1076(02)00193-8

203. Mörner, N.A. (2010). Solar Minima, Earth's rotation and Little Ice Ages in the past and in the future. https://doi.org/10.1016/j.gloplacha.2010.01.004

204. Stothers, R.B. (2007). Volcanic Eruptions and Solar Activity.

205. Schwenn, R. (2006). Space Weather: The Solar Perspective. https://doi.org/10.12942/lrsp-2006-2

206. Marusek, J.A. (2005). Supernovae – The Force Behind Great Ice Ages.

207. Kundt, W. (2015). Cosmic rays, clouds and climate. https://doi.org/10.1051/epn/2015306

208. Svensmark, H. (2015). Cosmic rays, clouds and climate. https://doi.org/10.1051/epn/2015204

209. Owens, M.J., et al. (2024). A Geomagnetic Estimate of Heliospheric Modulation Potential Over the Last 175 Years. https://doi.org/10.21203/rs.3.rs-4165343/v1

210. Marsh, N., & Svensmark, H. (2003). Solar Influence on Earth's Climate. https://doi.org/10.1023/a:1025573117134

211. Usoskin, I.G., et al. (2010). Ionization effect of solar particle GLE events in low and middle atmosphere. https://doi.org/10.5194/acpd-10-30381-2010

212. Karoff, C., & Svensmark, H. (2018). How did the Sun affect the climate when life evolved on the Earth? A case study on the young solar twin Kappa-1 Ceti.

213. Usoskin, I.G., & Kovaltsov, G.A. (2006). Link Between Cosmic Rays and Clouds on Different Time Scales. https://doi.org/10.1142/9789812707185_0026

214. Riley, P., et al. (2015). Inferring the Structure of the Solar Corona and Inner Heliosphere During the Maunder Minimum Using Global Thermodynam…. https://doi.org/10.1088/0004-637x/802/2/105

215. Conlon, K., et al. (2014). Supernova Disaster Preparedness Plan.

216. Usoskin, I.G., & Kovaltsov, G.A. (2008). Production of cosmogenic 7Be isotope in the atmosphere: Full 3-D modeling. https://doi.org/10.1029/2007jd009725

217. Gil, A. (2017). Heliospheric modulation of galactic cosmic rays: Effective energy of ground-based detectors.

218. Cook, J. (2019). The rise of the Mass cycle. https://doi.org/10.4324/9781351042383-2

219. Svensmark, H., et al. (2017). Increased ionization supports growth of aerosols into cloud condensation nuclei. https://doi.org/10.1038/s41467-017-02082-2

220. Bork, N., et al. (2012). Structures and reaction rates of the gaseous oxidation of SO 2 by an O 3 – (H 2 O) 0-5 cluster – a density functional…. https://doi.org/10.5194/acp-12-3639-2012

221. Svensmark, H., et al. (2006). Experimental evidence for the role of ions in particle nucleation under atmospheric conditions. https://doi.org/10.1098/rspa.2006.1773

222. Enghoff, M.B., et al. (2008). Evidence for the Role of Ions in Aerosol Nucleation. https://doi.org/10.1021/jp806852d

223. Enghoff, M.B., & Svensmark, H. (2008). The role of atmospheric ions in aerosol nucleation – a review. https://doi.org/10.5194/acp-8-4911-2008

224. Svensmark, H., Bondo, T., & Svensmark, J. (2009). Cosmic ray decreases affect atmospheric aerosols and clouds. https://doi.org/10.1029/2009gl038429

225. Svensmark, H., et al. (2021). Atmospheric ionization and cloud radiative forcing. https://doi.org/10.1038/s41598-021-99033-1

226. Svensmark, H. (2012). Evidence of nearby supernovae affecting life on Earth. https://doi.org/10.1111/j.1365-2966.2012.20953.x

227. Mironova, I., & Usoskin, I. (2013). Possible effect of extreme solar energetic particle events of September-October 1989 on polar stratospheric aerosols:…. https://doi.org/10.5194/acp-13-8543-2013

228. Svensmark, H. (2007). Cosmoclimatology: a new theory emerges. https://doi.org/10.1111/j.1468-4004.2007.48118.x

229. Svensmark, H., Enghoff, M.B., & Pedersen, J.O.P. (2013). Response of cloud condensation nuclei (>50 nm) to changes in ion-nucleation. https://doi.org/10.1016/j.physleta.2013.07.004

230. Zharkova, V. (2020). Modern Grand Solar Minimum Will Lead to Terrestrial Cooling. https://doi.org/10.1080/23328940.2020.1796243

231. Scherer, K., et al. (2007). Interstellar-Terrestrial Relations: Variable Cosmic Environments, The Dynamic Heliosphere, and Their Imprints on Terr…. https://doi.org/10.1007/s11214-006-9126-6

232. Svensmark, H. (2023). A persistent influence of supernovae on biodiversity over the Phanerozoic. https://doi.org/10.1002/ece3.9898

233. Shaviv, N.J. (2002). Cosmic Ray Diffusion from the Galactic Spiral Arms, Iron Meteorites, and a Possible Climatic Connection. https://doi.org/10.1103/physrevlett.89.051102

234. Heikkilä, U., Beer, J., & Feichter, J. (2007). Modeling cosmogenic radionuclides 10 Be and 7 Be during the Maunder Minimum using the ECHAM5-HAM General Circulation …. https://doi.org/10.5194/acpd-7-15341-2007

235. Yndestad, H. (2022). Jovian Planets and Lunar Nodal Cycles in the Earth's Climate Variability. https://doi.org/10.3389/fspas.2022.839794

236. Moss, D., et al. (2008). Solar Grand Minima and Random Fluctuations in Dynamo Parameters. https://doi.org/10.1007/s11207-008-9202-z

237. Kye, S.B. (2022). Uses of the Little Ice Age Theory in the Korean Academia of Korean History. https://doi.org/10.29186/kjhh.2022.46.11

238. Leif (2018). The modulation potential series is not very useful as a proxy for solar activity since the modulation potential is a ….

239. Zharkova, V.V., & Vasilieva, I. (2025). Links of Terrestrial Environment with Solar Activity and Solar and Planetary Orbital Motion. https://doi.org/10.4236/acs.2025.151004

240. Thouret, J.C., et al. (2002). Reconstruction of the AD 1600 Huaynaputina eruption based on the correlation of geologic evidence with early Spanish …. https://doi.org/10.1016/s0377-0273(01)00323-7

241. Prival, J.M., et al. (2020). New insights into eruption source parameters of the 1600 CE Huaynaputina Plinian eruption, Peru. https://doi.org/10.1007/s00445-019-1340-7

242. Báez, W., et al. (2015). Estratigrafía y evolución del Complejo Volcánico Cerro Blanco, Puna Austral, Argentina.

243. Tilling, R.I. (2009). Volcanism and associated hazards: the Andean perspective. https://doi.org/10.5194/adgeo-22-125-2009

244. Silva, S.L.D., & Zielinski, G.A. (1998). Global influence of the AD 1600 eruption of Huaynaputina, Peru. https://doi.org/10.1038/30948

245. Fei, J., Zhang, D.D., & Lee, H.F. (2016). 1600 AD Huaynaputina Eruption (Peru), Abrupt Cooling, and Epidemics in China and Korea.

246. Fei, J., & Zhou, J. (2008). The possible climatic impact in North China of the AD 1600 Huaynaputina eruption, Peru. https://doi.org/10.1002/joc.1776

247. Schwarzer, C., et al. (2010). 400 Years for Long-Distance Dispersal and Divergence in the Northern Atacama Desert – Insights from the Huaynaputina …. https://doi.org/10.1016/j.jaridenv.2010.05.034

248. Vera, Y.A. (2011). Monitoreo sísmico temporal y caracterización geoquímica de fumarolas y fuentes termales del volcán Huaynaputina.

249. Brázdil, R., et al. (2016). Climatic effects and impacts of the 1815 eruption of Mount Tambora in the Czech Lands. https://doi.org/10.5194/cp-12-1361-2016

250. Boers, B.D.J. (1995). Mount Tambora in 1815: A Volcanic Eruption in Indonesia and Its Aftermath. https://doi.org/10.2307/3351140

251. Cole-Dai, J., et al. (2009). Cold Decade (AD 1810–1819) Caused by Tambora (1815) and Another (1809) Stratospheric Volcanic Eruption. https://doi.org/10.1029/2009gl040882

252. Bodenmann, T., et al. (2011). Perceiving, explaining, and observing climatic changes: An historical case study of the "year without a summer" 1816. https://doi.org/10.1127/0941-2948/2011/0288

253. Oppenheimer, C. (2003). Climatic, environmental and human consequences of the largest known historic eruption: Tambora volcano (Indonesia) 1815. https://doi.org/10.1191/0309133303pp379ra

254. Auchmann, R., et al. (2012). Extreme climate, not extreme weather: the summer of 1816 in Geneva, Switzerland. https://doi.org/10.5194/cp-8-325-2012

255. Bearce, S., & Bolli, E. (2021). 1816: The Year Without a Summer. https://doi.org/10.4324/9781003239260-5

256. Newhall, C., Self, S., & Robock, A. (2018). Anticipating future Volcanic Explosivity Index (VEI) 7 eruptions and their chilling impacts. https://doi.org/10.1130/ges01513.1

257. Chipperfield, M.P., et al. (2025). Ongoing large ozone depletion in the polar lower stratospheres: the role of increased water vapour. https://doi.org/10.1039/d4fd00163j

258. Lightfoot, H.D., & Ratzer, G. (2025). The Impact of the Hunga Tonga Volcanic Eruption on Earth's Temperature. https://doi.org/10.29169/1927-5129.2025.21.14

259. Zhou, X., et al. (2026). Residence time of Hunga stratospheric water vapour perturbation quantified at 9 years. https://doi.org/10.5194/egusphere-egu26-22524

260. Zuo, M., et al. (2022). Volcanoes and Climate: Sizing up the Impact of the Recent Hunga Tonga-Hunga Ha'apai Volcanic Eruption from a Historic…. https://doi.org/10.1007/s00376-022-2034-1

261. Marshall, L.R., et al. (2022). Volcanic effects on climate: recent advances and future avenues. https://doi.org/10.1007/s00445-022-01559-3

262. Imran, S. (2017). Radiation Transfer Calculations and Assessment of Global Warming by CO2.

263. Byrom, R.E., & Shine, K.P. (2022). Methane's Solar Radiative Forcing. https://doi.org/10.1029/2022gl098270

264. Shindell, D.T., et al. (2001). Solar Forcing of Regional Climate Change During the Maunder Minimum. https://doi.org/10.1126/science.1064363

265. Shaviv, N.J. (2005). On climate response to changes in the cosmic ray flux and radiative budget. https://doi.org/10.1029/2004ja010866

266. Goslar, T. (2003). 14C as an Indicator of Solar Variability. https://doi.org/10.22498/pages.11.2-3.12

267. Harris, S.A. (2023). Comparison of Recently Proposed Causes of Climate Change. https://doi.org/10.3390/atmos14081244

268. Feynman, J. (2007). Has solar variability caused climate change that affected human culture?. https://doi.org/10.1016/j.asr.2007.01.077

269. Stothers, R.B. (2000). Climatic and Demographic Consequences of the Massive Volcanic Eruption of 1258. https://doi.org/10.1023/a:1005523330643

270. Ewert, J., Diefenbach, A., & Ramsey, D. (2018). 2018 Update to the U.S. Geological Survey National Volcanic Threat Assessment. https://doi.org/10.3133/sir20185140

271. MILES, G.M., GRAINGER, R.G., & HIGHWOOD, E.J. (2014). Volcanic Aerosols. https://doi.org/10.4135/9781446247501.n4085

272. Serra, I., et al. (2020). Probability estimation of a Carrington-like geomagnetic storm. https://doi.org/10.5194/egusphere-egu2020-8763

273. Chapman, S.C., Horne, R.B., & Watkins, N.W. (2020). Using the aa Index Over the Last 14 Solar Cycles to Characterize Extreme Geomagnetic Activity. https://doi.org/10.1029/2019gl086524

274. Schurer, A.P., Tett, S.F.B., & Hegerl, G.C. (2013). Small influence of solar variability on climate over the past millennium. https://doi.org/10.1038/ngeo2040

275. Lean, J., Beer, J., & Bradley, R. (1995). Reconstruction of solar irradiance since 1610: Implications for climate change. https://doi.org/10.1029/95gl03093

276. Landscheidt, T. (2003). New Little ICE Age Instead of Global Warming?. https://doi.org/10.1260/095830503765184646

277. Marsh, N., & Svensmark, H. (2003). Galactic cosmic ray and El Niño–Southern Oscillation trends in International Satellite Cloud Climatology Project D2 l…. https://doi.org/10.1029/2001jd001264

278. Berry (2022). The Impact of Human CO2 on Atmospheric CO2. https://doi.org/10.53234/scc202112/13

279. Licht, S., Wang, B., & Wu, H. (2011). STEP—A Solar Chemical Process to End Anthropogenic Global Warming. II: Experimental Results. https://doi.org/10.1021/jp111781a

280. Marusek, J.A. (2010). El sol y el cambio climatico.

281. Lange, W.D. (2025). Why I am a Climate Realist.

282. Berry, E.X. (2019). Human CO_2 Emissions Have Little Effect on Atmospheric CO_2. https://doi.org/10.11648/j.ijaos.20190301.13

283. Harde, H. (2023). How Natural CO2 Dominates the Increase in Atmospheric CO2. https://doi.org/10.53234/scc202301/21

284. Marusek, C. (2008). Heat Island Effects.

285. Nakamura, J., & Ishida, M. (2025). Global Warming and CO2 Emissions. https://doi.org/10.1007/978-981-95-3465-4_1

286. Scafetta, N. (2010). Empirical evidence for a celestial origin of the climate oscillations and its implications. https://doi.org/10.1016/j.jastp.2010.04.015

287. Xu, G., et al. (2019). Century-scale temperature variability and onset of industrial-era warming in the Eastern Tibetan Plateau. https://doi.org/10.1007/s00382-019-04807-z

288. Robock, A. (1979). The "Little Ice Age": Northern Hemisphere Average Observations and Model Calculations. https://doi.org/10.1126/science.206.4425.1402

289. Tina (2016). A Primer on Carbon Dioxide and Climate.

290. Marusek, C. (2008). Response to CCSP-Usp-Synthesis Report.

291. hy (2017). Barents Sea. https://doi.org/10.1007/978-3-319-25582-8_20006

292. Yndestad, H. (2006). The Arctic Ocean as a Coupled Oscillating System to the Forced 18.6 Year Lunar Gravity Cycle. https://doi.org/10.1007/978-0-387-34918-3_16

293. Yndestad, H. (2006). The influence of the lunar nodal cycle on Arctic climate. https://doi.org/10.1016/j.icesjms.2005.07.015

294. Yndestad, H. (2004). A General System Theory.

295. Cohler, J., et al. (2026). IPCC's Earth Energy Imbalance Assessment is Based on Physically Invalid Argo-Float-Based Estimates of Global Ocean He…. https://doi.org/10.5281/zenodo.18936064

296. Yndestad, H. (2009). The influence of long tides on ecosystem dynamics in the Barents Sea. https://doi.org/10.1016/j.dsr2.2008.11.022

297. Annable, J. (1984). Analysis. https://doi.org/10.1080/05775132.1984.11470925

298. Cruikshank, J. (2001). Glaciers and Climate Change: Perspectives from Oral Tradition. https://doi.org/10.14430/arctic795

299. Lloyd's (2013). Solar Storm Risk to the North American Electric Grid.

300. Tsurutani, B.T., et al. (2012). Extreme changes in the dayside ionosphere during a Carrington-type magnetic storm. https://doi.org/10.1051/swsc/2012004

301. Love, J.J., et al. (2024). On the uncertain intensity estimate of the 1859 Carrington storm. https://doi.org/10.1051/swsc/2024015

302. Sarkesian, S.C., Williams, J.A., & Cimbala, S.J. (2002). U.S. National Security. https://doi.org/10.1515/9781685859145

303. Cliver, E.W., et al. (2022). Extreme solar events. https://doi.org/10.1007/s41116-022-00033-8

304. Marusek, J.A. (2007). Impact Disaster Preparedness Plan.

305. Ahmed, M., et al. (2023). Transformer Protection Strategy During Solar Storm: Threat Analysis and Implementing Countermeasures. https://doi.org/10.1109/icps60393.2023.10428848

306. Conlon, K., et al. (2014). Solar Storm Disaster Preparedness Plan.

307. Marusek, J.A. (2006). Comet and Asteroid Threat Impact Analysis.

308. Baum, S.D., et al. (2015). Resilience to global food supply catastrophes. https://doi.org/10.1007/s10669-015-9549-2

Appendices

A. Downloads

You are reading an offline copy (version 293, 2026-07-08 15:39 UTC). The latest edition is always available — readable online, or as a fresh EPUB/PDF download — at https://winter-is-coming.pages.dev/downloads.html.

Kindle users: download the EPUB there and send it to your device with Amazon's *Send to Kindle* (modern Kindles open EPUB directly; the old `.mobi` format is retired).

B. About

B.1 The author

Frank Dosk

B.2 Corrections

This is a living document that is revised between releases. If you spot an error, it may already be fixed in the current version at https://winter-is-coming.pages.dev — the Changelog appendix lists what changed recently.

B.3 License

B.4 Cite this book

Frank Dosk (2026). *Winter Is Coming*. Version 293 (2026-07-08 15:39 UTC). https://winter-is-coming.pages.dev

C. Changelog

What changed in each release, newest first. Each release is a rebuild of the whole book from the source manuscript.

C.1 Version 293 — 2026-07-08 15:39 UTC

- Current release.